UC Merced

UC Merced Electronic Theses and Dissertations

Title

Role of Charged Facets and Surface States in Colloidal Quantum Dot Spectroscopy

Permalink

https://escholarship.org/uc/item/07s5x41s

ISBN

9798173794710

Author

Bajpai, Adityaa

Publication Date

2026-08-07

Copyright Information

This work is made available under the terms of a Creative Commons Attribution License, available at https://creativecommons.org/licenses/by/4.0/

Peer reviewed|Thesis/dissertation

eScholarship.org Powered by the California Digital Library
University of California

UNIVERSITY OF CALIFORNIA MERCED



DOCTORAL DISSERTATION

Role of Charged Facets and Surface States in Colloidal Quantum Dot Spectroscopy

---

A dissertation submitted in fulfillment of the requirements for the degree of Doctor of Philosophy

in

Physics

by

Adityaa Bajpai

Committee Members:

Prof. David A. Strubbe (Chair)
Prof. David F. Kelley (Advisor)
Prof. Jay Sharping

2026

Copyright Page

Portions of Chapter 2 © 2025 AIP Publishing
Portions of Chapter 3 © 2025 AIP Publishing
Portions of Chapter 4 © 2026 AIP Publishing
All other chapters © 2026 Adityaa Bajpai
All rights reserved

The dissertation of Adityaa Bajpai is approved, and it is acceptable in quality and form for publication on microfilm and electronically:

_____

Professor David F. Kelley

_____

Professor Jay Sharping

_____

Professor David Strubbe (Committee Chair)

Contents

List of figures **vii**

List of Tables **xi**

Acknowledgements **xv**

Curriculum Vitae **xv**

Abstract **xix**

1 Introduction to Colloidal Quantum Dots **1**
1.1 Electronic Structure & Photophysics . . . 2
1.2 Colloidal Synthesis . . . 3
1.3 Excitonic Fine Structure . . . 5
1.4 Spectroscopy of Quantum Dots . . . 9
1.5 Photoluminescent Excitation (PLE) Spectroscopy . . . 10

2 Ligand Effects on Fine Structure of CdTe Nanocrystals **13**
2.1 Abstract . . . 13
2.2 Introduction . . . 13
2.3 Modeling/Fitting the PL & PLE Data . . . 15
2.4 Determination of the Homogeneous Linewidth . . . 17
2.5 Radiative Lifetime Calculations . . . 18
2.6 Determination of the Extinction Coefficient . . . 19
2.7 Effects of Charged Ligands on Fine Structure . . . 20
2.7.1 Ligand-dependent Spectroscopy . . . 21
2.7.2 Ligand-dependent Radiative Dynamics . . . 26
2.7.3 Modeling the Ligand-dependent Spectroscopy . . . 28
2.7.4 Lowering of Symmetry & Group Theory Considerations . . . 32
2.7.5 Reversal to Charged Ligation . . . 33
2.8 Conclusions . . . 34

3 Surface Stoichiometry and Continuum **35**
3.1 Abstract . . . 35
3.2 Introduction . . . 35
3.3 Surface Stoichiometry-dependent Spectroscopy . . . 37
3.4 Comparison with CdSe and ZnSe QDs . . . 42
3.5 Ligand to QD Continuum Transitions . . . 44

3.6 Conclusion 46

4 Photophysics of Silver Indium Gallium Sulfide (AIGS) 47
4.1 Abstract 47
4.2 Introduction 47
4.3 Spectroscopy of AIGS Dots 50
4.4 Structural Characterization 52
4.4.1 EDX Results and RCP Calculation 52
4.4.2 Structural Inhomogeneity and Wavefunction Calculations 56
4.5 Inhomogeneity in Oscillator Strengths 60
4.6 Delayed Emission Model 61
4.6.1 Analysis of AIGS Radiative Dynamics & Comparison with Literature 62
4.7 Calculation of average dipole moment of the excited state 64
4.8 Conclusions 65

5 Summary & Outlook 66
5.0.1 Ligand Effects on the Fine Structure of CdTe QDs 66
5.0.2 Surface Stoichiometry and the Continuum 66
5.0.3 Photophysics of AIGS Quantum Dots 67
5.1 Outlook & Future Directions 67
5.1.1 Quantifying Ligand Fields 68
5.1.2 A More Quantitative Study of the Continuum 69
5.1.3 Engineering Disorder in Ternary Quantum Dots 69

A Synthesis & Ligand Exchange of CdTe Dots 70

B CdTe Synthesis & Surface Treatment 72

C Herzberg Teller Coupling 77

References 80

List of Figures

1.1 (a) The electronic band structure of bulk CdTe crystals adapted from [21], (b) the potential wells that confine the electrons and holes and the respective envelope wavefunction energies, and (c) the absorption (black) and emission (red) spectra of CdTe dots synthesized in our lab, showing the different quantum confined transitions between respective electron-hole envelope functions, the Stokes shift (52 meV), and the emission linewidth (117 meV). 3

1.2 (a) A schematic of the colloidal synthesis method showing tellurium precursor being injected into the three-neck flask containing the cadmium precursor and connected to a Schlenk line keeping the reaction under a constant flow of Nitrogen (b) shows a TEM scan of a sample of CdSe dots (roughly 3 nm in diameter) synthesized by Fernanda Pilla Bardela. 4

1.3 The electronic fine structure of the $1S_e - 1S_h$ transition showing the e-h exchange splitting and effects of anisotropies in the nanocrystals 7

1.4 (a) A level diagram of $1S_e - 1S_h$ transitions. The homogenous dispersion of the 0^U and $\pm 1^U$ levels are represented by the blue and red Gaussian, respectively. The schematic highlights three excitation events at energies E_1, E_2, and E_3. (b) Shows the polarization anisotropy (r) data corresponding to CdTe dots with the three energies marked with vertical lines. 11

2.1 (a) Shows the experimental static PLE/absorption spectra data (blue circle) of a CdTe sample plotted with respect to energy relative to the PL peak energy and a calculated fit (solid black line). The gaussians corresponding to the $\pm 1^U$ and 0^U states, $1S_e - 2S_h$ transition, and cubic background are represented by the blue, pink, green, and black dashed lines, respectively. (b) The experimental (blue markers) and calculated (red solid line) polarization anisotropy data for the same sample are shown. . 16

2.2 PL/PLE spectra of the ODPA ligated CdTe particles with the PLE spectra and (b) 1S-1S peak energy and a function of detection energy (black squares) and a linear fit (red line) showing a slope of 0.527. 17

2.3 Absorption and PL spectra of 3.3 nm diameter CdTe particles having ODPA ligands (black) or octanethiol ligands (red). The PL spectra have widths of 110 meV (ODPA) and 118 meV(octanethiol), and Stokes shifts of 64 meV (ODPA) and 51 meV (octanethiol). The inset shows ODPA and octanethiol absorption spectra with the octanethiol spectrum shifted 6.5 nm to the blue, so that its absorption maximum matches that of the ODPA spectrum 22
2.4 (a) FT-IR spectra of washed ODPA ligated CdTe QDs (black) and same QDs with octanethiol ligands (red). Panel (b) shows the low frequency features of the spectra, most notably the LO phonon mode at 145 cm^{-1} which is used to normalize the two curves since the intensity of the LO phonon line is proportional to the total volume of the CdTe nanocrystals. The QD surface bound ODPA can be characterized by the symmetric and asymmetric P-O-Cd stretch modes ($\nu_{\text{P-O-Cd}}$) at 1093 cm^{-1} and 1172 cm^{-1}.[47, 48] Those features are almost completely absent in the ligand exchanged sample (Oct-SH ligated QDs) confirming the near complete removal of ODPA upon ligand exchange. Panel (c) shows the high frequency components showing the stretch modes corresponding to the CH_2 at 2848 cm^{-1} and 2918 cm^{-1} and CH_3 at 2956 cm^{-1} present in both ODPA and octanethiol ligated QDs. Both high frequency and low frequency components have features corresponding to methanol (broad feature at $\sim$3250 cm^{-1} and a sharp feature at 1024 cm^{-1}) which was used in the process of purifying the QDs 23
2.5 PLE anisotropy spectra of CdTe QDs ligated with ODPA (black curve), octane thiol (red curve). The energy zero corresponds to excitation and detection at the same wavelength, which is the PL maximum. Also shown are linear fits near r = 0 with slopes of 0.277 eV-1 and 0.222 eV-1 for ODPA and octanethiol, respectively. 24
2.6 Shows the PLE anisotropy spectra CdTe QDs ligated with octanethiol in 1:1 (v/v) toluene/ODE (red curve) and 1:3 (v/v) toluene/ODE (blue curve) showing near identical features. The PLE anisotropy spectrum of the ODPA ligated particles in 1:1 (v/v) toluene/ODE is also shown for reference (black curve). 26
2.7 PL decays shown on linear (A) and log (B) scales. Also shown are fits corresponding to radiative lifetimes of 23.0, 27.3 and 23.9 ns for ODPA, octanethiol and ODPA (reversed) ligands, respectively. 27
2.8 (a) The absorption spectra and (b) PLE anisotropy spectra of CdTe QDs ligated with ODPA in the original reaction mixture (black curves), same particles ligand exchanged to octanethiol (red curves) and after reversal to ODPA ligation (blue curves) discussed in the main text. It also shows the absorption and PLE anisotropy spectra corresponding to an essentially identical set of particles (a different batch of the same ODPA/OA synthesis used for the data in the main text) ligand exchanged to oleic acid ligation (violet curves). 33

2.9 PL decays shown on linear (a) and log (b) scales. Also shown are fits corresponding to radiative lifetimes of 23.7, 26.3 and 23.9 ns for ODPA, octanethiol and oleic acid ligands, respectively. 33

3.1 The absorption and luminescence spectra of CdTe QD with a schematic level diagram showing the initial and final states of the quantum confined transitions along with the transitions that contribute to the continuum. 36
3.2 (a) Absorption spectra of purified particles (black), the purified particles treated with TOPTe resulting in the 'Te-capped' surfaces (red), followed by a treatment with $Cd(St)_2$ resulting in reversal to 'Cd-capped' nature (blue). The inset shows the closer look at the $1S_e$–$1S_h$ peaks of the absorption spectra, showing the red shift upon each successive surface treatment. (b) The same data as (a), plotted as a function of energy from the respective $1S_e$–$1S_h$ peaks, for comparison of the continuum contributions. The plot also includes the difference spectrum. 38
3.3 FTIR spectra of the purified particles (black), Te-capped particles (red) and Te-capped particles treated with TOP (blue). These spectra a normalized with respect to the CdTe LO phonon peak seen at ~ 145 cm^{-1} since its intensity scales with the volume and number of QDs. The relevant peaks in the spectra are labeled and the assignment is shown in Table 3.1. 41
3.4 A schematic showing the varying level of conduction band tunneling and Fermi energy (dashed line) in Te-CdTe, Se-CdSe and Se-ZnSe QDs. The larger wavefunction overlaps and the higher Fermi energy in the Se-ZnSe QDs results in the higher continuum intensity and lower onset energy relative to the $1S_e$-$1S_h$ energy ('continuum tail') 43
3.5 (a) Absorption spectra of CdTe QDs ligated with ODPA (black), octanethiol (red) and oleic acid (blue). (b) The same ODPA and octanethiol spectra as in (a), except plotted as a function of energy from the lowest exciton peak and including the scaled difference spectrum. 45

4.1 Absorption and PL spectra for AIGS QDs in chloroform and toluene. The vertical lines at 515, 525 and 535 nm indicate the detection wavelengths for the PL decays and PLE anisotropy spectra. 49
4.2 Photoluminescence excitation anisotropy spectra of the AIGS QDs at the indicated detection wavelengths. Also shown (for comparison) is the PLE anisotropy of InP/ZnSe/ZnS QDs [23] having a comparable PL maximum wavelength. 51
4.3 (a) PL decays of AIGS QDs in chloroform, taken with detection on the blue edge (515 nm), center (525 nm), and on the red edge (535 nm) of the band edge PL spectrum. The decays are fit to biexponentials and the fitting parameters are given in Table 4.1 (b) The fit and residuals for the 525 nm fit. 52

4.4 (a) The high-angle annular dark field TEM image of a representative sample. (b) The same image with the composite of the different elemental components: Ag (red), Ga (dark blue), S (light blue) and In (green), obtained through EDX measurements. (c-f) The elemental maps of the individual elements as shown at the lower left corner of each panel. . . . 53
4.6 (a) The radial profiles of atomic contributions obtained from averaging linescans from 10 particles (solid lines) and the fitted radial profiles (dashed lines). (b) The radial composition profile of the metals calculated from the differential equations describing the particle growth process and the relative atomic amounts. 54
4.5 Figures a – c show representative elemental composites obtained through EDX measurements. The red line marks the region scanned to produce the elemental cross section plots shown in Figures d-f. Figures d – f show the occurrence of Ga (dark blue line), S (light blue line), Ag (red line) and In (green area) across the respective cross sections. The noisy signal makes it difficult to directly estimate the radial composition profiles from EDX scan cross-sections. 55
4.7 Calculated electron-hole overlap and electric field strength averaged over the hole density, plotted versus the relative energy of the lowest exciton, for 20 structures. 57
4.8 Hole (left) and electron (right) wavefunctions for two gradient alloy structures. Plots show a cross-section through the center of each structure. The amplitude of the wavefunction on each atom is shown, color-coded with increasing amplitude: white < gray < tan < yellow < pink < red. Graphics were prepared using VMD.13 Note that some of the tetrahedral holes are empty, resulting in gaps that can be seen in the Figure. 59
4.9 Emission spectra of AIGS QDs in toluene (black) and chloroform (red). The wavelength shift is about 0.6 nm. 64

B.1 (A-C) Shows example absorption spectra of the purified (black) and Te-CdTe (red) QD samples of 3.3-3.4 nm in diameter. The Te-capped particles are obtained via treatments similar to ones described above. 75
B.2 The lowest energy region of the Cd-rich and Te-rich QD absorption spectra are fitted to a sum of three Gaussians. The absorption spectra are indicated in black, the contributing Gaussians in red and the fitted sum peaks in blue. The highest energy fitting peaks contain contributions from both quantum confined transitions and the low energy continuum. The widths (fwhm) of the lowest energy Cd-rich and Te-rich peaks are 131and 136 meV, as indicated. Making the surface Te rich slightly decreases the 2S-1S splitting by 5 meV, from 230 to 225 meV. The statistical error in this fitting ± 2 meV, so this difference is very small, but statistically significant 76

B.3 (a) Absorption spectra of CdTe QDs ligated with ODPA (black), octanethiol (red) and oleic acid (cadmium oleate treated) (blue). (b) The same ODPA and octanethiol spectra as in (a), except plotted as a function of energy from the lowest exciton peak. 76

C.1 The electronic fine structure of the $1S_e - 1S_h$ transition showing the e-h exchange splitting and effects of anisotropies in the nanocrystals 77
C.2 Shows the depolarization ratio (ρ) as a function of (a) Δ/η (b) η and (c) Δ 79

List of Tables

2.1 Fitting parameters for the PL decays. 27

3.1 Infrared peak wavenumbers and assignments. 41
3.2 We calculate the bond energies from standard enthalpy of formation (ΔH_f) for the reaction MX(s) $\rightarrow$ M(g) + $\frac{1}{2}$ X_2 and then to calculate the bond dissociation energy (BDE) as: BDE(MX) $= \Delta H_f + \frac{1}{2}$ BDE(X_2) . . . 44

4.1 Biexponential fitting parameters to $I(t) = A_f \exp(-t/\tau_f) + A_s \exp(-t/\tau_s)$, where τ_f and τ_s are the fast and slow decay times and A_f and A_s are the fast and slow amplitudes, respectively. The decays are normalized such that $A_f + A_s = 1$. 51
4.2 Experimental and calculated atomic fractions. 54
4.3 Parameters of the shallow trap model calculated using the fit values in Table 4.1. Here τ_1 (τ_{-1}) is the trapping (de-trapping) time constants, τ_{rad} is the radiative time constant (inverse of the respective rates, k_1, k_{-1} & k_{rad}), and ΔE is the energy separation of the trap states from the band edge. . 62
4.4 Biexponential decay parameters for as-grown and TBP-treated quantum dots reported by Uematsu (2018[111], 2023[112]). 63
4.5 Radiative and trapping parameters derived from the delayed emission model for as-grown and TBP-treated quantum dots. 63

Acknowledgements

I express my sincere gratitude to my advisor, Professor David Kelley, for his unwavering support, guidance, and patience throughout my time in his lab. His insightful ideas and ability to make sense of complex experimental data with a simple physical picture were equally instructive and amusing to witness. His mentorship has equipped me with the tools to think critically and rigorously, lessons that extend far beyond the lab and into life itself.

I would also like to thank Professor Anne Myers Kelley for being generous with her knowledge and time in group meetings and sharing her notes which were very insightful for me as a new student in Dave's group. I also want to thank Professor Myers Kelley for her work on the Monte Carlo structure and EMA wavefunction calculations for AIGS that were incredibly important for the interpretation of spectroscopic data in Chapter 4. I would also like to thank our collaborators at Nanosys-Shoei Chemicals-Ilan Jen-La Plante, Christopher Sunderland, Xudong Wang, David Olmeijer, Chunming Wang- who provided us with pristine AIGS samples and the EDX ICP data that made the paper possible.

I am also deeply grateful to colleagues I found at UC Merced: Dr. Mark Woodall, Dr. Paul Cavanaugh, Dr. Arun Ashokan, Fernanda Pilla Bardella and many others who offered their help and encouragement at various points along the way.

I am also thankful to the National Science Foundation for funding the work under NSF award no. CHE-2203301.

I would like to thank Prof. Manoj Harbola, Prof. R. Vijaya, Dr. Kurup, and Dr. Gurunath, among numerous mentors who nurtured my curiosity and guided me early on. Finally, I dedicate this work to my parents, who believed in me throughout this long and challenging journey. Your support has meant everything.

ADITYAA BAJPAI

abajpai4@ucmerced.edu | Website | +1-209-506-0375

EDUCATION

PhD, Physics (2021–2026)
Prof. David Kelley's Lab
University of California (UC) Merced

BS-MS (Dual degree), Physics (2015–2020)
Prof. R. Vijaya's Lab
Indian Institute of Technology (IIT), Kanpur

PUBLICATIONS

1. **A. Bajpai**, D. F. Kelley. "Effect of Surface Stoichiometry on the Continuum Intensity in CdTe Quantum Dots" (*submitted to Journal of Physical Chemistry C*)
2. **A. Bajpai**, I. Jen-La Plante, C. Sunderland, D. Olmeijer, A. M. Kelley, D. F. Kelley. "Radiative Dynamics of $AgIn_xGa_{1-x}S_2$ Quantum Dots" *J. Chem. Phys. 164, 154701* (2026)
3. **A. Bajpai**, D. F. Kelley."Ligand Effects on the Angular Momentum Fine Structure of CdTe Quantum Dots" *J. Chem. Phys. 163, 154308* (2025)
4. M. Woodall, **A. Bajpai**, Z. von Jena, A. Argueta, A. S. Bracker, M. Scheibner. " Detection and Localization of Charges in Semiconductors with Quantum Dot Molecules" (in preparation)

RESEARCH TALKS

- **A. Bajpai**, D. F. Kelley. "Radiative Dynamics in II-VI Quantum Dots" *National ECS Meeting* (2026) (Invited)
- **A. Bajpai**, M. Woodall, A. S. Bracker, M. Scheibner. "Hot Carrier Ground States in Coupled Quantum Dots" *APS March Meeting* (2023)
- **A. Bajpai**, G. Kumar, R Vijaya. "Tamm Plasmon Modes for Designing Optically-pumped Vertical Cavity Laser" *International OSA Network of Students (IONS)* (2020)
- M. Woodall, **A. Bajpai**, Z. von Jena, A. S. Bracker, S. G. Carter, M. Scheibner. "*In Situ Charge Detection with Single Quantum Dot Molecules*" APS March Meeting (2023)
- M. Woodall, **A. Bajpai**, P. Kumar, C. Jennings, A. S. Bracker, S. G. Carter, M. Scheibner. "*Sensing Capabilities of Self- Assembled Quantum Dot Molecules*" 2nd International Nanoscale Analytics Workshop 2022

RESEARCH SKILLS

Experimental Skills: IR/UV-Vis spectroscopy (cryo. & room temp.), Time Correlated Single Photon Counting (TCSPC), magneto-optical characterization of excitonic states in quantum materials, contact/non-contact Atomic Force Microscopy (AFM), confocal microscopy, maintenance and operation of picosecond/femtosecond Ti:Sapphire laser systems. Experienced with high temperature synthesis and optical characterization of semiconductor nanocrystals and dielectric/metal layered structures.

Programming Languages/Software: Python, C, Matlab, Mathematica, Origin, LaTeX, Inkscape

Research Experience

Photophysics & Radiative Dynamics of Colloidal Quantum Dots
Mentored by Prof. David F. Kelley, Dept. of Chem. & Biochem., UC Merced Aug 2023 - Aug 2026

Ligand-fields & Angular Momentum Fine Structure:

- Synthesized CdTe quantum dots (PLQY $\sim$ 70-80%) with strongly charged ligands (octadecylphosphonic acid) and weakly charged ligands (octanethiol).
- Performed static/polarized PLE and radiative lifetime measurements on these samples to demonstrate a measurable ligand dependent change in the spectroscopy of these dots.
- Analyzed the spectroscopic data using a commonly used two-parameter model and demonstrated that it doesn't describe the data quantitatively.

Metal Inhomogeneity and the Spectroscopy of $AgIn_xGa_{1-x}S_2$ Quantum Dots:

- Performed static and polarized photoluminescence excitation (PLE) measurements showed signs of strongly polarized transitions in the absorbing states, which is consistent with inhomogeneous composition.
- Analyzed the viability of three possible models to explain the biphasic PL decay – inhomogeneity in electron-hole overlap, delayed emissions due to shallow defect states, and inhomogeneity in the oscillator strength of the lowest exciton fine-structure level.

Surface Chemistry and the Continuum Transitions:

- Demonstrated an increase in the continuum absorption intensity of CdTe quantum dots by changing the surface stoichiometry from metal-rich to chalcogenide-rich. These experiments will confirm that some of the broad, featureless absorption seen in most semiconductor quantum dots results from these surface-to-bulk type transitions.

Interaction of Quantum States in Coupled Quantum Dots (CQDs)
Mentored by Prof. Michael Scheibner, Dept. of Phys., UC Merced Jan 2021 - July 2023

- Studied and characterized interactions between excitonic states in self-assembled InAs/GaAs CQDs and charge states in adjacent single or coupled quantum dots.
- Analyzed the spectroscopic data with a simple point charge Coulomb interaction model to estimate the radial distance to the interacting charge.

Tamm Plasmon (TP) in 1D Multi-layer Stack and Application in Vertical Cavity Laser
Mentored by Prof. R Vijaya, Department of Physics, IIT Kanpur Aug 2019 - March 2020

- Built and validated tunable photonic cavity systems, matching experimental optical response (angle-dependent reflection/transmission) with theoretical predictions.
- Systematically optimized material composition (dye concentration in polymer matrix) to eliminate self-absorption and maximize emission efficiency.
- Achieved 10-fold narrowband ($\sim$ 15 nm) emission enhancement with $\sim$ 100 nm tunability, demonstrating scalable control over light–matter interactions.

Awards

- Travel award, Convergence of Nano-engineered Devices for Environmental and Sustainable Applications (CONDESA) center, $1000 (2022)
- Department Summer Fellowship, Physics Department at UC Merced, $ 21,600 (2021-23).
- Awarded INSPIRE Scholarship by Government of India. (2015-2017)

Technical Workshops

- Attended a cross-disciplinary training program organized by the Integration of Modern Optoelectronic Materials on Demand (IMOD) center at the University of Washington (2023).
- Participated in the Convergence of Nano-engineered Devices for Environmental and Sustainable Applications (CONDESA) incubator at University of California Merced (2022).

Mentorship Experience

Graduate Mentor, Undergraduate Research Opportunities Center (UROC)
UC Merced May - Aug, 2024

- Conducted a 10-week workshop on science communication and effective research practices. Developed various sessions, including "Poster Presentation 101", "Basic Python Bootcamp", and "Graduate Application Workshop".
- Reviewed research poster/presentation for the end of summer symposium and statements for fellowship/graduate school applications; leading to improved research engagement & providing a head start towards graduate education.

Abstract

Role of Charged Facets and Surface States in Colloidal Quantum Dot Spectroscopy

by Adityaa Bajpai

This thesis examines how surface chemistry - ligation, surface stoichiometry, and the resulting internal electric fields - shapes the static spectroscopy and radiative dynamics of CdTe quantum dots, and extends this framework to interpret the complex photophysics and dynamics in AIGS dots that also result from local symmetry breaking via local electric fields.

The first study presents internal electric fields due to surface charges as a source for symmetry breaking and tuning the exciton fine structure. Polarized photoluminescence excitation (PLE) anisotropy, photoluminescence Stokes shift, and radiative lifetimes of CdTe QDs capped with charged octadecyl phosphonic acid (ODPA) and then ligand exchanged to weakly charged octanethiol ligands are reported. This data is utilized to probe the fine structure and demonstrate that charged ligands increase the fine structure splittings and mix oscillator strength into the lower-energy states. The two-parameter effective mass model of Efros *et al.* describes these trends qualitatively but not quantitatively, indicating lower-symmetry internal electric field perturbations play a larger role than the model assumes.

The second study addresses the continuum absorption, specifically focusing on the contribution that extends all the way down to the lowest exciton in II-VI QDs. By taking CdTe surfaces from cadmium-rich to tellurium-rich stoichiometry, it establishes a link between surface dangling bonds and the continuum intensities. This work shows the continuum comprises two physically distinct contributions: a low-energy component from transitions between occupied surface chalcogenide dangling-bond states and conduction band levels, and a higher-energy component, consisting of bulk-like transitions. An electron tunneling model explains the previously reported spectroscopy of selenium-rich ZnSe and CdSe QDs. Analogous transitions involving alkylthiol ligand lone pairs generalize the framework beyond inorganic surface states.

The third study examines the photophysics and radiative dynamics of high quantum -yield $AgIn_xGa_{1-x}S_2$ (AIGS) QDs, with multi component exponential decays. Using EDX linescan analysis and a growth-kinetics model, the radial composition profile of each cation is determined and used to build Monte Carlo atomistic structures. Effective mass wavefunction calculations show holes localize in randomly distributed silver-rich regions. This study evaluates several competing physical mechanisms, including variations in electron–hole overlap, defect-mediated delayed emission, and internal electric-field inhomogeneities to explain the radiative properties.

Together, these studies show that surface chemistry, internal electric fields due to lingands, and structural disorder are central to the photophysics of these systems.

1 Introduction to Colloidal Quantum Dots

Decades of research on colloidal quantum dots have led to the development of nanocrystals with near unity emission quantum yields and narrow emission linewidths, realized for a wide range of wavelengths. These properties have drawn interest in applying colloidal quantum dots in display technology [1, 2], lasers [3, 4], light emitting diodes [2], medical imaging [5], and biological research [6]. There has also been some interest in the quantum optical properties of the colloidal dots for quantum information and quantum sensing applications [7–10]. These applications require the development of quantum dots with engineered optical properties, which can be synthetically controlled by varying the selection of core/shell material, morphology and growth parameters.

The radiative dynamics and optical selection rules in semiconductor quantum dots (QDs) are governed by the excitonic fine structure, is typically treated as an intrinsic property of nanocrystal shape and composition. The role of internal electric fields originating from surface ligands as an additional source of perturbation to the fine stricture is largely overlooked. A similar aspect of the role of surface chemistry in the bulk spectroscopy of these dots has also been over looked. The broad continuum transitions are understood in terms of bulk like transitions that only show up at higher energies. While that is accurate, this definition doesn't account for the lower energy portion of these transitions. The presence of near band edge continuum transitions that can be tuned by engineering the surface chemistry of these dots is of significance to electroluminescent QLED applications since these surface states can be engineered to make the carrier injection efficient. These states are also relevant to any studies of the fine structure that utilizes polarization of the absorption/emission or Raman signature since these continuum transitions can heavily drown out the signal of interest depending on the energy region of interest. Understanding these effects is important for a more complete understanding of synthetic levers on photophysical properties specifically for developing predictive models for designing QDs for optoelectronic devices.

There have been a number of studies of the fine structure of II-VI and III-V colloidal dots [11–14]. A good proportion of these studies are single particle studies where the individual emission lines from the fine structure states are easily resolvable. However, these studies may be tainted by contributions from charged excitonic states, formed due to prolonged excitation, that may get mis-assigned as the neutral exciton fine structure splittings, making these studies unreliable. A number of ensemble temperature dependent radiative decay studies [13–15] have been employed to study the lowest

fine structure states and the splitting between them. However, the small splittings (∼4-6 meV) obtained in these studies don't reconcile with polarization selective measurements performed on the upper manifold of fine structure in similar dots that would require a much larger fine structure splitting (∼ 20-30 meV) [16]. We investigate the nature of fine structure via ensemble measurements, as opposed to more commonly used single particle measurements, since ensemble properties are more relevant from a device application perspective. This measurement provides an independent probe for the fine structure, shedding light on its true nature and the shortcomings of the Efros model [17] that is used to understand it.

1.1 Electronic Structure & Photophysics

This thesis primarily works with II-VI semiconductors, where the cation is a metal from group IIb and the anion from group VIa of the periodic table. Most II-VI semiconductor materials have a zincblende crystal structure at room temperature and pressure [18]. The electronic band structure of a bulk II-VI semiconductor is shown in Figure 1.1(a). A typical transition in II-VI semiconductors takes an electron p-type valence band to an s-type conduction band. The promotion leaves a hole behind in the valence band. There are three types of holes – heavy hole (HH), light hole (LH), and split-off hole (SO) – distinguished by the effective masses (m_{eff}) and spin states [19].

$$\frac{1}{m_{\text{eff}}} = \frac{1}{\hbar^2}\frac{d^2E(k)}{dk^2} \tag{1.1}$$

The valence band edge is a 4-fold degenerate heavy hole and light hole band. The spin-orbit coupling separates the split-off hole from the heavy-hole and light-hole manifold. The spin-orbit splitting in the case of II-VI quantum dots ranges from $70 - 900$ meV [20, 21]. The optical properties of semiconductor nanocrystals are partly due to the electronic band structure's direct band gap and the nanocrystal's quantum confinement. The quantum mechanical behavior of the electron/hole in the nanocrystal can be best understood by considering a particle trapped in a spherical potential well [17, 22]. Atom-like wavefunctions describe the wavefunction of the carriers as shown in equation(1.2).

$$\Psi^{e/h}_{nlm} = N_{nlm} j_l(\alpha_{n,l} r/a) Y_{lm}(\theta, \phi) \tag{1.2}$$

Here $\alpha_{l,n}$ is the n^{th} root of the Bessel function of the first kind (j_l), and a is the size of the potential well. Like atomic orbitals, the numbers n, l, and m represent the principal, azimuthal, and magnetic quantum numbers. These envelope functions are referred to in the atomic wavefunction notation (i.e., 1S, 2S, 2P, etc.). The energy corresponding to this wavefunction is given by:

$$E = \frac{\hbar^2 \alpha^2_{l,n}}{2m_{\text{eff}}a^2} \tag{1.3}$$

This equation demonstrates the size dependence of electron and hole energy levels in quantum dots; the smaller the dot, the larger the confinement and the higher the energy levels. The precise modeling of the electron and hole wavefunction will need a more detailed description that includes the contributions from the electron (hole) Bloch functions and the envelope functions discussed in this section.

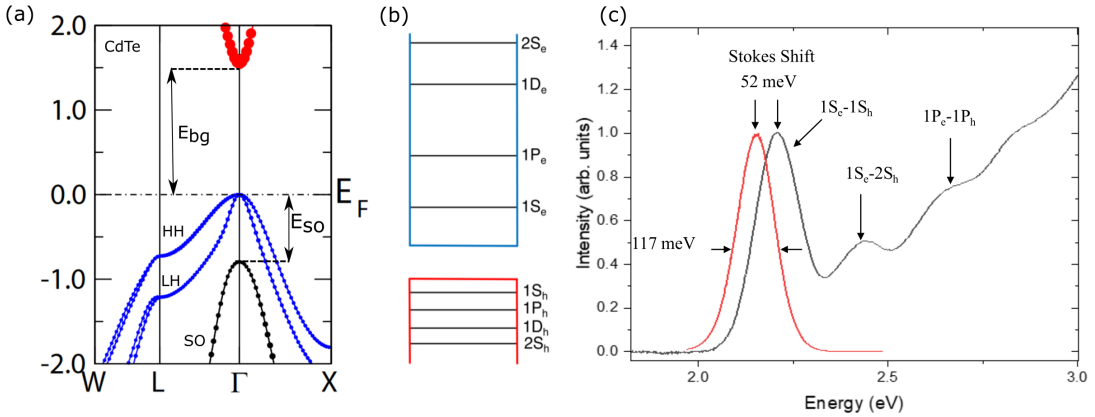


FIGURE 1.1: (a) The electronic band structure of bulk CdTe crystals adapted from [21], (b) the potential wells that confine the electrons and holes and the respective envelope wavefunction energies, and (c) the absorption (black) and emission (red) spectra of CdTe dots synthesized in our lab, showing the different quantum confined transitions between respective electron-hole envelope functions, the Stokes shift (52 meV), and the emission linewidth (117 meV).

The absorption spectra of CdTe in Figure 1.1 (c) show features corresponding to the transition between the electron and hole envelope functions. The Figure also shows the emission spectrum (red) and has a line width (σ_{obs}) of 117 meV. The emission line width of single CdSe particles (σ_{S}) ranges around $50 - 60$ meV [11, 14]. The particle size dispersion (σ_{E}) broadens the ensemble emission in accordance with the equation, $\sigma_{\text{obs}} = \sqrt{\sigma_{\text{S}}^2 + \sigma_{\text{E}}^2}$, the two contributions can be discerned by a wavelength dependent photoluminescence excitation measurements that will be described in the next chapter [23]. The emission peak and the $1S_e - 1S_h$ absorption peak in Figure 1.1(c) are separated by about 52 meV. This shift is called the Stokes shift, which arises from the fine structure of the lowest excitonic state. A typical Stokes shift for CdTe/CdSe ranges from $40 - 60$ meV [17, 24, 25]. The upcoming sections discuss the fine structure and its importance to the photophysics of colloidal quantum dots in greater detail.

1.2 Colloidal Synthesis

The first few syntheses of semiconductor nanocrystals reported in the literature were Louis Brus's synthesis of cadmium sulfide in aqueous solution [22, 26] and Alexei Ekimov's synthesis of copper chloride in glass matrices. These syntheses had broad size

distributions, poor crystallinity, and defect-riddled surfaces that quenched their fluorescence. Moungi Bawendi's group developed the hot-injection method, rapidly injecting organometallic precursors into a non-metal precursor to trigger a burst of nucleation followed by controlled growth [27–29]. This produced nearly monodisperse CdSe quantum dots with sharp, tunable emission, and it remains the foundation of colloidal synthesis today. Xiaogang Peng and Paul Alivisatos replaced the pyrophoric dimethylcadmium precursor with stable cadmium oxide as the metal precursor, making synthesis more accessible and scalable [30–32].

We employ a similar method to synthesize quantum dot samples in our lab. A typical CdTe synthesis starts with a hot injection of a tellurium precursor into a cadmium precursor at high temperatures ($\sim 250\ ^{o}$C). The tellurium precursor consists of tellurium (tri) octyl phosphine (TOP-Te) in octadecene (ODE). The cadmium precursor is synthesized by reacting cadmium oxide with oleic acid to form cadmium oleate in ODE. The cadmium precursor is heated at $120\ ^{o}$C under a vacuum to boil off water from the precursor before hot injection. The Cd-precursor is heated to $250 - 260\ ^{o}$C, and a hot injection is performed. The time of growth and the concentrations of Cd/Te-precursors dictate the growth of the nanocrystals.

The synthesis method described above is one of many methods that produce zincblende particles. This reaction can be tweaked to produce wurtzite particles by using appropriate ligands that bind to all crystal faces by the [111], which results in faster growth in this direction. These reactions are also carried out at higher temperatures ($\sim 300\ ^{o}$C) since the wurtzite structure is more stable at those temperatures. In this work we will mostly be working on zincblende particles.

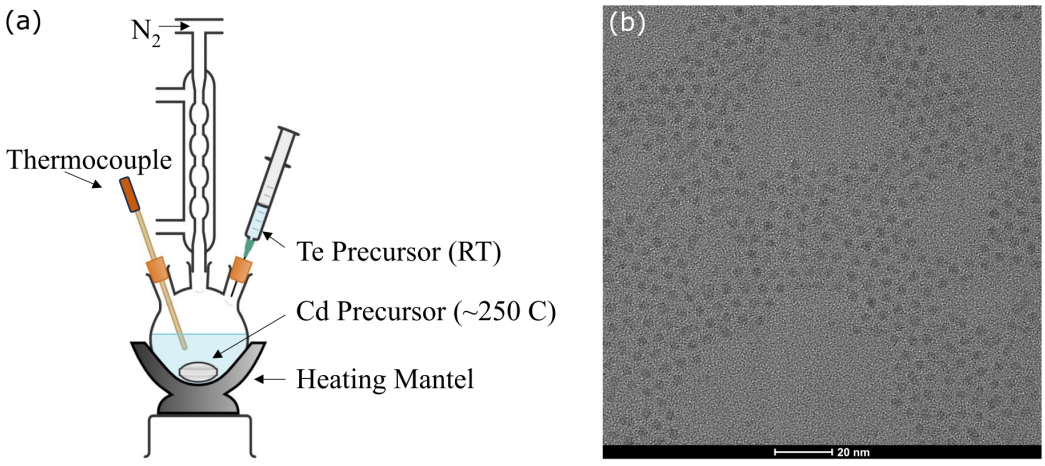


FIGURE 1.2: (a) A schematic of the colloidal synthesis method showing tellurium precursor being injected into the three-neck flask containing the cadmium precursor and connected to a Schlenk line keeping the reaction under a constant flow of Nitrogen (b) shows a TEM scan of a sample of CdSe dots (roughly 3 nm in diameter) synthesized by Fernanda Pilla Bardela.

The TOP and oleic acid in the Te/Cd-precursor end up on the surface of the nanocrystal on separate facets based on the end atoms on a particular facet. The Te/Cd-precursor can be engineered to produce a desirable ligation in the final nanocrystals. Another way of obtaining desirable ligation is by performing a ligand exchange[33]. A ligand exchange relies on Le Chatelier's principle, which dictates the reaction rates for reversible reactions. The principle states the reaction rate shifts in a way that resists any change in the equilibrium. So if the ligand concentration in solution is reduced, the equilibrium shifts such that more ligands leave the surface of the nanocrystals to increase the concentration in the solution. On the other hand, if a larger concentration of a replacement ligand is added to the solution, the equilibrium moves to place them on the surface of the nanocrystals. This process is sped up by increasing the temperature at which the ligand exchange takes place to 120 ^{o}C instead of room temperature (25 ^{o}C).

1.3 Excitonic Fine Structure

The particle-in-a-spherical-well model is an excellent approximation for understanding the size dependence of the electron and hole energy levels and the different transitions observed in the emission and absorption spectra. Early work by Louis Brus [22] on the theoretical description of quantum-confined levels applies effective mass approximation (EMA) onto a particle in a sphere model to describe the size dependence of exciton energies and the oscillator strength of the lowest exciton. For a closer understanding of the fine structure and its relationship with the photophysics of these quantum dots, we must consider the Bloch wavefunctions of the carriers and Exchange interactions.

As mentioned in the prior section, the conduction (valence) band in II-VI quantum dots is an s-type (p-type) wavefunction. The Bloch's theorem defines the wavefunctions for particles in periodic potentials is given by:

$$\psi(x) = e^{ikx}u(x) \tag{1.4}$$

The equation contains the free particle wavefunction (e^{ikx}) shaped by the functions ($u(x)$) that have the same periodicity as the crystal lattice. The Bloch functions are a linear combination of participating orbitals of the individual atoms in the crystal. In the case of II-VI semiconductors, the Bloch functions for the valence bands are represented by X, Y, and Z, which correspond to the linear combination of p_x, p_y and p_z orbitals of the non-metal atom (S, Se, Te, etc.). The conduction band Bloch function is represented by S, a combination of s-orbitals from the metals (Cd, Zn, etc.). These Bloch functions also possess the angular momentum properties of their respective atomic orbitals. Therefore the, S, $X \pm iY$, and Z Bloch functions can be re-written in terms of their L, L_z quantum numbers (l, m) – $|0,0\rangle$, $|1,\pm1\rangle$ and $|1,0\rangle$ respectively.

When an electron is promoted to the conduction band, this results in the mixing of the angular momentum of the Bloch function and the electronic spin state. In the case of an electron in the conduction band the wavefunction is given by:

$$|S\alpha\rangle = |S\rangle \times \left|\frac{1}{2}, \pm\frac{1}{2}\right\rangle, \ \alpha = +\frac{1}{2}, \ \beta = -\frac{1}{2} \tag{1.5}$$

In the case of the unpaired electron left behind in the valence band, this mixing of the Bloch function angular momentum and electronic spin gives rise to three types of holes – heavy hole ($|\frac{3}{2}, \pm\frac{3}{2}\rangle$), light hole ($|\frac{3}{2}, \pm\frac{1}{2}\rangle$) and split-off hole ($|\frac{1}{2}, \pm\frac{1}{2}\rangle$). The heavy hole and light hole bands are degenerate, and the split-off band is separated from the heavy/light hole manifold due to spin-orbit coupling effects. In II-VI semiconductors, the spin-orbit splitting is of the order of $70 - 900$ meV. Therefore, a mixture of heavy and light hole states contribute to the band edge excitons. The Bloch functions corresponding to heavy and light holes are given by:

$$\begin{aligned} u_{+3/2} &= \frac{1}{\sqrt{2}}[X + iY] \left|\frac{1}{2}, +\frac{1}{2}\right\rangle, \ u_{+1/2} = \frac{1}{\sqrt{6}}[X + iY] \left|\frac{1}{2}, -\frac{1}{2}\right\rangle - \frac{2}{\sqrt{6}} Z \left|\frac{1}{2}, +\frac{1}{2}\right\rangle \\ u_{-3/2} &= \frac{1}{\sqrt{2}}[X - iY] \left|\frac{1}{2}, -\frac{1}{2}\right\rangle, \ u_{-1/2} = \frac{1}{\sqrt{6}}[X - iY] \left|\frac{1}{2}, +\frac{1}{2}\right\rangle + \frac{2}{\sqrt{6}} Z \left|\frac{1}{2}, -\frac{1}{2}\right\rangle \end{aligned} \tag{1.6}$$

The carrier wavefunctions in II-VI nanocrystals were worked out by Efros et al. [17] as a mixing of envelope functions with the respective Bloch functions. The rest of this section summarizes an adapted form of that work to provide necessary background for the thesis. The doubly degenerate electron wavefunction is given by:

$$\begin{aligned} \Psi_e &= \sqrt{\frac{2}{a}} \frac{Sin[\pi r/a]}{r} Y_{00} \, |S\alpha\rangle \\ E_{1S_e} &= \frac{\hbar^2 \pi^2}{2 m_e a^2} \end{aligned} \tag{1.7}$$

The four-fold degenerate hole wavefunctions looks like:

$$\Psi_M(r) = 2 \sum_{l=0,2} R_l(r) (-1)^{M-3/2} \times \sum_{m+\mu=M} \begin{pmatrix} 3/2 & l & 3/2 \\ \mu & m & -M \end{pmatrix} Y_{lm}(\Omega) u_\mu(r) \tag{1.8}$$

Here, R_l is the radial function, Y_{lm} are spherical harmonics, Ω are angular coordinates (θ, ϕ), $u_\mu(r)$ are the Bloch functions corresponding to the light and heavy holes ($\mu = \pm 3/2, \pm 1/2$), and $\begin{pmatrix} 3/2 & l & 3/2 \\ \mu & m & -M \end{pmatrix}$ are the Wigner $3j$ symbols represented with $W_{\mu,m,-M}$ in the following equations. The full heavy and light hole wavefunctions are

given by:

$$\begin{aligned}
\Psi^h_{3/2} &= \sqrt{2}R_0(r)W_{0,0,3/2}Y_{0,0}(\Omega)u_{3/2} - \sqrt{2}R_2(r)[W_{2,0,3/2}Y_{2,0}(\Omega)u_{3/2} \\
&\quad + W_{2,1,1/2}Y_{2,1}(\Omega)u_{1/2} + W_{2,2,-1/2}Y_{2,2}(\Omega)u_{-1/2}] \\
\Psi^h_{-3/2} &= -\sqrt{2}R_0(r)W_{0,0,-3/2}Y_{0,0}(\Omega)u_{-3/2} + \sqrt{2}R_2(r)[W_{2,0,-3/2}Y_{2,0}(\Omega)u_{-3/2} \\
&\quad + W_{2,-1,-1/2}Y_{2,-1}(\Omega)u_{-1/2} + W_{2,-2,1/2}Y_{2,-2}(\Omega)u_{1/2}] \\
\Psi^h_{1/2} &= -\sqrt{2}R_0(r)W_{0,0,1/2}Y_{0,0}(\Omega)u_{1/2} + \sqrt{2}R_2(r)[W_{2,0,1/2}Y_{2,0}(\Omega)u_{1/2} \\
&\quad + W_{2,1,-1/2}Y_{2,1}(\Omega)u_{-1/2} + W_{2,2,-3/2}Y_{2,2}(\Omega)u_{-3/2} + W_{2,-1,3/2}Y_{2,-1}(\Omega)u_{3/2}] \\
\Psi^h_{-1/2} &= \sqrt{2}R_0(r)W_{0,0,-1/2}Y_{0,0}(\Omega)u_{-1/2} - \sqrt{2}R_2(r)[W_{2,0,-1/2}Y_{2,0}(\Omega)u_{-1/2} \\
&\quad + W_{2,-1,1/2}Y_{2,-1}(\Omega)u_{1/2} + W_{2,-2,3/2}Y_{2,-2}(\Omega)u_{3/2} + W_{2,1,-3/2}Y_{2,1}(\Omega)u_{-3/2}]
\end{aligned} \tag{1.9}$$

The hole Bloch function can be written in terms of the electron spin (α or β) and the spherical harmonics and a radial function (U(r)) of the p-type conduction band [34]:

$$\begin{aligned}
u_{3/2} &= U(r)Y_{1,+1}(\Omega)\alpha \\
u_{-3/2} &= U(r)Y_{1,-1}(\Omega)\beta \\
u_{1/2} &= \frac{1}{\sqrt{3}}U(r)Y_{1,1}(\Omega)\beta + \sqrt{\frac{2}{3}}U(r)Y_{1,0}(\Omega)\alpha \\
u_{-1/2} &= \frac{1}{\sqrt{3}}U(r)Y_{1,-1}(\Omega)\alpha + \sqrt{\frac{2}{3}}U(r)Y_{1,0}(\Omega)\beta
\end{aligned} \tag{1.10}$$

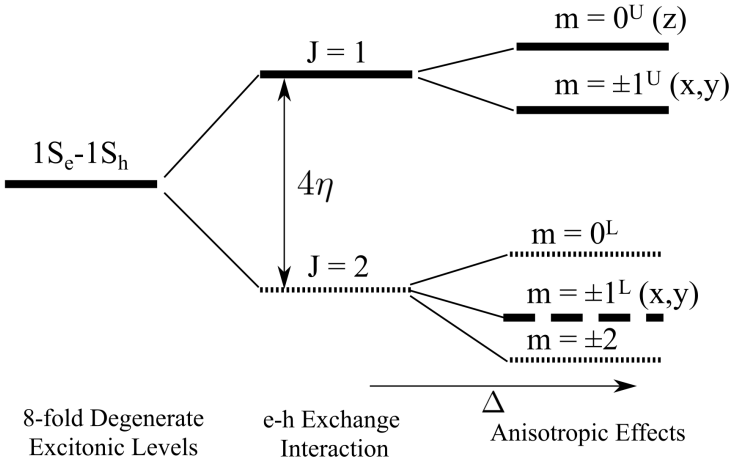


FIGURE 1.3: The electronic fine structure of the $1S_e - 1S_h$ transition showing the e-h exchange splitting and effects of anisotropies in the nanocrystals

The exciton wavefunctions are given in Efros' 2010 paper [35]:

$$\begin{aligned}
\psi_2 &= \Psi^h_{3/2}\alpha \\
\psi_{-2} &= \Psi^h_{-3/2}\beta \\
\psi^U_1 &= -C^+\Psi^h_{1/2}\alpha + C^-\Psi^h_{3/2}\beta \\
\psi^L_1 &= C^-\Psi^h_{1/2}\alpha + C^+\Psi^h_{3/2}\beta \\
\psi^U_{-1} &= -C^-\Psi^h_{-3/2}\alpha + C^+\Psi^h_{-1/2}\beta \\
\psi^L_{-1} &= C^+\Psi^h_{-3/2}\alpha + C^-\Psi^h_{-1/2}\beta \\
\psi^{U,L}_0 &= \frac{1}{\sqrt{2}}[\pm\Psi^h_{-1/2}\alpha + \Psi^h_{1/2}\beta]
\end{aligned} \tag{1.11}$$

Where $C^\pm$ are written in terms of $b = (-2\eta + \Delta)/2$ and $d = 3\eta^2$ defined earlier:

$$C^\pm = \sqrt{\frac{\sqrt{b^2+d} \pm b}{2\sqrt{b^2+d}}} \tag{1.12}$$

Using equations (1.9-1.11), one could write the exciton wavefunctions in terms of the radial functions, spherical Bessel functions, and two-electron spin wavefunctions (the arguments of the radial functions and the spherical harmonics have been omitted for brevity):

$$\begin{aligned}
\psi_2 &= \frac{R_0 + R_2}{\sqrt{2}}\, Y_{00}Y_{11}\,\alpha\alpha \\
\psi_{-2} &= \frac{R_0 + R_2}{\sqrt{2}}\, Y_{00}Y_{1-1}\,\beta\beta \\
\psi^U_1 &= (R_0+R_2)\left(\frac{C^+Y_{00}Y_{10}}{\sqrt{3}}\alpha\alpha - \frac{C^-Y_{00}Y_{11}}{\sqrt{2}}\alpha\beta + \frac{C^+Y_{00}Y_{11}}{\sqrt{6}}\beta\alpha\right) \\
\psi^L_1 &= (R_0+R_2)\left(\frac{C^-Y_{00}Y_{10}}{\sqrt{3}}\alpha\alpha + \frac{C^+Y_{00}Y_{11}}{\sqrt{2}}\alpha\beta + \frac{C^-Y_{00}Y_{11}}{\sqrt{6}}\beta\alpha\right) \\
\psi^U_{-1} &= (R_0+R_2)\left(-\frac{C^+Y_{00}Y_{10}}{\sqrt{3}}\beta\beta + \frac{C^+Y_{00}Y_{1-1}}{\sqrt{6}}\alpha\beta - \frac{C^+Y_{00}Y_{1-1}}{\sqrt{2}}\beta\alpha\right) \\
\psi^L_{-1} &= (R_0+R_2)\left(\frac{C^-Y_{00}Y_{10}}{\sqrt{3}}\beta\beta + \frac{C^-Y_{00}Y_{1-1}}{\sqrt{6}}\alpha\beta + \frac{C^-Y_{00}Y_{1-1}}{\sqrt{2}}\beta\alpha\right) \\
\psi^{U,L}_0 &= (R_0+R_2)\left(\frac{Y_{00}Y_{1-1}}{2\sqrt{3}}\alpha\alpha \pm \frac{Y_{00}Y_{11}}{2\sqrt{3}}\beta\beta \mp \frac{Y_{00}Y_{10}}{\sqrt{6}}\alpha\beta + \frac{Y_{00}Y_{10}}{\sqrt{6}}\beta\alpha\right)
\end{aligned} \tag{1.13}$$

The 2-fold degenerate electronic and 4-fold degenerate hole states form the 8-fold degenerate excitonic levels that make the $1S_e - 1S_h$ transitions. A perfectly spherical zincblende quantum dot of CdTe would have the 3-fold degenerate states ($J = 1, m_J = 0, \pm 1$) and the 5-fold degenerate ($J = 2, m_J = 0, \pm 1, \pm 2$). The lower energy $J = 2$ states are dark states with nearly zero dipole strength, and the higher energy $J = 1$ states are bright with a significant dipole strength. The breaking of the spherical symmetry

further splits these levels into two upper and three lower levels as shown in Figure 1.3. As a result of the anisotropy, the $\pm 1^U$, and $\pm 1^L$ undergo mixing, resulting in a small yet significant oscillator strength in the lower $\pm 1^L$ state. The fine structure energy splitting and the dipole strength of the $\pm 1^L$ are worked out by Efros *et al.* in 1996 [17]. The relevant energies for the fine structure levels are shown below.

$$\begin{aligned} E_1^{U/L} &= \eta/2 \pm \sqrt{(2\eta - \Delta)^2/4 + 3\eta^2} \\ E_0^{U/L} &= \eta/2 + \Delta/2 \pm 2\eta \\ E_2 &= -3\eta/2 - \Delta/2 \end{aligned} \tag{1.14}$$

$\eta = (a_{ex}/a)^3 \hbar\omega_{ST}\chi$ is a measure of the electron-hole exchange, χ is the overlap integral of the electron-hole envelope functions, Δ is the light/heavy hole splitting, and is very sensitive to the anisotropy that breaks the spherical symmetry. The transition oscillator strengths of the only bright states are given by:

$$f_{1L/U} = \frac{2K\tilde{P}^2}{9} \frac{2\sqrt{b^2+d} \mp b \pm \sqrt{3d}}{2\sqrt{b^2+d}}, \quad f_{0U} = \frac{4K\tilde{P}^2}{9} \tag{1.15}$$

Where, $K = \frac{2}{a}|\int drrsin(\pi r/a)R_0(r)|^2$, $\tilde{P}^2 = \frac{2\lambda}{3mch}|\langle S|\, p_z\, |Z\rangle\,|^2$, m and e are the mass and charge of the electron, λ is the wavelength corresponding to the transition, $b = (-2\eta + \Delta)/2$, and $d = 3\eta^2$. The transitions to 0^L and ± 2 are spin-forbidden; hence, their oscillator strengths are zero.

Anisotropy can be introduced into the system in two ways: (1) by changing the internal crystal structure at the unit cell level, i.e. by introducing a unique axis as in the case of a wurtzite structure and (2) by changing the morphology of the dots. Chapter 2 will demonstrate that ligand fields can also contribute to symmetry breaking at a macroscopic level. The prior effect is represented by the term Δ_{CFS} (crystal field component) and the latter by Δ_{shape}

$$\Delta = \Delta_{\text{CFS}} + \Delta_{\text{shape}} \tag{1.16}$$

Efros' work sums up the fine structure splitting and their transition dipole strengths in terms of η and Δ that connect them to some material properties (ω_{ST}, $\tilde{P}$), the size of the quantum dots (a) and the anisotropy. It shows that the photophysical properties of these dots are inseparably enmeshed with the fine structure and shape anisotropy.

1.4 Spectroscopy of Quantum Dots

Static photoluminescence (PL) and absorption spectroscopy are standard means of characterizing quantum dot samples. In PL spectroscopy, the quantum dot sample is excited by a spectrally narrow source of light at about 400 nm or 3.1 eV to a high-energy excited state. The exciton created relaxes to the band edge, where it eventually recombines and emits a photon. The absorption and emission spectra of a 3.2 nm CdTe

quantum dots are shown in Figure 1.1 (c), it shows the first exciton absorption at 2.22 eV and the emission peak is redshifted by about 52 meV known as the Stokes shift. The Stokes shift in molecular spectroscopy is understood in terms of vibrational coupling driven by nuclear reorganization upon photoexcitation. In the case of QDs the Stokes shift is predominantly due to the fine structure splittings, specifically the electron-hole exchange energy that scales as $1/R^3$ [17, 36]. The absorption peak of the lowest exciton ($1S_e - 1S_h$) results from transitions to $\pm 1^U$ and 0^U states that contain most of the oscillator strength. the emission comes from a combination of $\pm 1^U$ and $\pm 1^L$ states, this is a point of contention in the literature. Given that the Boltzmann distribution sufficiently favors the lower energy $\pm 1^L$, most of the luminescence would result from this state. In the next chapter we will show that even though this is true a non-negligible portion of the luminescence comes from the upper manifold.

Not all excitation events lead to radiative recombination since, in some instances, the hole or electron may get trapped in a defect and non-radiatively recombine. These defects can be internal or surface related, most internal defects can be annealed in a high temperature hot-injection synthesis, while the number of surface defects are a function of sufficient surface passivation. Therefore, high-quality samples containing fewer dots with surface defects end up being brighter. This property is quantified by photoluminescence quantum yield (PL QY), which is generally measured in reference to a dye sample with a known $PLQY_{\text{dye}}$.

$$PLQY_{QD} = PLQY_{dye} \frac{I_{QD}}{(1 - T_{QD})} \frac{(1 - T_{dye})}{I_{dye}} \tag{1.17}$$

Where I_{QD} and I_{dye} (T_{QD} and T_{dye}) are the PL intensities (transmitted intensities) of the quantum dot sample and dye, respectively. High PLQYs are very important for display applications and other characterization techniques, such as PLE spectroscopy.

1.5 Photoluminescent Excitation (PLE) Spectroscopy

PLE spectroscopy is another common technique where the PL intensity at a specific detection energy is measured as a function of excitation energy. Choosing a specific detection energy results in probing a narrow selection of the quantum dot population that emits in the observation window. The PLE spectra obtained at different detection wavelengths should differ only slightly with the change in confinement energy associated with emission at each wavelength. The broad features in the PLE spectra follow the features of the absorption spectrum with a narrower line width. In a polarization-selective PLE a polarized excitation beam is incident on the quantum dot sample, exciting all the dots whose excitation dipoles are aligned with the excitation polarization. The PL emission can be polarized parallel or perpendicular relative to the excitation polarization (corresponding intensities referred to as $I_{\parallel}$ and $I_{\perp}$). The emission spectrum is collected and filtered based on polarization, and the extent and direction of the

luminescence polarization is given in terms of the anisotropy, which is defined as[16, 37]:

$$r = \frac{I_{\parallel} - I_{\perp}}{I_{\parallel} + 2I_{\perp}}, \tag{1.18}$$

where $I_{\parallel}$ and $I_{\perp}$ are the luminescence intensities having polarizations parallel and perpendicular to that of the incident light. Anisotropies following excitation of randomly oriented QDs average the absorbing and emitting oscillators over all possible QD orientations. Two limiting cases of relative orientations of the absorbing and emitting oscillators define the limits of the anisotropies that can be obtained here. In the case where the oscillators are coplanar (the $\pm 1^L$ and $\pm 1^U$ planar oscillators), an anisotropy of $r = 0.1$ is obtained. However, when the absorbing and emitting oscillators are perpendicular (the $\pm 1^L$ or $\pm 1^U$ with the 0^U), a negative anisotropy is obtained, $r = -0.2$ [37].

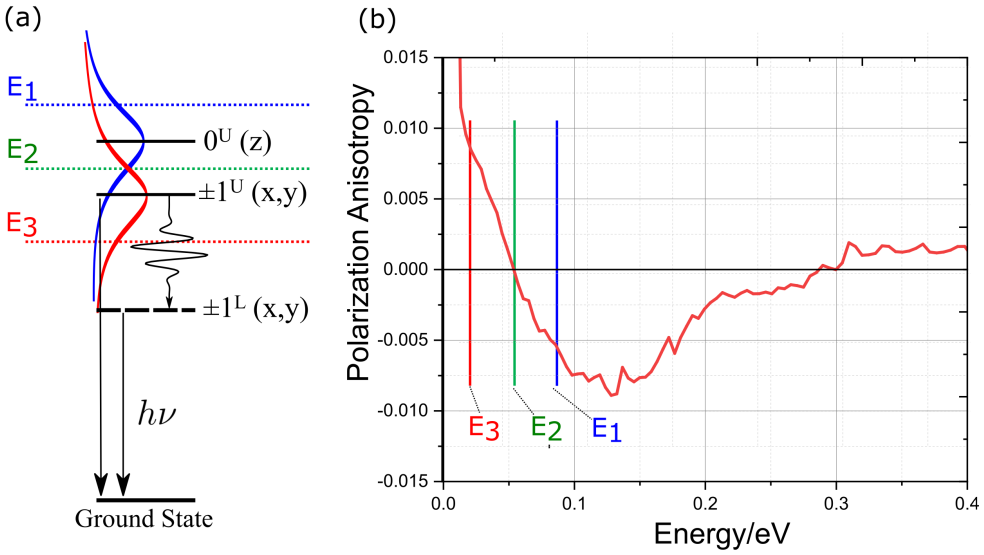


FIGURE 1.4: (a) A level diagram of $1S_e - 1S_h$ transitions. The homogenous dispersion of the 0^U and $\pm 1^U$ levels are represented by the blue and red Gaussian, respectively. The schematic highlights three excitation events at energies E_1, E_2, and E_3. (b) Shows the polarization anisotropy (r) data corresponding to CdTe dots with the three energies marked with vertical lines.

A polarization-selective PLE can bring more insight into the fine structure of the $1S_e - 1S_h$. Transitions from the ground state to the various fine structure states have different polarizations, as indicated in Figure 1.4. At room temperature, thermally equilibrated QDs, most of the PL comes from the partially allowed $\pm 1^L$ states and the more strongly allowed $\pm 1^U$ states, both of which are x, y-polarized. The slightly higher energy 0^U state is z-polarized, orthogonal to the $\pm 1^{L/U}$ states. Because of the orthogonal polarization of the $\pm 1^U$ and 0^U states, static polarization excitation spectroscopy gives a measure of the extent to which these states can be selectively excited. Figure 1.4 (a) shows the participating states of the $1S_e - 1S_h$ exciton and the homogenous linewidth

of the 0^U and $\pm1^U$ states represented by the blue and red Gaussians, respectively. The energies for three excitation events (E_1, E_2, and E_3) are highlighted as examples. Applying the aforementioned limiting cases here, it is possible to interpret the PLE anisotropy data in Figure 1.4(b) in terms of which states are preferentially excited and their relative orientation with respect to the emitting state ($\pm1^L$ and $\pm1^U$). At E_1, 0^U has a higher probability of excitation; therefore, a negative PLE anisotropy is obtained; at E_3, $\pm1^U$ has a higher probability of excitation, and a positive PLE anisotropy is measured. At E_2, both 0^U and $\pm1^U$ have an equal probability of excitation, and therefore, the PLE anisotropy is zero; this marks the centroid of the $\pm1^U$ and 0^U states. If the energy E_2 is measured in reference to the energy of the $\pm1^L$ state, it would represent the Stokes shift. When the difference between the excitation and detection energies is small (less than the splittings or the homogeneous linewidth), the lowest emitting state is primarily excited, and a positive PLE anisotropy is observed. At higher excitation energies (much larger than E_1), most of the excitation is to the higher-lying, more strongly allowed fine structure levels. When the excitation is on the red edge of these bands, the absorption and emission happens through the co-polarized $\pm1^{L/U}$ states, therefore a positive PLE anisotropy is observed.

If the spectral widths of these transitions are known or can be modeled, the excitation wavelength-dependent extent of photoluminescence polarization gives the $\pm1^U/0^U$ splitting. How this splitting is calculated from the polarization-dependent excitation spectra of a room temperature solution of randomly oriented QDs is discussed in greater detail in Chapter 2.

2 Ligand Effects on Fine Structure of CdTe Nanocrystals

2.1 Abstract

This chapter discusses the ligand effects on the angular momentum fine structure of 3.2 nm diameter CdTe quantum dots studied using room temperature static spectroscopy and lifetime measurements. This work was published in The Journal of Chemical Physics [38]. This study focused on the comparison of particles having charged (octadecylphosphonic acid) and uncharged (octanethiol) ligands. In both cases, polarized photoluminescence excitation spectroscopy provides a measure of the extent to which fine structure states having orthogonal polarizations can be selectively excited and the photoluminescence Stokes shift provides a measure of amount of luminescence coming from fine structure states having different energies. Radiative lifetime measurements provide a measure of the relative oscillator strengths of fine structure states having different energies. The results are analyzed in terms of a simple two-parameter effective mass approximation model for quasi-spherical II-VI quantum dots (Efros, et al., Phys. Rev. B 1996, 54, 4843-4856 [17]), which is the 'standard model' of angular momentum fine structure states. We find that this standard model qualitatively explains the results. However, quantitative analysis of these results gives a significant deviation from the standard model predictions; it requires that the fine structure splittings are smaller and/or more complicated and that the lower energy states have more oscillator strength than predicted by the standard model.

2.2 Introduction

The angular momentum fine structure is central to the spectroscopy and photophysics of II-VI and III-V semiconductor quantum dots (QDs) and controls much of their radiative dynamics. The lowest excitons in strongly quantum-confined II-VI and III-V QDs have very large oscillator strengths and extinction coefficients. Simple radiative lifetime considerations suggest that photoluminescence (PL) from this state should have a very short radiative lifetime. However, these QDs exhibit very long, and strongly temperature-dependent PL decays. Radiative lifetimes are typically tens of nanoseconds at room temperature and much longer at cryogenic temperatures. These long lifetimes are understood in terms of population of dark and bright states in the angular momentum fine structure. The lowest fine structure level (the "dark exciton") is optically forbidden from the ground state, and luminescence occurs by thermal population

of higher energy, optically bright states. The basic theory describing the energies and oscillator strengths of the fine structure states in quasi-spherical particles was first described by Efros *et al.*[17] and this description is the "standard model" for understanding QD spectroscopy. The model is based on using the effective mass approximation to describe an electron and a hole moving under spherical, oblate or prolate confinement. The fine structure model for an oblate particle is summarized in Figure 1.3.

With spherical symmetry, the $J = 1$ and $J = 2$ states are split by the electron-hole exchange interaction and all the oscillator strength is in the upper, $J = 1$ states; the lower $J = 2$ states are optically dark. Quantitative predictions of this splitting are improved by the inclusion of both long- and short-range exchange interactions.[39] This model considers only oblate/prolate nonspherical perturbations, which mixes the optically dark $\pm 1^L$ with the bright $\pm 1^U$ states, giving significant oscillator strength to the former. The symmetry of an oblate/prolate perturbation maintains inversion and rotational symmetry. As a result, the ± 2 and 0^L states remain dark. These qualitative conclusions also follow from group theory considerations of the tetrahedral environment in a zincblende crystal, as described in the Section 2.7.4. This relatively simple

standard model relates the energetic splittings and the amount of oscillator strength in the $\pm 1^L$ states to the deviation from spherical symmetry. However, it only describes the deviation from spherical symmetry in terms of oblate/prolate perturbations; lower symmetry perturbations affect the state mixings and energetic splittings in more complicated ways. This model has been extended to consider the effects of a point charge perturbation on the surface or in the interior of the QD.[40] The analysis is done in the context of the electrostatic potential being expanded in terms of the spherical harmonics and therefore considers perturbations having more general symmetries. One of the conclusions of this study is that a perturbation having D_{2h} or lower symmetry removes the x, y degeneracy and therefore splits both the $\pm 1^L$ and $\pm 1^U$ states. Furthermore, any perturbation that reduces the symmetry to C_s results in J and m_j not being good quantum numbers and all the fine structure states acquire finite oscillator strength. We take the standard model as the starting point for our discussion of the fine structure and will later consider the limitations of the model.

This chapter examines the role of internal electric fields on the fine structure states of CdTe QDs. These fields are produced by surface and ligand charges, and their magnitude depends on the nature (charged or uncharged) of the ligands, the nature of the surface crystal facets, and the polarity of the surrounding solvent. Reference [40] presents calculations showing that charged dopant atoms can have very significant effects on the splittings and mixing of the fine structure states, leading us to expect that the presence of charged ligands on the particle surfaces may also have large effects. The quasi-spherical CdTe particles used here can be ligated with either charged or uncharged ligands on the surface crystal facets. Exchanging charged with uncharged ligands is expected to have large effects on the internal electric fields, and therefore measurable effects on the fine structure states. The three complementary spectroscopic measurements discussed above are used to study the exciton fine structure. The model in Ref [17] allows calculation of the magnitudes of the $\pm 1^L / \pm 1^U$ mixing and the

$\pm 2/\pm 1^L$ and $\pm 1^U/0^U$ splittings in terms of two parameters: the light/heavy hole splitting and the electron/hole exchange interaction. This work presents PLE and polarized-PLE measurements to calculate these parameters and radiative lifetime measurements as an independent method to test this model. The next few sections describe modeling of PLE data and the considerations needed for the calculation of the radiative lifetimes.

2.3 Modeling/Fitting the PL & PLE Data

There are several spectroscopic probes that can be used to assess the fine structure splittings and oscillator strengths of QDs in room temperature solutions. The spectroscopic probes used here are the radiative lifetime, the Stokes shift and the photoluminescence excitation (PLE) anisotropy spectrum. The radiative lifetime depends on the relative populations and oscillator strengths of the different fine structure states. The overall radiative lifetime is simply a Boltzmann weighted average of the lifetimes of all the fine structure states. The Boltzmann population in these states depends on the energetic splittings and the oscillator strengths depend on the extent to which the states are mixed. As a result, the measured radiative lifetime significantly constrains these splittings and mixings. The Stokes shift from an individual state depends on the total (vibrational and solvent) excited state reorganization energy. When absorption and luminescence occur from different states, energy relaxation from the absorbing to the emitting states also contributes to the Stokes shift. Therefore, the Stokes shift depends on the relative amount of absorption and PL from each of the fine structure states, further constraining the relative energies and oscillator strengths. A static photoluminescence excitation (PLE) spectrum measures the photoluminescence intensity as a function of excitation wavelength at a specific detection wavelength. Excitation can be done with polarized light, and the parallel and perpendicularly polarized components of the PL spectrum can also be obtained throughout the excitation wavelengths. This gives a PLE anisotropy spectrum, which is somewhat more complicated to interpret, but essentially provides a measure of the $\pm 1^U/0^U$ splitting compared to the homogeneous linewidth. The crucial point is that a PLE anisotropy spectrum allows discrimination between absorption into the different $J = 1$ states and therefore facilitates determination of the $\pm 1^U/0^U$ splitting, as has been shown in the case of InP/ZnSe/ZnS QDs.[23]

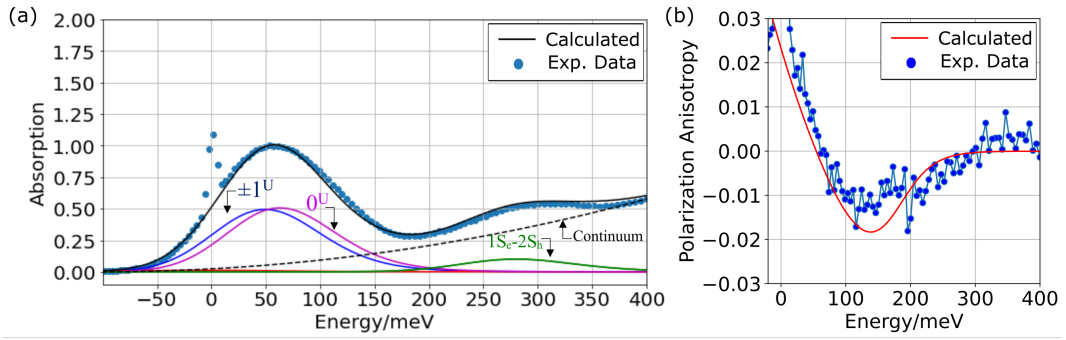


FIGURE 2.1: (a) Shows the experimental static PLE/absorption spectra data (blue circle) of a CdTe sample plotted with respect to energy relative to the PL peak energy and a calculated fit (solid black line). The gaussians corresponding to the $\pm 1^U$ and 0^U states, $1S_e - 2S_h$ transition, and cubic background are represented by the blue, pink, green, and black dashed lines, respectively. (b) The experimental (blue markers) and calculated (red solid line) polarization anisotropy data for the same sample are shown.

The PLE anisotropy data can be modeled using a linear combination of anisotropy values for the $\pm 1^U$ and $\pm 0^U$ states, given by $r_{\pm 1} = 0.1$ and $r_0 = -0.2$ respectively, weighted with their respective relative excitation probabilities. The relative excitation probability can be modeled by two Gaussians ($G_{\pm 1}$ and $G_0(E)$) with peaks at E_{1U} and E_{0U} given by equation ((1.14)). The observed final PLE anisotropy at a given excitation energy E can be calculated by the expression:

$$r_{obs} = \frac{2r_{\pm 1}G_{\pm 1}(E) + r_0 G_0(E)}{2G_{\pm 1}(E) + G_0(E)} \tag{2.1}$$

where, $G_{\pm 1}(E) = S_{\pm 1} \exp\left[-(E - E_{1U})^2/2\sigma_U^2\right]$ and $G_0(E) = S_0 \exp\left[-(E - E_{0U})^2/2\sigma_U^2\right]$. The factor of two in the terms corresponding to $\pm 1^U$ state is due to the fact that it is doubly degenerate. This equation introduces three more independent variables: the widths of the transitions σ_U, the individual amplitudes of the two states $S_{\pm 1}$ and S_0. The ratio of the amplitudes is equal to the ratio of the respective oscillator strengths.

$$\frac{S_0}{S_{\pm 1}} = \frac{f_{0U}}{f_{1U}} \tag{2.2}$$

The ratio of oscillator strengths is equal to the ratio of the respective transition probabilities from equation((1.15)) and can be calculated from η and Δ. The Stokes shift depends on the line width (σ_U), the relative amplitudes $S_{\pm 1}$, S_0, η and Δ. Therefore, fitting the static PLE will give us a good starting value for all of these parameters. these values have a small wiggle room. For example, small changes η would reduce the calculated Stokes shift, but it can be made up by an increase in Δ pushing the Stokes shift back to the original value. It should be noted that the variables aren't entirely free but rather have a contour in parameter space where they can fit the static PLE spectrum. Figure 2.1 (a) shows the experimental static PLE data for a CdTe sample (blue circles) and a fit (black line) produced by the two Gaussians corresponding to the $\pm 1^U$

and 0^U states (blue and pink lines respectively), a gaussian corresponding to $1S_e - 2S_h$ transition (green) and a cubic background (black dashed line). The $1S_e - 2S_h$ and the unassigned background transition are added to the fit to fully fit the observed data and reduce any extra wiggle room in parameter space.

The parameters obtained with this fit serve as a starting point to fit the PLE anisotropy data. The slope of the PLE anisotropy data around the first zero ($0 - 100$ meV region), the x-intercept, and the peak value on either side are all dependent on the splitting between $\pm 1^U$ and 0^U states and their linewidths. Figure 2.1(b) shows the experimental PLE anisotropy data (pink circle) and the calculated PLE anisotropy data (red line). The final set of parameters obtained upon fitting both the static PLE and PLE anisotropies are $\sigma_U = 51$ meV, $\eta = 16$ meV, and $\Delta = 18$ meV. The splitting between $\pm 1^U$ and 0^U states calculated from equation(1.14) is 12.4 meV and a calculated Stokes shift of 63.4 meV.

2.4 Determination of the Homogeneous Linewidth

PLE measurements can also be informative on the homogeneous and inhomogeneous linewidths of a sample. The PL/PLE spectra of ODPA ligated CdTe QDs with the observation window spanning across the PL band is shown in Figure 2.2. The PL spectrum can fit with a gaussian to obtain a width of 27.4 meV (σ_{total}). Panel (b) of Figure 2.2 shows $1S_h$-$1S_e$ peak energy as a function of the detection energy extracted from the PLE also showing a linear fit with a slope of 0.527. The slope of the $1S_e$-$1S_h$ peak vs detection energy plot and the total line width can be used to discern the homogeneous and inhomogeneous spectral widths similar to the one used in Cavanaugh *et al.*[23]

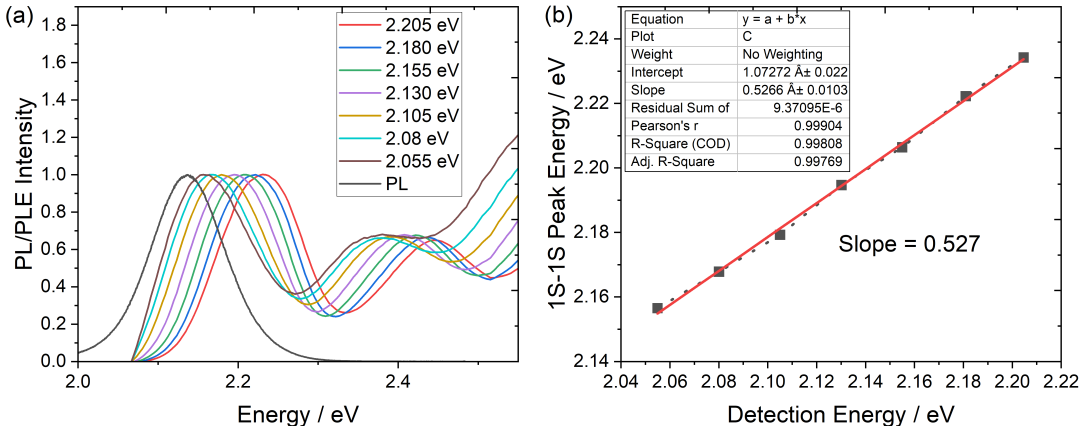


FIGURE 2.2: PL/PLE spectra of the ODPA ligated CdTe particles with the PLE spectra and (b) 1S-1S peak energy and a function of detection energy (black squares) and a linear fit (red line) showing a slope of 0.527.

Plugging the total width in the equation:

$$\frac{\sigma_I^2}{\sigma_{\text{total}}^2} = 0.527, \tag{2.3}$$

gives a inhomogeneous width (σ_I) of 34.6 meV. Given that the square of the total width is a sum of the square of the homogeneous and inhomogeneous widths the former can be calculated to be 32.8 meV, corresponding to a homogeneous full-width-half-maximum of 77.2 meV.

2.5 Radiative Lifetime Calculations

Anisotropy also affects the radiative lifetimes of quantum dots. The mixing of $\pm 1^U$ state with $\pm 1^L$ due to the breaking of spherical symmetry redistributes the oscillator strength in the lowest emitting $\pm 1^L$ state. The energy difference between the slightly allowed $\pm 1^L$ and ± 2 states determines the fraction of the population that will end up in the $\pm 1^L$ states. Both of these factors combined determine the radiative lifetime of a quantum dot. Consequently, any change to the fine structure should result in a change in the measured radiative lifetime of the sample. The apparent radiative lifetime (τ_{rad}) can be calculated using the oscillator strengths weighted with the respective Boltzmann factors.

$$\frac{1}{\tau_{rad}} = C\frac{2B_{1L}f_{1L} + 2B_{1U}f_{1U} + B_{0U}f_{0U}}{2B_2 + 2B_{1L} + 2B_{1U} + B_{0U} + B_{0L}},\ B_x = \exp(-E_x/kT) \tag{2.4}$$

Here, $C = \frac{2\pi ne^2}{\varepsilon_0 mc\lambda^2}$, m and e are the mass and charge of the electron, ε_0 is the permittivity of free space. f_{0U}, f_{1U} and f_{1L} are the oscillator strengths of 0^U, $\pm 1^U$, and $\pm 1^L$ states respectively. The Einstein coefficient (A) is the spontaneous emission rate in a two-level system and puts a bound on the oscillator strengths of 0^U, $\pm 1^U$, and $\pm 1^L$ states – f_{0U}, f_{1U} and f_{1L} respectively. As described earlier, the oscillator strength in f_{1L} is obtained by redistributing from f_{1U}. Therefore, the two should add up to be equal to the f_{0U}.

$$C(2f_{1L} + 2f_{1U} + f_{0U}) = A,\ \ f_{1L} + f_{1U} = f_{0U} \tag{2.5}$$

For nondegenerate states of a two-level system, the radiative rate constant is given by reference [41]

$$A = \frac{8\pi\, 0.2303\, n_f^3}{N_A c^2 n_a} \int \frac{\varepsilon(\nu)}{\nu}\, d\nu \approx 2.88 \times 10^{-9} n^2 \bar{\nu}_f^2 \int \varepsilon(\nu)\, d\nu \tag{2.6}$$

which may be written in terms of wavelengths as

$$A = \frac{8\pi\, 0.2303\, n_f^3}{N_A n_a c\lambda^3} \int \varepsilon(\lambda)\lambda\, d\lambda \approx 2.88 \times 10^{-15} \frac{n^2}{\lambda^4}\, \varepsilon(\lambda_{\max})\, \Delta\lambda \tag{2.7}$$

where $\varepsilon(\lambda)$ is the wavelength dependent molar extinction coefficient, n_f and n_a are the refractive indices at the fluorescence, N_A is Avogadro's number and absorption

wavelengths, respectively, and $\lambda_{\max}$ and $\Delta\lambda$ are the maximum and the full width half maximum of the absorption peak, respectively. In the case of the CdTe particles in chloroform (spectra are shown in Figure 1.1(c)) – $n = 1.44$, $\lambda_{max} = 563$ nm (the first absorption peak), $\Delta\lambda = 30$ nm, $\varepsilon(\lambda_{max}) = 4.6 \times 10^5\ M^{-1}cm^{-1}$ [42, 43] – the values for the contents defined above come out as: $A = 8.18 \times 10^8\ s^{-1}$ or $(1.22\ ns)^{-1}$, $C = 3.03 \times 10^8$ and $2f_{1L} + 2f_{1U} + f_{0U} = A/C = 2.7$. The accurate estimation of the molar extinction coefficient is necessary for this calculation. Section 2.6 discusses this in greater detail and concludes that the molar extinction coefficients calculated by references [42, 43] are potentially higher than the actual value.

2.6 Determination of the Extinction Coefficient

The extinction coefficient is related to the absorption strength by the following simple equation (Beer Lambert law): $Abs = \epsilon lc$, where Abs is the absorbance, l is the length of the optical path and c is the concentration of absorbers. This makes is clear that an accurate estimation of the extinction coefficients depends on an accurate estimation of the concentration. This is commonly done by measuring the absorbance of a known volume of the sample and weighing the precipitated QDs from the sample to estimate the molar amount present. This method is plagued by interference from the molar mass of ligands attached to the surface and the other organic material that may also precipitate along with the QDs. This leads to an over-estimation of the concentration hence and under-estimation of the extinction coefficients. Another method uses inductively coupled plasma (ICP) measurements to estimate the cation/anion amounts and an empirical sizing curve can be used to determine the number of dots from this data. This method is more accurate than the gravimetric approach described earlier but heavily depends on accurate sizing curves. Reference [42] and [43] use this method and end up with values that differ by ∼30% due to differences in sizing curves.

CdTe extinction coefficients reported by Kamal *et al.*[44] are based on measuring the QD sizes by TEM and the total CdTe concentration by ICP-MS. Size dispersion broadens the absorption spectrum in the region of the lowest exciton, so the extinction coefficient of the lowest exciton depends on the monodispersity of the sample. As such, it is more useful to report the value at a shorter wavelength where quantum confinement effects are minimal. In this case, the fitting of the size-dependent 410 nm extinction coefficients give

$$\varepsilon_{410} = 1.06 \times 10^4\ D_{QD}^3, \tag{2.8}$$

where D_{QD} is the QD diameter in nm. Extinction coefficients at the lowest excitons are then be determined from the absorption spectra. From Figure 2.3 this gives $\varepsilon_{560} = 2.9 \times 10^5$ L mol^{-1}cm^{-1}.

The extinction coefficient of the $1S_e$-$1S_h$ exciton can also be calculated from the optical properties of bulk CdTe and the QD absorption spectrum. The idea is to use the bulk CdTe properties to calculate the extinction coefficient at a wavelength that is sufficiently far blue that quantum confinement effects are negligible, and then, as before, use that extinction coefficient and the measured QD absorption spectrum to obtain the

extinction coefficient at the $1S_e$-$1S_h$ exciton. Using this approach and CdTe QD sizing curves, de Mello Donega *et al.*[45] report the molar extinction coefficient of zincblende CdTe QDs at 3.1 eV (400 nm). The 400 nm extinction coefficient is given by

$$\varepsilon_{400} = 1520 \left(\frac{4V_{QD}}{V_{UC}} \right) = 1.17 \times 10^4 \, D_{QD}^3, \tag{2.9}$$

where V_{QD} and V_{UC} and the quantum dot and unit cell volumes, respectively and D_{QD} is the QD diameter in nm. When the 410 versus 400 nm absorptions are considered, this result is in reasonable agreement (about 24% larger) than the direct experimental value. In this case, Figure 2.3 gives $\varepsilon_{560} = 3.6 \times 10^5$ L mol^{-1}cm^{-1}. We have also used this approach to calculate the lowest exciton extinction coefficient based on bulk properties at higher energies. The reason for wanting to use higher energies is to be able to more confidently disregard quantum confinement effects. In the absence of quantum confinement effects, the extinction coefficient is given as

$$\varepsilon_\lambda = \frac{N_A 2\pi}{2303 \, n_m \lambda} V_{QD} |f_{LF}(\lambda)|^2 2 n_s k_s \tag{2.10}$$

where V_{QD} is the QD volume, N_A is Avogadro's number, n_s and k_s are the real and imaginary parts of the CdTe refractive index, n_m is the solvent refractive index and $f_{LF}(\lambda)$ is the local field factor, given by

$$|f_{LF}|^2 = \frac{9 n_m^4}{\left(n_s^2 - k_s^2 + 2n_m^2\right)^2 + 4 n_s^2 k_s^2} \tag{2.11}$$

for a spherical particle. We evaluate the extinction coefficient at 350 nm and use the spectrum in Figure 2.3 to then get the 560 nm extinction coefficient. Putting the CdTe values[46] for n_s and k_s and a solvent refractive index of 1.4, we get $|f_{LF}|^2 = 0.186$ at 350 nm. The QD diameter is taken to be 3.25 nm, and equation 10 gives an extinction coefficient $\varepsilon_{350} = 9.8 \times 10^5$ L mol^{-1} cm^{-1}. From the absorption spectrum, this corresponds to $\varepsilon_{560} = 3.35 \times 10^5$ L mol^{-1}cm^{-1}, about 17% larger than the directly measured result, which is reasonable agreement. We note that the exact calculated value of ε_{560} varies with the wavelength chosen for evaluation of the bulk extinction coefficient. Choosing wavelengths between 340 and 400 nm gives ε_{560} values between 3.05×10^5 and 5.1×10^5 L mol^{-1} cm^{-1}, which reflects the uncertainties associated with this approach. We choose 350 nm because this is far enough above the exciton energy to minimize quantum confinement effects, yet not so blue to be subject to absorption from impurities. In the analysis that follows, we will use the experimental value of $\varepsilon_{560} = 2.9 \times 10^5$ L mol^{-1}cm^{-1}, with the caveat that the correct value may be as much as 25% larger.

2.7 Effects of Charged Ligands on Fine Structure

In this section we examine the role of internal electric fields produced by charged ligands on the fine structure states of CdTe QDs. The magnitude of these fields depends

on the nature (charged or uncharged) of the ligands, the nature of the surface crystal facets and the polarity of the surrounding solvent. Below, we will examine all these factors but will focus on the role of ligand charge in QDs having surface facets giving the largest effects, presumably corresponding to the highest ligand densities. Reference 3 presents calculations showing that charged dopant atoms can have very significant effects on the splittings and mixing of the fine structure states, leading us to expect that the presence of charged ligands on the particle surfaces may also have large effects. The quasi-spherical CdTe particles used here can be ligated with either charged or uncharged ligands on the surface crystal facets. The ligand density and hence the surface charge density will depend on the nature of the crystal facets, and this will control the magnitude and the symmetry of the internal electric fields. Exchanging charged with uncharged ligands is expected to have large effects on the internal electric fields, and therefore measurable effects on the fine structure states. The three complementary spectroscopic measurements discussed above are used to study the exciton fine structure. The model in reference 1 allows calculation of the magnitudes of the $\pm 1^L / \pm 1^U$ mixing and the $\pm 2 / \pm 1^L$ and $\pm 1^U / 0^U$ splittings in terms of two parameters: the light/heavy hole splitting and the electron/hole exchange interaction. This two-parameter model cannot describe the more general case in which the perturbation is an internal electric field having several Y_{lm} components. Below we show that the extent to which this simple model breaks down in the presence of charged crystal facets can be assessed in terms of the spectroscopic measurements.

2.7.1 Ligand-dependent Spectroscopy

The absorption and PL spectra of CdTe QDs synthesized with OA/ODPA (details in Appendix A), ligated with ODPA and following ligand exchange to octanethiol are compared in Figure 2.3. IR spectroscopy shows that the ligand exchange procedure results in near complete removal of the surface-bound ODPA (Figure 2.4).

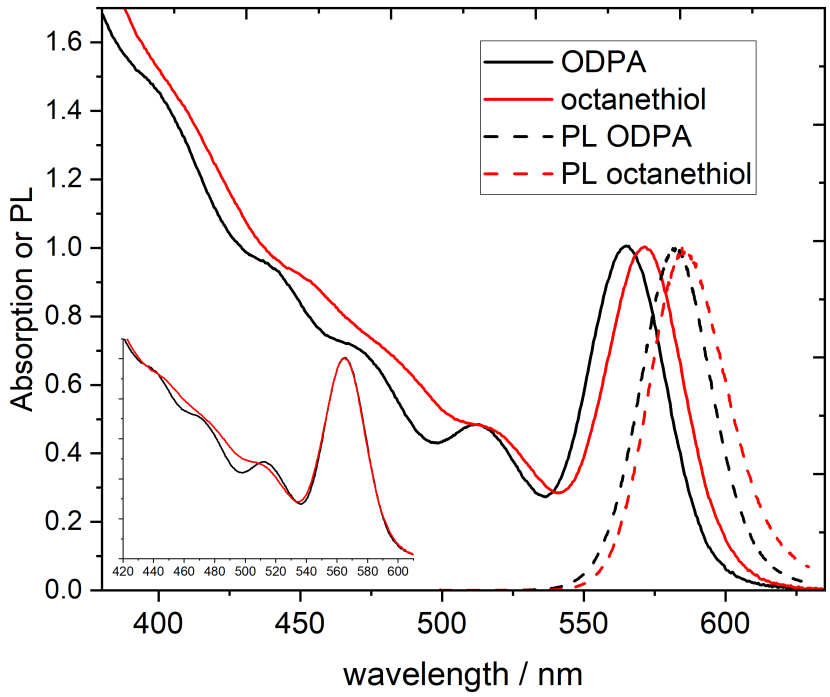


FIGURE 2.3: Absorption and PL spectra of 3.3 nm diameter CdTe particles having ODPA ligands (black) or octanethiol ligands (red). The PL spectra have widths of 110 meV (ODPA) and 118 meV(octanethiol), and Stokes shifts of 64 meV (ODPA) and 51 meV (octanethiol). The inset shows ODPA and octanethiol absorption spectra with the octanethiol spectrum shifted 6.5 nm to the blue, so that its absorption maximum matches that of the ODPA spectrum

The ODPA-ligated absorption spectrum shows the lowest energy exciton with a peak absorbance at 560 nm and a Stokes-shifted (17.1 nm, 64 meV) PL maximum. The PL is quite intense, having a QY of about 60%. Sizing curves put the particle diameters at 3.2–3.3 nm.[42, 44, 45] The ODPA ligands can be exchanged for octanethiol, resulting in an approximately 6.5 nm red shift in the absorption spectrum, a smaller 3.0 nm shift in the PL spectrum, and only a slight (<10%) loss in PLQY. Reverse ligand exchange restores the absorption and PL spectral maxima to very close to their original values (Figure 2.8). ODPA to oleate ligand exchange has little to no effect on the spectra (Figure 2.8), nor on the other measured parameters discussed below (Figures 2.8 and 2.9).

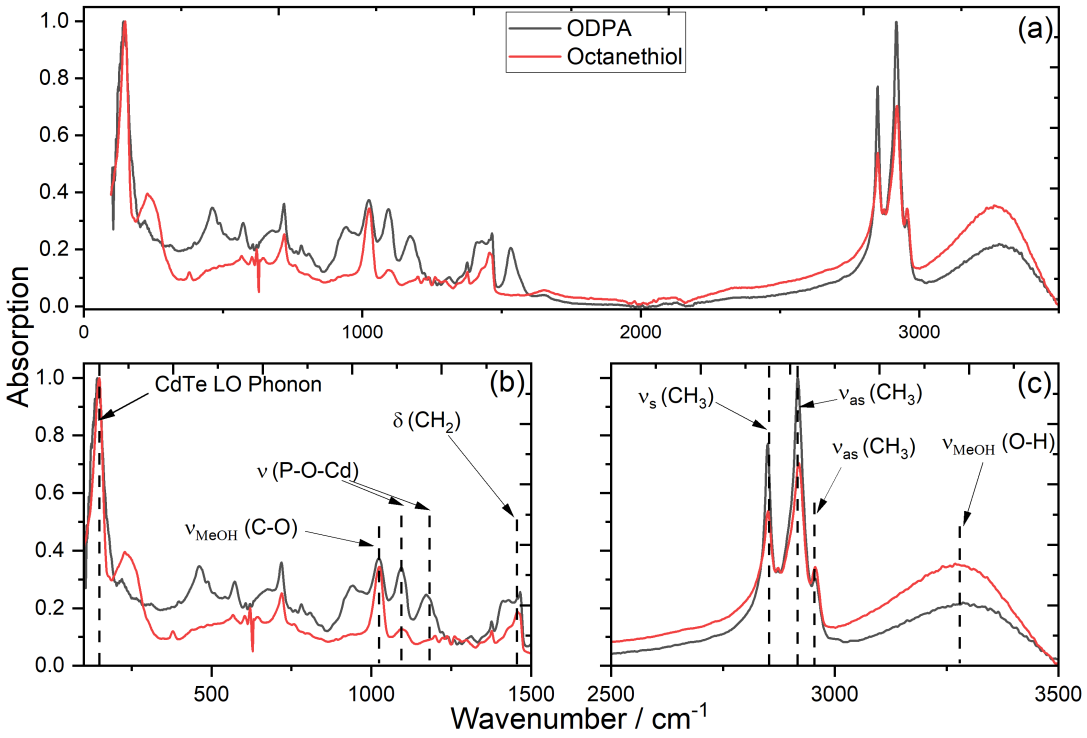


FIGURE 2.4: (a) FT-IR spectra of washed ODPA ligated CdTe QDs (black) and same QDs with octanethiol ligands (red). Panel (b) shows the low frequency features of the spectra, most notably the LO phonon mode at 145 cm^{-1} which is used to normalize the two curves since the intensity of the LO phonon line is proportional to the total volume of the CdTe nanocrystals. The QD surface bound ODPA can be characterized by the symmetric and asymmetric P-O-Cd stretch modes ($\nu_{\text{P-O-Cd}}$) at 1093 cm^{-1} and 1172 cm^{-1}.[47, 48] Those features are almost completely absent in the ligand exchanged sample (Oct-SH ligated QDs) confirming the near complete removal of ODPA upon ligand exchange. Panel (c) shows the high frequency components showing the stretch modes corresponding to the CH_2 at 2848 cm^{-1} and 2918 cm^{-1} and CH_3 at 2956 cm^{-1} present in both ODPA and octanethiol ligated QDs. Both high frequency and low frequency components have features corresponding to methanol (broad feature at $\sim$3250 cm^{-1} and a sharp feature at 1024 cm^{-1}) which was used in the process of purifying the QDs

The shift in the absorption spectrum can be understood in terms of the extent to which the hole wavefunctions are delocalized.[49] Alkyl thiol ligands are good hole acceptors and are known to quench CdSe excitons. However, the CdTe valence band is at a less positive potential, and alkyl thiol ligands only slightly perturb the hole, lowering the valence band quantum confinement energy. The result is a modest shift in the exciton energy without charge transfer quenching. The spectral width of the lowest exciton transition is unchanged by ligand exchange, indicating no measurable change in the particle size distribution. The spectra also show that ODPA to octanethiol ligand exchange decreases the Stokes shift from 64 to 51 meV. It is also of interest to note that

the intensity of the continuum absorption above ∼540 nm increases upon ODPA to octanethiol ligand exchange,[24] indicating that continuum absorption involves nanoparticle surface states. The details of how the continuum absorption varies with surface chemistry and stoichiometry is discussed in Chapter 3.

The PLE anisotropy spectra of ODPA- and octanethiol-ligated CdTe QDs are shown in Figure 2.5. As in the absorption spectra, reverse ligand exchange restores the spectrum to very close to its original ODPA spectrum (Figure 2.8).

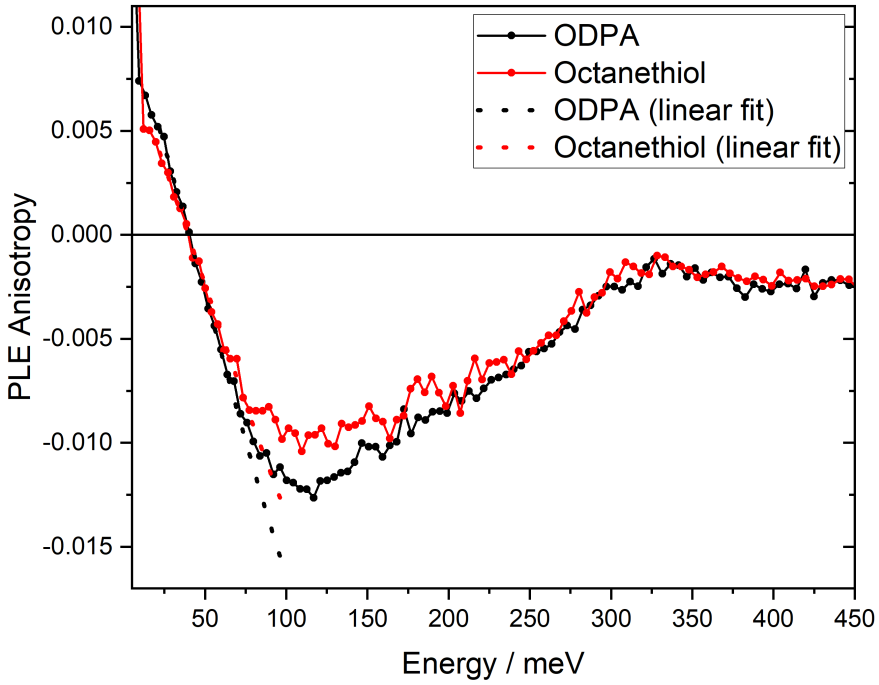


FIGURE 2.5: PLE anisotropy spectra of CdTe QDs ligated with ODPA (black curve), octane thiol (red curve). The energy zero corresponds to excitation and detection at the same wavelength, which is the PL maximum. Also shown are linear fits near r = 0 with slopes of 0.277 eV-1 and 0.222 eV-1 for ODPA and octanethiol, respectively.

As mentioned above, the higher energy (greater than about 100 meV) region of the absorption spectrum has significant contribution from continuum transitions. These transitions involve surface states and are therefore likely to be unpolarized. All but the lowest energies of the anisotropy spectra in Figure 2.5 are therefore complicated by the presence of these transitions. Because of this complication, we will focus on the low energy region, specifically, the slope of the spectrum at $r = 0$, corresponding to equal absorption contributions of the $\pm 1^U$ and 0^U states. This region of the spectrum can be qualitatively understood in terms of Figure 2.3. Although transitions to the $\pm 1^L$ states have less oscillator strength than transitions to the higher energy $\pm 1^U$ and 0^U states, the Boltzmann factor strongly favors the lower energy state and much of the luminescence

is from this (x, y)-polarized state. Furthermore, because of the significant splitting between the $\pm 1^U$ and 0^U states, the Boltzmann factor strongly favors the lower energy state. The conclusion is that almost all the luminescence is from (x, y)-polarized states. The PLE anisotropy spectrum can be qualitatively understood in terms of which states are preferentially excited as a function of the excitation wavelength. When the excitation is between the $\pm 1^L$ and the centroid of the $\pm 1^U$ and 0^U states, most of the excitation is to the (x, y)-polarized $\pm 1^L$ and $\pm 1^U$ states. As a result, at the lowest PLE energies, a positive anisotropy is observed. At excitation energies above the $\pm 1^U$ and 0^U centroid excitation is primarily to the higher energy, z-polarized 0^U state and a negative anisotropy is observed. The anisotropy zero occurs when there are equal absorption contributions from the $\pm 1^U$ and 0^U states. Since the upper states have most of the oscillator strength, the energetic centroid of the $\pm 1^U$ and 0^U states is close to the $1S_h$-$1S_e$ absorption band maximum. We note that if the splitting between the $\pm 1^U$ and 0^U states were very small compared to the overall $1S_e$-$1S_h$ width (on the order of 100 meV), then their absorption spectra would be completely overlapping, and little or no anisotropy would be observed. The fact that significant positive and negative anisotropies are observed shows that there is a significant splitting between the $\pm 1^U$ and 0^U states. The comparable spectral widths along with the larger slope of the PLE anisotropy obtained with ODPA ligands indicates that the $\pm 1^U/0^U$ splitting is larger in this case, compared to QDs with octanethiol ligands. We note that the total spectral width of the lowest exciton is essentially unchanged in Figure 2.3. This precludes large changes in the fine structure splittings. However, the PLE anisotropy measurements are vastly more sensitive to the $\pm 1^U/0^U$ splitting than is the total spectral width. A change of the $\pm 1^U/0^U$ splitting of a few meV would be undetectable in the width of this transition in the absorption or unpolarized PLE spectrum. However, modeling results (discussed below) show that changes of a few meV result in easily detectable changes in the PLE anisotropy spectrum.

The accuracy of the PLE anisotropy spectrum depends on sufficiently arresting the effects of rotational diffusion, which depends on the viscosity of solvent medium and the volume of the particles among other factors. The PLE anisotropy spectrum corresponding to octanethiol ligated particles in 1:1 (v/v) toluene/ODE solution and 1:3 (v/v) toluene/ODE (shown in Figure 2.6) demonstrate that there is no detectable difference in the PLE anisotropy upon increasing the viscosity of the solvent. This indicates that 1:1 (v/v) toluene/ODE has an adequately high viscosity that the PLE anisotropy measurements are free of rotational diffusion artifacts.

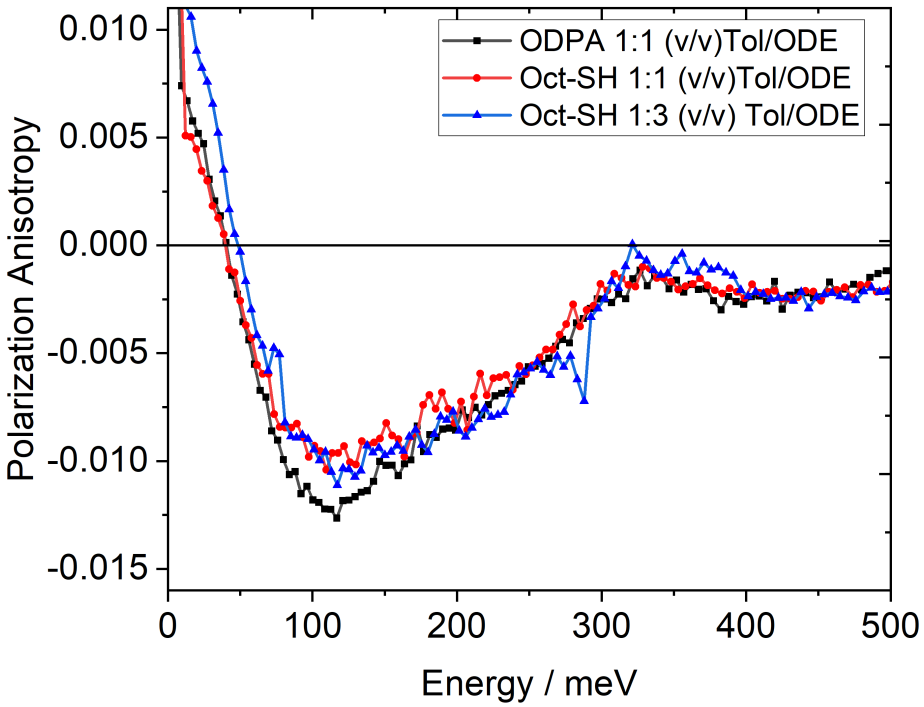


FIGURE 2.6: Shows the PLE anisotropy spectra CdTe QDs ligated with octanethiol in 1:1 (v/v) toluene/ODE (red curve) and 1:3 (v/v) toluene/ODE (blue curve) showing near identical features. The PLE anisotropy spectrum of the ODPA ligated particles in 1:1 (v/v) toluene/ODE is also shown for reference (black curve).

2.7.2 Ligand-dependent Radiative Dynamics

In QDs having near unity PLQY, the radiative lifetime is easily determined from the PL decay kinetics. A PLQY that is less than unity indicates that some of the particles undergo nonradiative decay, often giving rise to observable decay components that are shorter than the intrinsic radiative lifetime. The time-resolved PL decays in Figure 2.3 show several decay components. The short components are assigned to particles that undergo irreversible carrier trapping, followed by nonradiative recombination. A relatively small fraction of the CdTe QDs also undergo reversible carrier trapping, giving rise to PL decay components that are longer than the radiative lifetime.[25] These longer components have been reported to correspond to less than a few percent of the total decay curve amplitude,[25] and that is consistent with what we observe in the present case. Thus, the longest large-amplitude PL decay component can be assigned to the radiative lifetime.

The PL decays are fit to a biexponential with a small long-lived component,

$$I(t) = A_1 \exp\left(-\frac{t}{\tau_1}\right) + A_2 \exp\left(-\frac{t}{\tau_2}\right) + A_3. \tag{2.12}$$

The fitting parameters are given in Table 2.1.

TABLE 2.1: Fitting parameters for the PL decays.

	A_1	τ_1	A_2	τ_2	A_3
ODPA	0.12	6.7	0.87	23.0	0.01
octanethiol	0.15	5.5	0.82	27.3	0.03
ODPA (reversed)	0.17	4.3	0.81	23.9	0.02

Ligand exchange from ODPA to octanethiol results in a small increase in the amplitude of the fast (nonradiative decay) component, which further increases upon reverse ligand exchange. These sample manipulations create surface recombination centers on a small fraction of the QDs. Importantly, the radiative lifetime increases from 23.0 to 27.3 ns upon ligand exchange and reverse ligand exchange decreases the radiative lifetime to 23.9 ns, almost back to the original value. We find this that this ≈15% difference in radiative lifetimes between ODPA and octanethiol ligated particle is very reproducible from one batch of particles to another. The overall total oscillator strength of the $1S_h$-$1S_e$ exciton is intrinsic to the QD size and material; it is not expected to significantly change with ligation. As such, the longer radiative lifetime with (neutral) octanethiol ligands indicates that a smaller fraction of the oscillator strength is in the $\pm 1^L$ states than with the (charged) ODPA ligands.

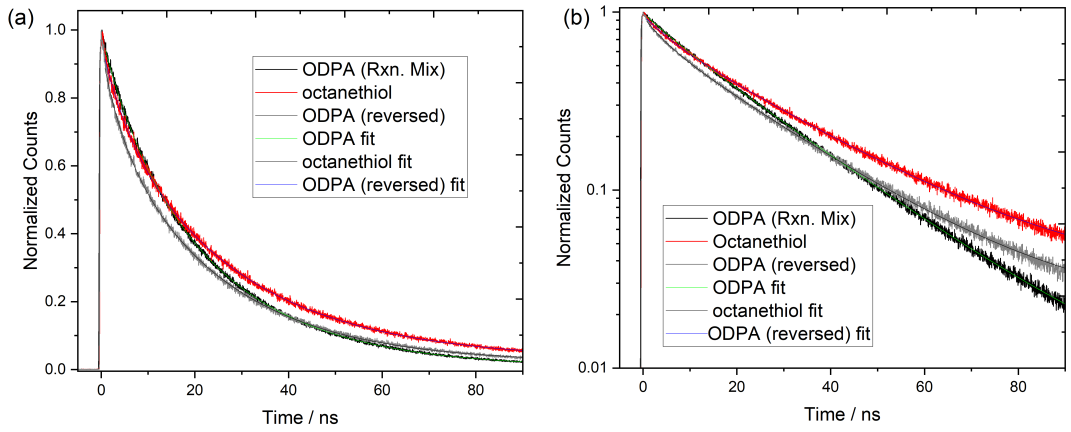


FIGURE 2.7: PL decays shown on linear (A) and log (B) scales. Also shown are fits corresponding to radiative lifetimes of 23.0, 27.3 and 23.9 ns for ODPA, octanethiol and ODPA (reversed) ligands, respectively.

The results presented in Figures 2.3 and 2.7 can be summarized in terms of three crucial observations associated with ODPA to octanethiol ligand exchange. Ligand exchange results in a decrease in the slope of the PLE anisotropy spectrum at low energies, a decrease in the magnitude of the Stokes shift, and an increase in the radiative

lifetime. All three of these observations are consistent with a decrease in the fine structure splittings and the extent to which oscillator strength gets mixed into the $\pm 1^L$ states.

We note that these results were obtained with particles synthesized in OA/ODPA. The magnitude of the ligand-dependent spectroscopic changes depends on the details of the QD synthesis. Specifically, particles synthesized in stearic acid/ODPA and at higher nucleation temperatures show smaller ligand exchange effects. We think it is likely that the temperature and the ligands present in the synthesis reaction mixture affect the nature of the surface crystal facets, and this affects the final ligand density. These effects will be briefly discussed towards the end of this chapter. We now address the question whether the relative magnitudes of these changes can be quantitatively understood in terms of the standard model presented in reference [17].

2.7.3 Modeling the Ligand-dependent Spectroscopy

The model in reference [17] gives the relative oscillator strengths and energetic splittings of the eight fine structure states in terms of two parameters: the electron-hole exchange energy, η, and the energetic splitting between the heavy and light holes, Δ. The former is characteristic of the QD size, and the latter is a measure of the extent to which the exciton potential is nonspherical. The model predicts that as the exciton potential deviates from being spherical, the $\pm 1^U/0^U$ and $\pm 2/\pm 1_L$ splittings become larger and the lower energy $\pm 1^L$ states gain oscillator strength. Increasing the $\pm 1^U/0^U$ splitting results in larger magnitudes of the PLE anisotropies and hence a larger magnitude of the PLE anisotropy slope, $\left.\frac{dr}{dE}\right|_{r=0}$, as seen in Figure 2.5. It also results in more luminescence coming from the $\pm 1^L$ states, which increases the Stokes shift as seen in Figure 2.3 and shortens radiative lifetimes as seen in Figure 2.7 and Table 2.1. We suggest that the charged ODPA ligands perturb the shape of the exciton more than the neutral octanethiol ligands. As such, this model is qualitatively consistent with the experimental results.

A quantitative analysis of PLE anisotropy, Stokes shift and lifetime results is somewhat complicated. The approach taken below is to attempt to find η and Δ values that allow calculation of all the results in Figures 2.3 – 2.7. Specifically, we want to obtain η and Δ values that fit $\left.\frac{dr}{dE}\right|_{r=0}$ and the radiative lifetimes for both ODPA and octanethiol ligands as well as the ligand-dependent difference in Stokes shifts. Specifying η and Δ values allows calculation of the energies and relative oscillator strengths of each fine structure state. The extent to which a single set of η and Δ parameters can accurately fit both the lifetime and polarization results will allow us to comment on the validity of this simple two-parameter model. The energies and oscillator strengths from the model are not sufficient to calculate the lifetimes and anisotropy spectra. Calculation of the PLE anisotropies also requires a measure of the homogeneous linewidths and calculation of the radiative lifetime also requires knowing the total oscillator strength. Determination of the total oscillator strength and the homogeneous width and how these

values facilitate calculation of the measured quantities through the standard model is discussed next.

Equation (1.15) can be rewritten in terms of the following averaged relative oscillator strengths:

$$P_{\pm 1_L} = \frac{2\sqrt{4\eta^2 - \eta\Delta + \frac{\Delta^2}{4}} - 4\eta + \frac{\Delta}{2}}{2\sqrt{4\eta^2 - \eta\Delta + \frac{\Delta^2}{4}}} \tag{2.13}$$

$$P_{\pm 1_U} = \frac{2\sqrt{4\eta^2 - \eta\Delta + \frac{\Delta^2}{4}} + 4\eta - \frac{\Delta}{2}}{2\sqrt{4\eta^2 - \eta\Delta + \frac{\Delta^2}{4}}} \tag{2.14}$$

$$P_{0_U} = P_{\pm 1_U} + P_{\pm 1_L} \tag{2.15}$$

$$P_{0_L} = 0, \qquad P_{\pm 2} = 0 \tag{2.16}$$

Using equations (1.14),(2.13) – (2.16), the energetics and relative oscillator strengths of the states depicted in Figure 1.3 can be assessed. The magnitude of the wavelength-dependent PLE anisotropy depends on the extent to which the x, y-polarized $\pm 1^U$ and the z-polarized 0^U states can be selectively excited and therefore depends on the ratio of the energetic separation to the homogeneous width of each state. The overall width of the PL spectrum depends on both homogeneous and inhomogeneous contributions. The inhomogeneous linewidth can be obtained from measurement of how the center of the $1S_e$-$1S_h$ transition in the (unpolarized) PLE spectrum varies with detection wavelength. An analysis of this result and the measured total PL linewidth allows calculation of the homogeneous linewidth, see the Section 2.4. The analysis indicates that if the homogeneous and inhomogeneous distributions are taken to be Gaussians, their widths are roughly the same, with a full-width at half-maximum of about 77 meV.

The value of η is expected to depend only on the size of the QD and therefore can be taken to be independent of the type of ligands. As such, changes following ligand exchange should only reflect differences in Δ. The PLE anisotropy slopes can be fit with a wide range of η values, with appropriately chosen Δ values. We therefore next determine which, if any, of these sets of η and Δ values also give the correct radiative lifetimes.

Equations (1.14), (2.13) – (2.16) give the energetics (and therefore Boltzmann populations) and relative oscillator strengths of all eight fine structure states. The functional dependencies of equations (1.14),(2.13) – (2.16) on η and Δ are notable. For a spherical particle ($\Delta = 0$), the energetic difference of the $J = 2$ and $J = 1$ states is 4η, and the $J = 2$ states are dark. If $\Delta \approx 0$ and $4\eta \gg kT$, then the upper states ($\pm 1^U$ and 0^U) have little Boltzmann population and the model predicts that the radiative lifetime is quite long. However, as the value of Δ increases (the Hamiltonian becomes oblate) the $\pm 1^L$ states acquire significant oscillator strength and the radiative lifetime decreases. However, the $\pm 2/\pm 1_L$ splitting also increases, and as a result, large Δ values result in a relatively small Boltzmann populations in the $\pm 1^L$ states, which limits

the extent to which the radiative lifetime decreases. Although these qualitative considerations are quite simple, quantitative calculation of radiative lifetime also requires knowing the total oscillator strength, and obtaining accurate values can be problematic. The oscillator strength can be obtained from the integrated $1S_e$-$1S_h$ exciton extinction coefficients, which can be determined in two different ways: by direct experimental measurement on QDs and by calculation from the optical properties of bulk CdTe. Having an accurate value of the total oscillator strength is crucial to calculating the radiative lifetime, and the details of these two methods are considered in the Section 2.6. From these considerations, we conclude that the best estimate of the experimental value is $\varepsilon_{560} \approx 2.9 \times 10^5$ L mol^{-1}cm^{-1}, with the caveat that the value may be as much as 25% larger. Evaluation of equation (2.7) using the wavelengths and spectral width in Figure 2.3 gives a two-level system radiative lifetime of 2.1 ns. The integrated extinction coefficient and radiative rate constant may be expressed in terms of the oscillator strength,[37] f

$$A = C'f \quad \text{where} \quad C' = \frac{2\pi ne^2}{\varepsilon_0 mc\lambda^2} \tag{2.17}$$

and

$$f = \frac{0.9212\, mnc^2\varepsilon_0}{N_A e^2} \int \frac{\varepsilon(\lambda)}{\lambda^2}\, d\lambda \approx 6.05 \times 10^{-11}\, \lambda^2\, \varepsilon(\lambda_{\max})\, \Delta\lambda \tag{2.18}$$

where m and e are the mass and charge of the electron, n is the refractive index of the surrounding solvent and ε_0 is the permittivity of free space. Using the above extinction coefficient, an absorbance maximum at $\lambda = 560$ nm and a spectral width $\Delta\lambda = 30$ nm, a total oscillator strength of $f = 1.6$ for the $1S_e$-$1S_h$ transition is calculated. This oscillator strength is partitioned between the fine structure states according to equations (2.13) – (2.16), as discussed below. We note that this value makes sense in terms of the total oscillator strength reported for red-emitting InP/ZnSe/ZnS QDs.[23] The InP/ZnSe/ZnS QDs have comparably core sizes, but the exciton has significant delocalization into the ZnSe shell. As a result, these CdTe QDs have somewhat (≈40%) smaller total oscillator strengths.

The absolute oscillator strengths in each of the fine structure states are related to the relative oscillator strengths by an experimentally determined numerical factor, which is determined above from the integrated exciton extinction coefficient. We will denote this factor as N_{QD}, specifically, $f_{1L} = N_{\mathrm{QD}} P_{\pm 1_L}$, $f_{1U} = N_{\mathrm{QD}} P_{\pm 1_U}$ and $f_{0U} = N_{\mathrm{QD}} P_{0_U}$. With the measured total oscillator strength of these QDs (= 1.6), application to equations (2.13) – (2.16) and equation (2.18) gives $N_{\mathrm{QD}} = 1.6/6 = 0.267$. We note that in the limiting case of a spherical particle, $\Delta = 0$, equations (1.14),(2.13) – (2.16) simplify and give $E_{\pm 2} = E_{\pm 1_L} = E_{0_L} = -3\eta/2$, $P_{\pm 1_L} = 0$ and $E_{\pm 1_U} = E_{0_U} = 5\eta/2$, $2f_{1U} + f_{0U} = 1.6$. In this case, all the oscillator strength is in the degenerate upper states while the lower states are degenerate and dark.

We find that the PLE anisotropy slopes can be fit with a range of η and corresponding Δ values. If, in analogy to comparably sized InP/ZnSe/ZnS QDs,[23] η is taken to be $\eta = 13$ meV, then the PLE anisotropy slopes can be fit with $\Delta = 34.5$ meV (ODPA) or 31.8 meV (octanethiol). Using these parameters, the calculated ODPA and octanethiol

lifetimes are very close to the same and far too long, 76 and 77 ns for ODPA and octanethiol, respectively. The measured lifetimes in Table 2.1 are about a factor of 3.0 less than the calculated value. We conclude that these discrepancies are too large to be due to inaccuracies in estimates in the extinction coefficient and hence total oscillator strength. If the largest calculated exciton extinction coefficient is assumed, then the calculated radiative lifetime is shorter, about 43 ns, but still almost a factor of two larger than the experimental values. These very long lifetimes are calculated because with $\eta = 13$ meV and these Δ values, there is little mixing of the $\pm 1^L$ and $\pm 1^U$ states and most of the PL is calculated as coming from the upper states. The Boltzmann population in these states is small and the calculated radiative lifetime is very long and not very sensitive to the Δ value.

Alternatively, the measured PLE anisotropy slopes can be fit if η is taken to be very small. If we take $\eta = 5$ meV and $\Delta = 28.7$ meV (ODPA) or 26.4 meV (octanethiol), the correct anisotropy slopes are again obtained, and in this case, the calculated lifetimes are not vastly different than what is observed, 28.3 (ODPA), 28.4 (octanethiol). However, with such a small assumed value for η, the $\pm 1^L$ and $\pm 1^U$ states are very strongly coupled and the calculated lifetimes and Stokes shifts are almost totally insensitive to the value of Δ. This is contrary to the experimental results in Figure 2.3 and Table 2.1. We conclude that equations (1.14),(2.13) – (2.16) do not facilitate quantitative understanding of the fine structure. The experimental results suggest that there is more oscillator strength in the lower $\pm 1^L$ states than what is calculated by the standard model and/or the internal electric fields break the x, y symmetry and thereby lower the PLE anisotropy.

The fundamental problems with trying to quantitatively understand these results in terms of the standard model can be summarized as follows. The PLE anisotropy spectra show small slopes near the center of the $\pm 1^U/0^U$ states. This requires a very small splitting between the upper states. If this is the case, and if η is taken to be a reasonable value of about 13 meV, then the mixing of the $\pm 1^L$ state with $\pm 1^U$ state is also small and the lower states are close to being dark. As a result, most of the PL is calculated to be from the upper states, and due to the small Boltzmann factor, the calculated radiative lifetime is far too long and insensitive to Δ. Alternatively, if η is taken to be very small, then the Boltzmann population in the upper states is much larger, and the total radiative lifetime is calculated to be about right. But in this case, the calculated lifetime and Stokes shift are almost completely insensitive to Δ, making it impossible to explain the observed ligand dependence. Furthermore, η should scale like the inverse of the particle radius, so based on InP/ZnSe/ZnS QDs,[23] such a small value of η does not seem to be physically reasonable. The conclusion is that the CdTe particles must have smaller $\pm 1^U/0^U$ splittings and/or breaking of the x, y degeneracy in the $\pm 1^U$ states, as well as more $\pm 1_L/\pm 1_U$ mixing than predicted by the standard model. The perturbations that break the x-y degeneracy also further mix the upper and lower ± 1 states.

We noted above that the magnitude of the Stokes shift decreases upon ODPA to

octanethiol ligand exchange, see Figure 2.3. This is assigned to a decrease in the fraction of the PL that originates from the lower energy $\pm 1^L$ states, shifting the overall PL spectrum to the blue. The sensitivity of the Stokes shift to the change in the relative $\pm 1^L$ and $\pm 1^U$ oscillator strengths suggests that a significant fraction of the PL originates from the upper states and that fraction increases upon ligand exchange. Although the Stokes shift results indicate that a significant fraction of the PL originates from the upper states, without an accurate model of how the energetics relate to the relative oscillator strengths, the fraction of the PL coming from each of the states cannot be accurately assessed.

2.7.4 Lowering of Symmetry & Group Theory Considerations

A more recent paper by Sercel *et al.* [40] shows that surface electric fields alter the splittings and mix the polarizations of the upper states in ways that depend on the specific symmetry of the perturbation. This can be understood by considering the transformation properties of the excitonic wavefunctions and the different perturbations that mix them.

Consider the transformation properties of the $j = 3/2$ hole and the $j = 1/2$ electron. The hole transforms as Γ_8 (note that the bases for Γ_8 are $|3/2, 3/2\rangle$, $|3/2, 1/2\rangle$, $|3/2, -1/2\rangle$ and $|3/2, -3/2\rangle$) and the electron as Γ_6 (note that the bases for Γ_6 are $|1/2, 1/2\rangle$ and $|1/2, -1/2\rangle$). The exciton transforms as the direct product, $\Gamma_8 \times \Gamma_6 = \Gamma_3(E) + \Gamma_4(T_1) + \Gamma_5(T_2)$. Of these 8 states, only T_2 is allowed (corresponding to $\pm 1^U$ and 0^U) while T_1 (corresponding to $\pm 1^L$ and 0^L) and E (corresponding to ± 2) are dark. We also note that an oblate/prolate perturbation transforms as $\Gamma_3(E)$. It mixes T_1 with T_2 and therefore allows the T_1 states (there is no distinction between (x, y, z) in T_d). It does not allow the E ($m_j = \pm 2$) states, that is, $\Gamma_3 \times \Gamma_3$ does not contain Γ_5. This is consistent with the Efros 1996 paper.[17]

We can consider which Y_l^m perturbations allow which of the forbidden transitions. The spherical harmonics (Y_2^m) transform as $T_2 + E$. Specifically: $Y_2^0 \rightarrow E$; $Y_2^{\pm 1} \rightarrow T_2$; $Y_2^{\pm 2} \rightarrow E + T_2$. To be allowed, the direct product of the state and the perturbation must transform as T_2 to be allowed. Taking the direct products, we get that a Y_2^2 perturbation allows T_2, but not E. All the Y_l^m perturbations allow all the fine structure states.

This is consistent with the 2017 Sercel paper,[40] which states that when inversion and rotational symmetry is lost, all transitions become symmetry allowed. In the case of excitation into the $\pm 1^U$ and 0^U states, breaking the x, y symmetry of the absorbing $\pm 1^U$ and the emitting $\pm 1^L$ states along with changing the splittings can have the effect of diminishing the PLE anisotropies. The additional perturbations also mix the upper and lower states, lowering the radiative lifetime. We suggest that inclusion of these lower symmetry perturbations is necessary to quantitatively understand the effects of ligand-induced internal electric fields on the fine structure. However, the results presented here are insufficient to allow detailed modeling of these perturbations.

2.7.5 Reversal to Charged Ligation

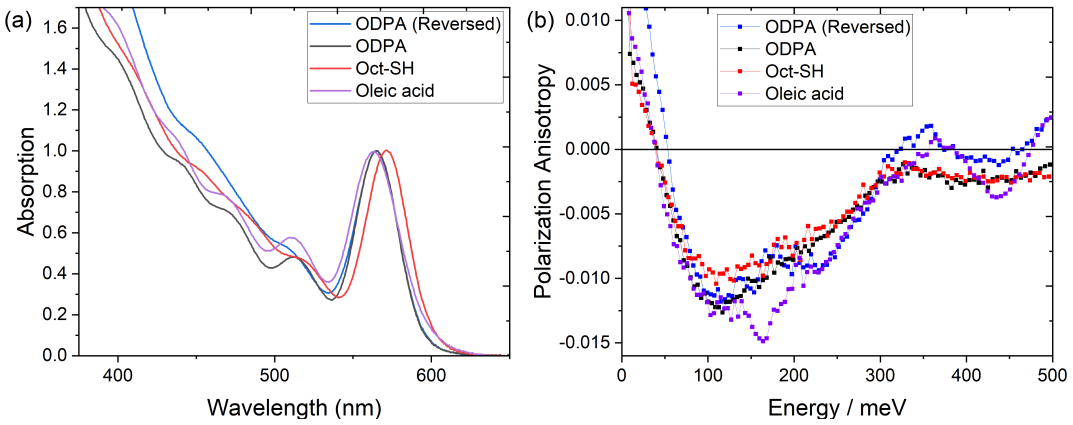


FIGURE 2.8: (a) The absorption spectra and (b) PLE anisotropy spectra of CdTe QDs ligated with ODPA in the original reaction mixture (black curves), same particles ligand exchanged to octanethiol (red curves) and after reversal to ODPA ligation (blue curves) discussed in the main text. It also shows the absorption and PLE anisotropy spectra corresponding to an essentially identical set of particles (a different batch of the same ODPA/OA synthesis used for the data in the main text) ligand exchanged to oleic acid ligation (violet curves).

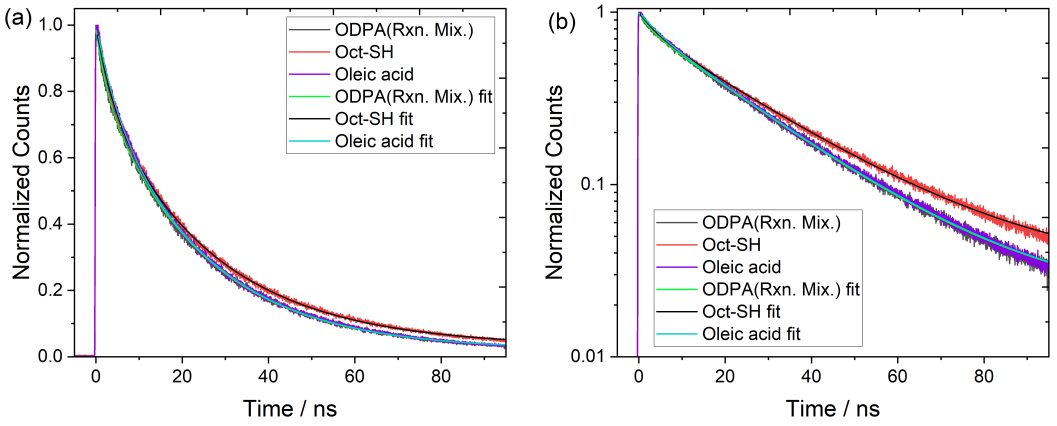


FIGURE 2.9: PL decays shown on linear (a) and log (b) scales. Also shown are fits corresponding to radiative lifetimes of 23.7, 26.3 and 23.9 ns for ODPA, octanethiol and oleic acid ligands, respectively.

The absorption and PLE anisotropy spectra in Figure 2.8 indicate that the reversal to ODPA ligation and a ligand exchange to oleate ligands restores the absorption spectrum and PLE anisotropy close to those of ODPA ligated QDs immediately after synthesis. The particles that have been reverse exchanged back to ODPA ligation have a slightly larger contribution from the continuum absorption to the blue of the lowest exciton. The reverse ligand exchanged sample showed somewhat larger scattering, resulting in the slope of the anisotropy curve around $r = 0$ being unreliable. The

oleic acid ligated particles show signs of a very small amount of etching, which results in a slight spectral broadening. However, the PLE anisotropy spectrum closely follows that of the ODPA ligated particles from the reaction mixture. The slope of the anisotropy curve of this sample near $r = 0$ is 0.31 eV^{-1} compared to 0.277 eV^{-1} in the ODPA ligated shown in Figure 2.5. The PL decay data in Figure 2.9 shows an increase in radiative lifetime from 23.7 ns to 26.3 upon ligand exchange to octanethiol. Ligand exchange of the same sample to oleic acid leaves the radiative lifetime essentially unchanged, 23.9 ns. The reversal to charged ligation leaving the spectroscopy and dynamics unaffected implies that the ligand exchange process does not affect the morphology significantly and that this phenomenon is purely electrostatic; i.e. it is not dependent on the organic nature of the ligand rather solely on the electrostatic charge on the binding entity in the ligand (oxygen/ sulfur in this case).

2.8 Conclusions

The central conclusion of these studies is that the nature of the ligands on the surface of CdTe QDs produce significant changes in the angular momentum fine structure. We suggest that this is due to large internal electric fields associated with charged ligands. The presence of the internal electric fields causes several changes in the QD spectroscopy and dynamics. Charged ligands result in more anisotropy in the polarized PLE spectrum, larger Stokes shift in the PL spectrum and a shorter radiative lifetime. These effects can be qualitatively described in terms of the standard model described in reference [17]. However, the magnitudes of the observed effects suggest that CdTe QDs exhibit smaller fine structure splittings and/or larger mixings than this model predicts. We suggest that this is due to the perturbations having lower symmetry than is assumed by the model in reference [17].

3 Surface Stoichiometry and Continuum

3.1 Abstract

This Chapter discusses the investigation of surface stoichiometry dependence of the absorption spectra in 3.2 nm CdTe quantum dots (QDs) using room-temperature absorption spectroscopy, more specifically we focus on the broad bulk-like contribution commonly referred to as continuum. This work was submitted to The Journal of Physical Chemistry C for review [50]. Systematic modification of the surface from Cd-rich to Te-rich conditions results in a pronounced increase in the absorption intensity, particularly in the region between the $1S_e$–$1S_h$ and $1S_e$–$2S_h$ transitions. In contrast, the absorption in the bulk limit remains comparatively insensitive to surface stoichiometry. We assign the continuum absorption to two distinct types of transitions: (i) low-energy transitions that involve transferring an electron from a surface chalcogenide dangling-bond to a quantum-confined conduction band state, and (ii) high-energy bulk-like transitions that scale with particle volume. We also find that the same considerations apply to continuum transitions involving adsorbed alkylthiols. We further apply this model to interpret the spectroscopy data of metal and chalcogenide rich ZnSe and CdSe quantum dots reported in literature. This analysis provides a consistent interpretation of continuum absorption in semiconductor quantum dots and highlights the role of surface stoichiometry in determining optical spectra.

3.2 Introduction

The optical properties of semiconductor quantum dots (QDs) are governed by quantum confinement and the resulting discrete electronic structure. In II–VI and III–V QDs, the electron and hole envelope functions as well as the angular momentum fine structure play central roles in determining both the absorption spectra and radiative dynamics. For samples with narrow size distributions, the absorption spectrum consists of well-resolved features corresponding to transitions between specific quantum-confined electron–hole states.

Superimposed on these discrete transitions is a featureless, monotonically increasing background commonly referred to as continuum absorption. This contribution has been observed since early studies of QD spectroscopy and is often empirically modeled as a smooth, energy-dependent function, frequently approximated by a cubic dependence.[36, 51] The continuum transitions are often attributed to bulk-like high-energy

transitions, owing to the fact that at higher energies the excitons are sufficiently localized that quantum confinement effects are negligible.[52] However, the continuum absorption is observed to extend down to the lowest quantum-confined transition, and this assignment is untenable at energies that are comparable to the energies of transitions between discrete quantum-confined levels. Furthermore, in some cases (most notably, selenium-rich ZnSe QDs), the continuum extends to significantly lower energies than the lowest exciton.[53] The experimental studies in Ref. [53] report variations in the absorption spectra and molar extinction coefficients with changes in surface stoichiometry of ZnSe QDs. These results demonstrate the importance of surface states in the spectroscopy and photophysics of these QDs. Specifically, the spectroscopy of metal-rich and chalcogenide-rich surfaces in ZnSe and CdSe was studied and the results show a marked increase in the extinction coefficient and a significant tail to lower energy in the absorption spectrum of selenium-rich ZnSe QDs. No spectral tail was reported in the CdSe case. The authors indicate that this peculiar change in the absorption spectra must be connected to the surface electronic states but do not make any detailed assignment of the transitions for the tail or the increased absorption.

Several theoretical studies have shown that the in-gap trap states in II-VI and III-V QDs result from dangling bonds in surface chalcogenides, leading to surface hole traps and quenching of photoluminescence.[54–56] Experimental studies showed that surface stoichiometry and passivation of surface chalcogenides play a crucial role in the blinking and hole trapping in QDs.[56–65] Transient absorption studies have demonstrated that these surface chalcogenide states are responsible for surface charging, where a valence band electron temporarily occupies an empty surface chalcogenide level.[65–67] Morgan *et al.*[66] showed that the QD Fermi level plays an important role in this mechanism. A Fermi energy that is close to the valence band (VB) edge results in partially electron-filled levels that are thermally accessible from the VB ("surface charging"). Subsequent photoexcitation produces an effective trion state in the bulk of the QD, with an increased Auger recombination rate. A higher Fermi energy results in filled in-gap states and therefore in surface hole traps. It is important to assign the

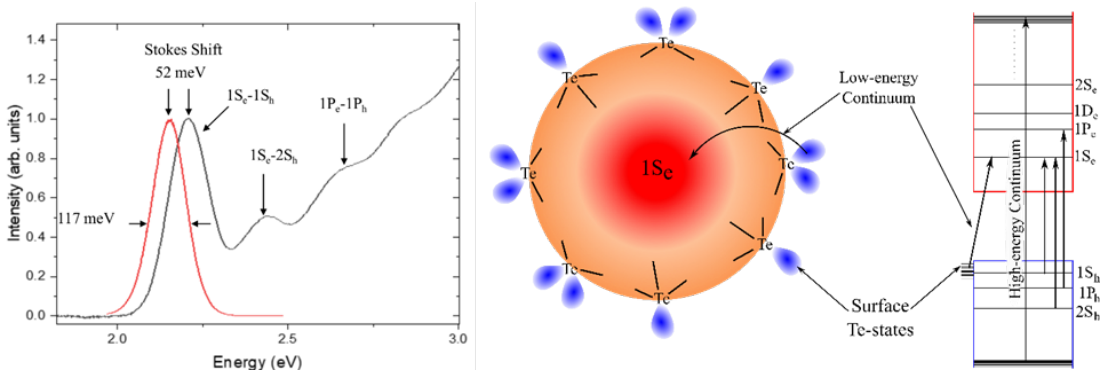


FIGURE 3.1: The absorption and luminescence spectra of CdTe QD with a schematic level diagram showing the initial and final states of the quantum confined transitions along with the transitions that contribute to the continuum.

continuum transitions since they contribute to a significant portion of the absorption intensity. Additionally, these surface states are of particular interest to industrial applications, particularly for the development of electroluminescent QLED displays,[68, 69] QD-based detectors,[70] etc. In this work, we systematically study the role of surface stoichiometry in the absorption spectra of CdTe QDs and demonstrate that the continuum absorption can be decomposed into two physically distinct contributions: the low-energy continuum, which is due to the presence of surface tellurium states (near the $1S_e$–$1S_h$ transition), and the high-energy continuum ($\sim$3.5 eV) with bulk-like transitions. This provides a physically intuitive framework for understanding continuum absorption in colloidal QDs. We further interpret the ZnSe data presented in Ref. [53] based on this model.

3.3 Surface Stoichiometry-dependent Spectroscopy

The absorption spectra of 3.2 nm diameter CdTe particles at varying stages of changing surface stoichiometry going from Cd-capped to Te-capped and partial reversal to Cd-capped are shown in Figure 3.2. The details on synthesis, surface treatments and spectroscopy are discussed in Appendix B.

The initial, purified particles have cadmium-rich surfaces due to the high excess of Cd-precursor in the synthesis reaction. This sample was treated with TOPTe to produce particles with increased amounts of surface tellurium (Te-CdTe). Subsequent treatment with $Cd(St)_2$ results in (incomplete) reversion to a Cd-rich surface. These changes in surface stoichiometry are further established from vibrational spectroscopy. The Fourier transform IR (FTIR) spectra are shown in Figure 3.3 and several of the spectral assignments are given in Table 3.1. The spectra show the peaks corresponding to Cd-ODPA on the surfaces of QDs, which markedly decrease in the Te-CdTe sample, while a prominent feature emerges at $\sim$1030 cm^{-1}. The intensity of this peak increases upon the addition of excess TOP, which indicates that this mode is connected to ligated surface tellurium; we tentatively assign it to a Te–P stretch mode. These changes are consistent with the change from Cd- to Te-capped QD surfaces.

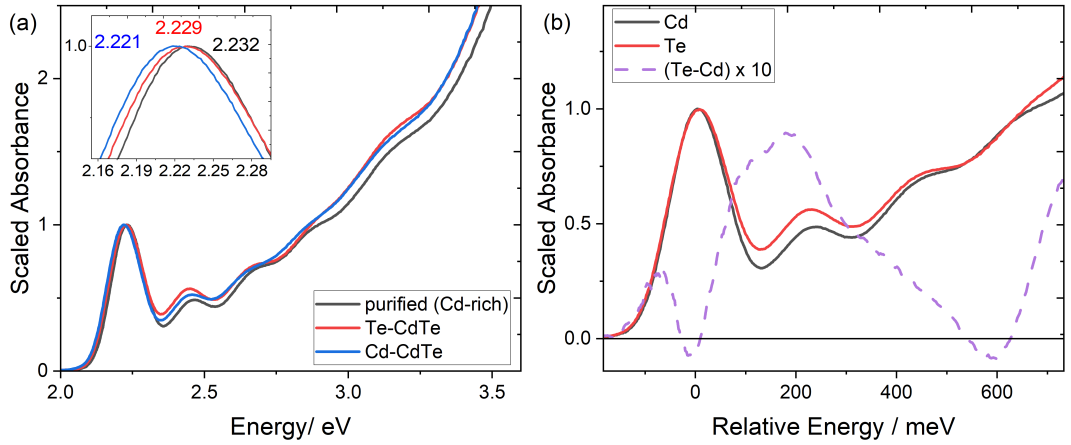


FIGURE 3.2: (a) Absorption spectra of purified particles (black), the purified particles treated with TOPTe resulting in the 'Te-capped' surfaces (red), followed by a treatment with $Cd(St)_2$ resulting in reversal to 'Cd-capped' nature (blue). The inset shows the closer look at the $1S_e$–$1S_h$ peaks of the absorption spectra, showing the red shift upon each successive surface treatment. (b) The same data as (a), plotted as a function of energy from the respective $1S_e$–$1S_h$ peaks, for comparison of the continuum contributions. The plot also includes the difference spectrum.

Figure 3.2 (a) shows that the initial, purified particles have $1S_e$–$1S_h$, $1S_e$–$2S_h$, and $1P_e$–$1P_h$ peaks at 2.232 eV (557 nm), 2.46 eV (505 nm), and about 2.7 eV (∼460 nm), respectively. The Cd- to Te-capped surface treatment results in several notable spectral changes: (i) a small redshift (∼1 nm) of the $1S_e$–$1S_h$ transition, (ii) an apparent increase in the $1S_e$–$2S_h$ peak intensity (15%), and (iii) a substantial increase in absorption within the valley (≈2.36 eV) between these transitions (26%). The increase in valley intensity cannot be accounted for by spectral broadening, which is minimal ∼4 meV, as shown in Figure B.2. As such, the emergence of this additional low energy continuum absorption indicates the presence of additional optical transitions.

To understand these spectroscopic changes, one must consider the effect of surface tellurium on the quantum-confined valence band wavefunctions. The valence band is composed mainly of tellurium *p*-orbitals, so addition of surface tellurium causes an expansion in the hole envelope function, reducing the extent of hole quantum confinement. This explains the observed redshift as well as a reduction in energy separation between the $1S_e$–$1S_h$ and $1S_e$–$2S_h$ peaks as is clear in Figure 3.2 (b). The expansion of the hole envelope function also predicts the relative decrease in the $1S_e$–$2S_h$ intensity due to a reduced overlap between the $1S_e$ and $2S_h$ envelope functions. Figure 3.2 (a)shows that the relative intensity of the $1S_e$–$2S_h$ peak increases, indicating the presence of an additional absorption transition in that spectral region. The $1S_e$–$2S_h$ peak-to-valley (2.36 eV in Figure 3.2 (a)and 125 meV in Figure 3.2 (b)) ratios indicate the same thing; in the purified particles the peak-to-valley intensity ratio is 1.55 and that decreases to 1.4 in the Te-CdTe case. This increased absorption is the low energy continuum, extending from the $1S_e$–$1S_h$ transition to about 2.7 eV. The relative intensity of this continuum is shown in the Te-CdTe minus purified difference spectrum,

Figure 3.2b. Ligand exchange results in small changes in the energies and intensities of the quantum confined transitions, which adds to the complexity of the difference spectrum. Figure 3.2a shows several partially resolved quantum confined transitions and a shift in the energy of any of these features will result in a derivative-like feature in the difference spectrum. These complexities make quantitative modeling of the difference spectrum problematic, and not such modeling will be attempted.

Despite the above difficulties, several qualitative and semiquantitative aspects of the additional low-energy continuum absorption are apparent in Figure 3.2b. The most obvious aspects of the difference spectrum are that it has an onset at about the same energy as the $1S_e$–$1S_h$ transition, a maximum at about 200 meV above that onset and much lower intensity above about 400 – 500 meV. The spectra in Figure 3.2 are normalized at the peak of the $1S_e$–$2S_h$ transition. If the continuum has significant intensity under the $1S_e$–$1S_h$ peak, then this normalization is not correct, and the maximum of the continuum could be at a relative energy below 200 meV. This is a relatively minor point, and the present results do not address this ambiguity. The integrated area of the low-energy part (E < 2.7 eV) of the absorption spectra increases by 7.5% upon becoming Te rich. Making the limiting assumptions that the low energy continuum is completely absent in the purified case and that surface exchange is complete in Te-CdTe, this suggests that the total low energy continuum oscillator strength is about 7.5% that of the combined $1S_e$–$1S_h$ and $1S_e$–$2S_h$ transitions. This is a lower limit and relaxing either of these assumptions increases this value. We suggest that an increased amount of surface tellurium leads to an increase in the density of surface states shown in the schematic in Figure 3.1, which in turn leads to a higher intensity of the continuum transitions overlapping this transition. The same type of low energy continuum is observed in other II-VI QDs. Several studies show that in CdSe QDs, the continuum onset matches the $1S_e$–$1S_h$ exciton energy, independent of the particle size. [53, 59] From this energy dependence we conclude that the continuum cannot be assigned to purely surface-state transitions. The electron effective mass is much less than that of the hole, so most of the quantum confinement is in the electron. Thus, the assignment depicted in Figure 3.1, a transition from the surface states to the 1S electron state, explains this coincident energy dependence.

As mentioned above, the continuum is reasonably intense, having an oscillator strength that is greater than 7.5% that of the $1S_e$–$1S_h$ and $1S_e$–$2S_h$ transitions. It is reasonable to ask whether the surface tellurium p-orbitals have sufficient overlap with the 1S electron wavefunction to give a significant oscillator strength. We note that in these $\approx$ 3.3 nm Te-CdTe particles, about 60% of the Te atoms are on the surface, so it is plausible that these transitions could have significant oscillator strength. To further address this question, we have calculated electron wavefunctions using methods analogous to that reported in reference [71]. In II-VI semiconductors, the conduction and valence bands are composed primarily of metal s-orbitals and chalcogenide p-orbitals, respectively. The calculated wavefunctions assume a soft potential wall at the outermost Cd atoms and give the integrated electron density at and beyond the surface Te atoms. This distance is taken to ¼ of the unit cell, 0.16 nm. The biggest uncertainty

in these calculations is the electron potential at the surface Te atoms compared to inside the particle. Literature values of the bulk electron affinity have some uncertainty, but there is a rough consensus that the bulk CdTe conduction band edge is about 3.6 eV below the vacuum level [72, 73], which is an upper limit on this value. However, the electron affinity of elemental tellurium is 1.97 eV, which would put this potential difference at about 1.6 eV. When the integrated wavefunction calculation is performed with this assumed potential differences, we find that 18% of the electron density extends beyond the surface tellurium atoms. We note that the calculation is sensitive to the assumed potential difference, which can only be roughly estimated. If the potential difference is assumed to be 1.0 and 2.0 eV, bracketing this value, we get values of 30% and 13%, respectively. This is a very approximate calculation that has many uncertainties. But it shows that electron-hole overlap considerations are consistent with having a significant amount of oscillator strength in the low energy continuum and hence the assignment in Figure 3.1.

The nature of the surface chalcogenide states has been studied extensively.[54, 57, 67] The coordination number, ligation, and strength of the ligand determine the electronic structure and level of electron filling of these surface states. When triply coordinated with core metal ions, the chalcogenide *p*-states are stabilized to be within the VB, while double or single coordination leads to in-gap dangling bonds. Bonding to a ligand stabilizes the chalcogenide *p*-orbitals further into the VB. The charge on the surface chalcogenide (reduced (Te^{2-}/Se^{2-}) or neutral (Te^{0}/Se^{0})) depends on the synthesis process[65, 74, 75] and determines the level of electron filling in these states, i.e., the Fermi level. When these in-gap states are empty they result in "surface charging", while filled in-gap states act as hole traps. These electrons in dangling *p*-orbitals, in-gap or in-band, can couple to the quantum-confined CB electronic states, and we posit that these transitions result in the low-energy continuum. The intensity of these transitions depends on the density of surface chalcogenide states and the overlap of the CB electronic wavefunction with the surface chalcogenide *p*-orbitals, along with QD Fermi energy dictating the onset energy.

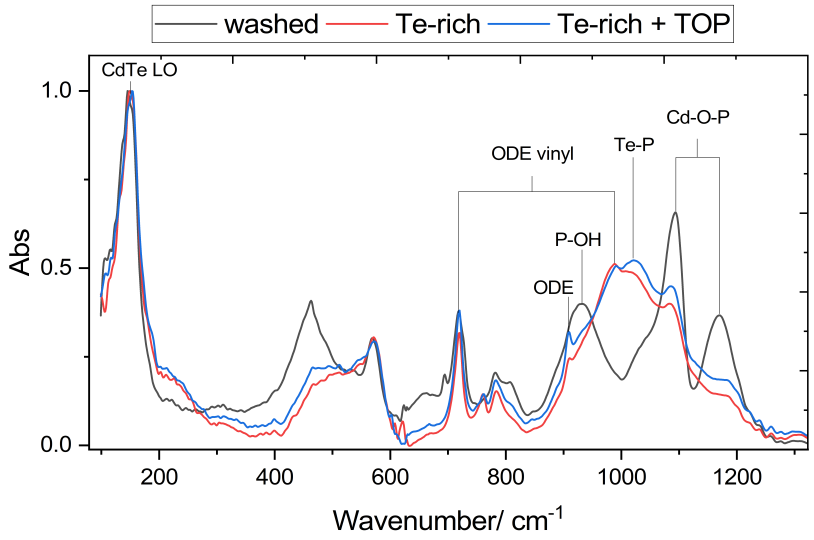


FIGURE 3.3: FTIR spectra of the purified particles (black), Te-capped particles (red) and Te-capped particles treated with TOP (blue). These spectra a normalized with respect to the CdTe LO phonon peak seen at $\sim$ 145 cm^{-1} since its intensity scales with the volume and number of QDs. The relevant peaks in the spectra are labeled and the assignment is shown in Table 3.1.

TABLE 3.1: Infrared peak wavenumbers and assignments.

Vibrational mode	**Freq. (cm^{-1})**	**Vibrational mode**	**Freq. (cm^{-1})**
CdTe LO phonon[a]	145	Cd–O–P[b]	1092.9, 1168.8
Alkyl C–C bending[c]	717	P–OH[b]	930.9
ODE vinyl group[c]	909, 988.7	Te–P	1030

[a]Ref. [76] [b]Ref. [64] [c]Ref. [65]

The Te-CdTe sample can be treated with $Cd(St)_2$ to passivate the surface tellurium. The additional layer of cadmium leads to an expansion in the electron envelope function, a further redshift of about 2 nm, and an increase in the $1S_e$–$2S_h$ intensity. The passivation of surface tellurium reduces the density of surface tellurium states and therefore a reduction of continuum intensity in the 2.2–2.5 eV region, as evidenced by the decrease in the valley between $1S_e$–$1S_h$ and $1S_e$–$2S_h$ peaks (seen in Figure 3.2 (b)). The spectrum does not completely return to that of the original "purified" sample, indicating an incomplete return to Cd-rich nature and that some unpassivated surface tellurium still contributes to the continuum intensity. This is also consistent with a PLQY increase to $\sim$40%, indicating that the cadmium-stearate treatment passivated some, but not all, the dangling chalcogenide bonds on the surface. We also note that Figure 3.2 (a)shows that the higher-energy ($\sim$3.5 eV) continuum sustains its intensity upon treatment with $Cd(St)_2$. This further indicates that partial passivation of the particle with $Cd(St)_2$ results in only a very small increase in the volume of the particle.

The larger redshift in the Cd-CdTe sample, regardless of the partial return to Cd-rich nature, is due to a higher sensitivity of electron energies to particle size compared to hole energies.

The observed spectral trends are consistent with the presence of two distinct contributions to the continuum absorption. The low-energy continuum exhibits a pronounced dependence on surface treatment, increasing under Te-capped conditions and decreasing upon Cd passivation, suggesting a significant contribution from surface-related electronic states. In contrast, the high-energy continuum shows comparatively weaker variation across the same treatments, consistent with a more bulk-like origin. We extend this idea to interpret the spectroscopy of CdSe and ZnSe QDs reported in the literature, in order to point out the subtleties of the role played by Fermi energy, bond energies, and tunneling of the conduction band electron in determining the onset and intensity of the continuum transitions.

3.4 Comparison with CdSe and ZnSe QDs

Lin *et al.*[53] show that the continuum transitions just above the lowest exciton are significantly more intense in Se-ZnSe QDs compared to the CdTe results in Figures 3.2. Furthermore, at energies near and slightly below the lowest exciton, the Se-ZnSe QDs exhibit a much more intense continuum. These differences can be qualitatively understood in terms of simple "toy-model" calculations, described below.

The central premise of these calculations is that the continuum absorption can be assigned to transitions from occupied surface chalcogenide states near the valence band edge to quantum-confined conduction band states. The absorption intensity depends on the density of surface states and the extent of conduction band electron overlap with the chalcogenide *p*-orbitals which extend from the particle surface. The overlap associated with these transitions depends on the extent to which the quantum-confined conduction band wavefunction spills into the classically forbidden region of the particle surface. The comparison of the extents of conduction band delocalization in CdTe versus ZnSe depends on the relative energetics, as summarized below.

The CdTe lowest exciton is at about 557 nm, corresponding to 2.23 eV. The bulk CdTe bandgap is 1.5 eV, so the total quantum confinement energy (ignoring electron–hole interaction) is 0.73 eV. Most of the quantum confinement energy (about 75%) is in the electron, so the electron quantum confinement energy is about 0.58 eV, and that of the hole is about 0.15 eV. Literature values of the bulk electron affinity have some uncertainty, but there is a rough consensus that the bulk CdTe conduction band edge is about 3.6 eV below the vacuum level. This puts the quantum-confined conduction band electron about 3.0 eV below the vacuum level. A similar calculation for the smallest ZnSe QDs in Ref. [53] (close to the size of the CdTe QDs used here) puts the electron and hole quantum confinement energies at 0.24 and 0.08 eV, respectively. The quantum-confined conduction band electron is at about 2.5 eV below vacuum. In II-VI semiconductors, the conduction and valence bands are composed primarily of metal *s*-orbitals and chalcogenide *p*-orbitals, respectively. In the case of a II-VI QD having chalcogenide surface

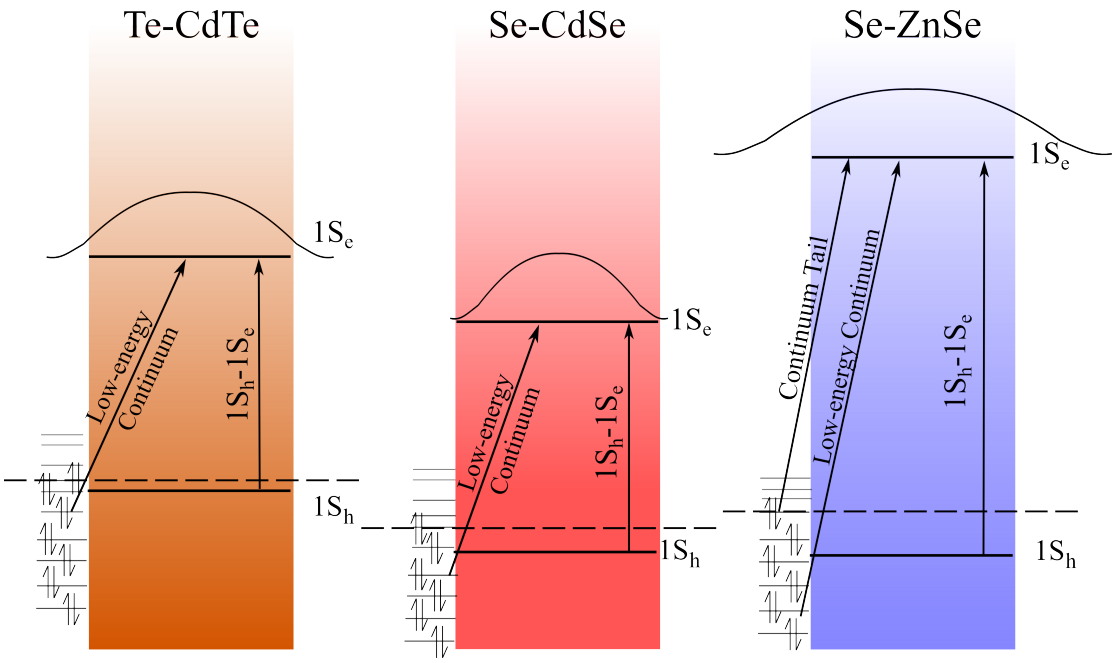


FIGURE 3.4: A schematic showing the varying level of conduction band tunneling and Fermi energy (dashed line) in Te-CdTe, Se-CdSe and Se-ZnSe QDs. The larger wavefunction overlaps and the higher Fermi energy in the Se-ZnSe QDs results in the higher continuum intensity and lower onset energy relative to the $1S_e$-$1S_h$ energy ('continuum tail')

termination, a simple particle-in-a-sphere model has the conduction band terminated at the outermost metals, with the surface chalcogenides in the nonclassical region. As such, the electron–hole overlap depends on the extent to which the conduction band electron tunnels the distance separating metal and chalcogenide lattice planes. This is an elementary quantum mechanics calculation:

$$\Psi(x) \propto \exp\left(-\frac{\sqrt{2m(E-V_0)}}{\hbar}\,x\right), \tag{3.1}$$

where V_0 is the energetic depth of the bulk conduction band below the vacuum level and E is the electron quantum confinement energy. If x is set to the distance separating adjacent metal and chalcogenide lattice planes, then $|\Psi|^2$ is proportional to the overlap and hence the continuum intensity. Putting appropriate values for CdTe and ZnSe and evaluating the metal–chalcogenide distance along the $\langle 111 \rangle$ planes, this calculation predicts the continuum to be a factor of 1.8 more intense in ZnSe compared to CdTe. This is in approximate agreement with the observed absorption spectra. The essence of the difference results from the ZnSe conduction band being a shallower well, resulting in increased tunneling to surrounding surface seleniums.

Another obvious difference between the Te-CdTe spectrum in Figure 3.2 and the Se-ZnSe spectra in Ref. [53] is the presence of the low-energy continuum tail in the Se-ZnSe case. We suggest that this difference can be understood in terms of the energy

difference between the valence band edge and the nonbonding surface chalcogenide p-orbitals. This energy difference is essentially the metal–chalcogenide bond energy and can be estimated from thermochemical data. We conclude that the ZnSe bond is significantly stronger than the CdTe bond (by about 1 eV; see Table 3.2 for details of the calculation). The CdSe case is very similar to CdTe. As such, the dangling p-orbitals are further into the gap, above the valence band in the ZnSe case. For transitions from these orbitals to occur, they must also be filled, i.e., they must be below the Fermi level. We note that elemental selenium is much easier to reduce than tellurium, by about 0.47 V. This will put the Fermi level correspondingly higher and make it more likely that the dangling p-orbitals are filled. To the best of our knowledge, Se-ZnSe is the only II-VI QD that exhibits the red continuum tail. We suggest that it is the combination of these factors that results in this unusual behavior.

TABLE 3.2: We calculate the bond energies from standard enthalpy of formation (ΔH_f) for the reaction MX(s) $\rightarrow$ M(g) + $\frac{1}{2}$ X_2 and then to calculate the bond dissociation energy (BDE) as: $\mathrm{BDE(MX)} = \Delta H_f + \frac{1}{2}\,\mathrm{BDE}(X_2)$

Compound	ΔH_f (kJ/mol)	X_2 BDE (kJ/mol)	BDE of MX (kJ/mol)
CdTe	364*	260**	494 (5.1 eV)
CdSe	405*	329**	569 (5.9 eV)
ZnSe	429*	329**	594 (6.2 eV)

*ref. [77] **ref. [78]

3.5 Ligand to QD Continuum Transitions

We have thus far only considered surface chalcogenide to QD conduction band transitions. We can also consider analogous transitions from ligand chalcogenide atoms, as shown in Figure 3.5 .

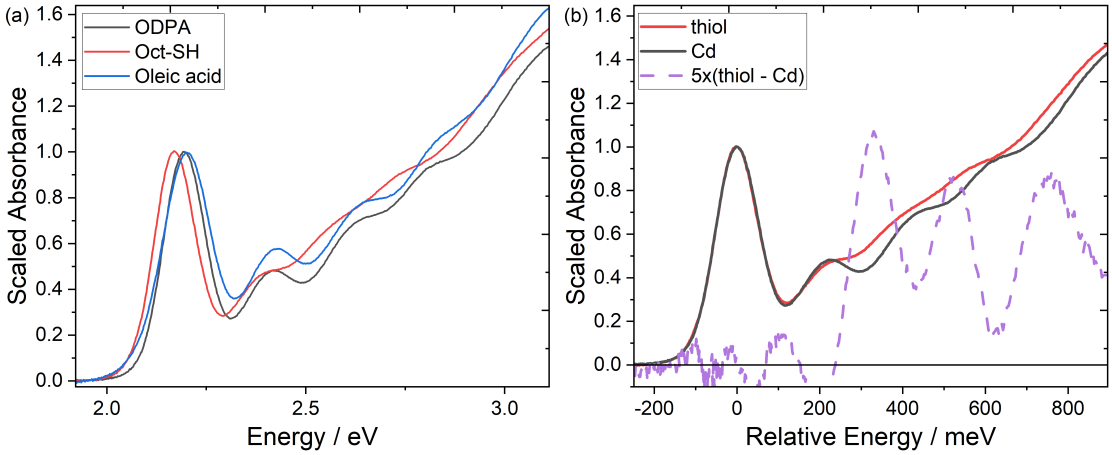


FIGURE 3.5: (a) Absorption spectra of CdTe QDs ligated with ODPA (black), octanethiol (red) and oleic acid (blue). (b) The same ODPA and octanethiol spectra as in (a), except plotted as a function of energy from the lowest exciton peak and including the scaled difference spectrum.

The CdTe QDs are synthesized with cadmium-rich surfaces ligated with ODPA. These particles are ligand-exchanged with octanethiol and then subsequently ligand-exchanged with oleic acid. The increased continuum seen upon exchange from ODPA to octanethiol ligands is largely lost upon removal of the octanethiol, showing that this increase is specific to alkylthiol ligation. There is however an increase in the surface tellurium related continuum due to etching upon treatment with oleic acid. Removal of octanethiol ligands with cadmium oleate in similar QDs demonstrates that the octanethiol-related continuum is fully reversible, Figure B.3.

Figure 3.5b shows the thiol minus purified difference spectrum. As in the case of the difference spectrum shown in Figure 3.2b, there are derivative-like features due to small shifts of the quantum confined peaks. Figure 3.5 shows that the change from ODPA to octanethiol ligation causes several changes in the spectrum. There is an obvious decrease in the intensity of the $1S_e$–$2S_h$ transition. This is due to a slight delocalization of the hole onto the ligands.[79] The increase in the spatial extent of the hole decreases the overlap of the $2S$ hole state with the $1S$ conduction band electron, which decreases the intensity of this transition. Figure 3.5 b also shows an increased intensity of the low-energy continuum, with the additional intensity having an onset at about 200 meV above the $1S_e$–$1S_h$ exciton. This is very different from the Te-CdTe continuum in Figure 3.2, which has an onset at the $1S_e$–$1S_h$ exciton, as depicted in Figure 3.4 . The increased absorption is assigned to transitions from the p-orbital lone pair electrons of octanethiol to the QD conduction band. The molecular orbitals involved in this transition are lone pair $3p$-orbitals on sulfur atoms that are bonded to the alkyl chain and to surface cadmiums. They are part of the octanethiol molecule and are expected to exhibit less energetic inhomogeneity than in the case of the surface tellurium atoms, which can be in very different environments depending on the local morphology (surface facet, edge, corner, etc.). The nonzero onset energy can be understood in terms of the ligand energetics. The energy of the sulfur lone pair orbitals can be established by

a comparison of trapping dynamics: alkyl thiols trap holes and thereby quench luminescence in mid-sized CdSe, but not CdTe QDs. The absence of hole trapping indicates that the energies of these orbitals cannot extend to within a few kT of the CdTe VB edge. Conversely, the well-known hole trapping with CdSe indicates that these orbitals are above the CdSe valence band edge. The valence band edge potential is about 0.5 V more positive (further from the vacuum level) in CdSe compared to CdTe,[73, 80] so this tightly brackets the energy of the sulfur $3p$-orbitals. This indicates that with CdTe, the transitions from these orbitals must be at least several kT ($kT = 26$ meV) above the lowest exciton, but the onset of these transitions cannot be more than about 500 meV above the lowest exciton. This is in agreement with the $\approx$200 meV onset seen in the spectra in Figure 3.5 .

3.6 Conclusion

This chapter presents data that demonstrate that the absorption continuum in CdTe QDs consists of two physically distinct contributions: a high-energy contribution corresponding to bulk-like transitions, and a low-energy surface-dependent contribution. Systematic modification of the QD surface from Cd-rich to Te-rich conditions produces a pronounced increase in the low-energy continuum between the $1S_e$–$1S_h$ and $1S_e$–$2S_h$ transitions. The strong dependence of this spectral region on surface treatment, together with its size-dependent onset observed across multiple II–VI quantum dots, demonstrates that these transitions are from occupied surface chalcogenide states into quantum-confined conduction band levels. In contrast, the high-energy continuum exhibits comparatively weak sensitivity to surface stoichiometry and is consistent with bulk-like transitions that scale primarily with particle volume.

This framework also provides an interpretation of previously reported spectroscopy in ZnSe and CdSe quantum dots. In particular, the substantially stronger continuum observed to the red of the first exciton peak in selenium-rich ZnSe QDs can be understood in terms of enhanced tunneling of the quantum confined conduction band electron into the surface selenium layer, along with differences in the energetics of selenium and tellurium dangling-bond levels. We also find that transitions involving non-bonding electrons in alkylthiol ligands can result in a similar low-energy absorption continuum. These results establish that the low-energy continuum absorption in semiconductor quantum dots is connected to surface stoichiometry, surface electronic structure, and the electronic structure of the ligands.

4 Photophysics of Silver Indium Gallium Sulfide (AIGS)

4.1 Abstract

This chapter presents the static spectroscopy and radiative dynamics of very high quality, well characterized silver indium gallium sulfide (AIGS) quantum dots. This work was published in The Journal of Chemical Physics [81]. This was a collaborative endeavor, requiring spectroscopy performed by the author of this thesis, analysis by the author and Professor David Kelley, sample synthesis and EDX measurements performed by collaborators at Nanosys-Shoei Chemicals, EDX analysis performed by Professor David Kelley, and Monte Carlo structure calculations and subsequent EMA wavefunction calculations performed by Professor Anne Myers Kelley.

We find that the static spectroscopy and radiative dynamics are is very different than in II-VI and III-V quantum dots. The absorption spectrum is broad and featureless, but sharp, high quantum yield (90%) band edge photoluminescence is observed. Despite the spectrally sharp photoluminescence, theThe photoluminescence decays are long and nonexponential, having components ranging from 40 to 150 ns. The spectroscopy and radiative kinetics are understood in the context of the radial composition profile of each element, as determined by EDX line profiles. The radially dependent compositions show that the core is largely Ag_2S with the fraction of gallium increasing with radial distance. We suggest that random spatial fluctuations in the local silver concentration localize holes at the most silver-rich regions of the particle. The lowest energy transition is nominally parity forbidden and the parity selection rule is relaxed in the random alloy crystal environment. The sites at which holes localize have varying degrees of local crystal asymmetry and varying magnitudes of internal electric fields. Both types of perturbations can break the local symmetry and thereby relax the parity selection rule, giving rise to inhomogeneity in the radiative rates. We also consider the possibility that the nonexponential photoluminescence decay kinetics can be explained by a delayed emission model, but consider this to be less likely than the inhomogeneous radiative rate model.

4.2 Introduction

Silver indium gallium sulfide (AIGS) belongs to a class of alloyed semiconductor I-III-VI materials that have attracted interest as Cd/Pb-free nanocrystals with solution processability and size- and composition-tunable bandgap energies. These materials find

applications in quantum dot (QD) display technology, luminescent solar concentration, photovoltaics, and bio-markers for imaging biological matter. They are of particular interest to the display industry because the conduction and valence band energies can be engineered to be suitable for high quality, stable electroluminescent display devices. These applications require a deeper understanding of the factors (inhomogeneity, defects, etc.) that control the photophysics. Despite high interest, the complex defect chemistries and structural disorder of I-III-VI QDs still present major challenges to understanding and controlling their spectroscopic and photophysical properties.

Many types of semiconductor QDs exhibit a combination of spectrally narrow photoluminescence (PL) with near unity PL quantum yield (QY), which is desirable for display applications. However, most I-III-VI QDs exhibit very broad and strongly Stokes-shifted PL. This emission is typically assigned to radiative recombination of carriers trapped at donor and acceptor sites. This donor-acceptor-pair PL typically has a very slow (hundreds of nanoseconds) radiative lifetime that is strongly dependent on the detection wavelength. Nonradiative processes can effectively compete with the slow radiative decay, and I-III-VI QDs rarely exhibit high PLQY. There have been a few recent reports of band-edge luminescence in I-III-VI QDs, specifically $AgInS_2$-based core/shell structures.[82–87] The shell material is usually Ga_2S_3 that upon deposition undergoes interdiffusion into the core. As a result, these are not really core/shell particles and are better thought of as graded-composition $AgIn_xGa_{(1-x)}S_2$ (AIGS) QDs. Prior to Ga_2S_3 deposition, the $AgInS_2$ core particles exhibit primarily broad trap PL. However, after gallium addition, these particles give very little trap emission and high quantum yield band-edge emission that is of comparable spectral width to their II-VI and III-V counterparts, i.e., less than 30 nm. The band-edge PL kinetics are multiexponential, having components from about 50 to over 200 ns. This is a much faster overall decay than the trap emission seen prior to gallium deposition, but much slower than the PL decays seen from the more conventional II-VI and III-V semiconductor QDs. Multiexponential PL decays are usually associated with an inhomogeneous distribution of nonradiative decay rates. The presence of nonradiative decay processes shortens the excited state lifetime and hence the observed PL decay. Some particles have larger nonradiative rates than others, giving rise to multiexponential kinetics. However, nonradiative electron-hole recombination also lowers the PLQY, whereas in Ref. [82] the measured PLQY is quite high, greater than 75%. The high overall PLQY eliminates heterogeneous nonradiative rates as a possible explanation for the nonexponential decays. No mechanism for the multiexponential decay is discussed in Refs. [82, 83, 85].

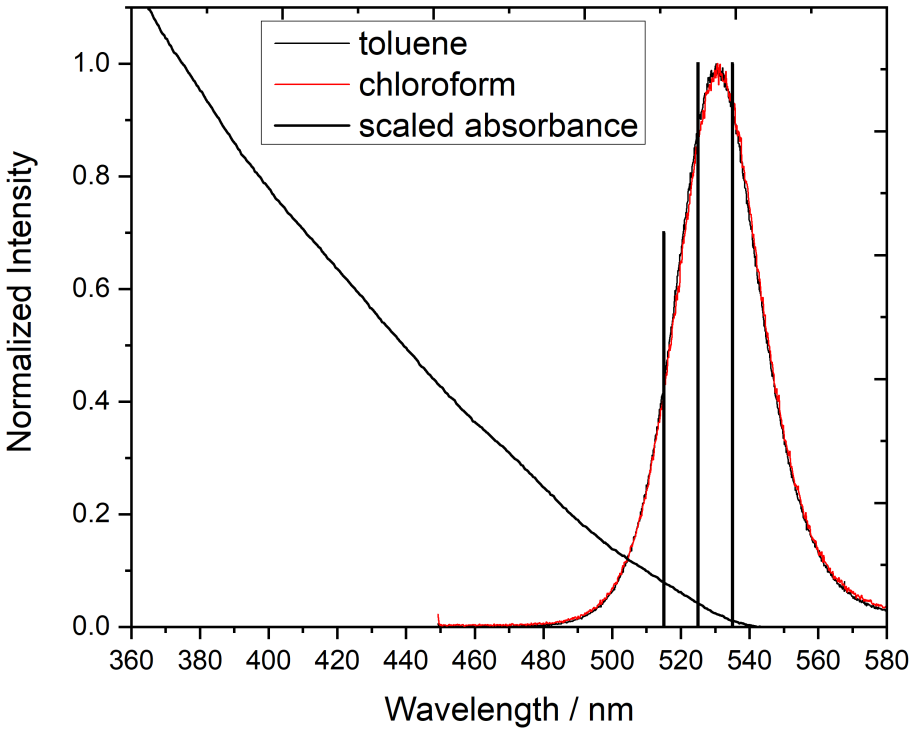


FIGURE 4.1: Absorption and PL spectra for AIGS QDs in chloroform and toluene. The vertical lines at 515, 525 and 535 nm indicate the detection wavelengths for the PL decays and PLE anisotropy spectra.

Very different spectroscopy and photophysics are seen in the more common and better understood II-VI and III-V QDs, such as CdSe or InP and their core/shell analogs. The presence of a larger bandgap shell passivates the surface states, reducing or eliminating nonradiative charge recombination centers. High-quality CdSe- and InP-based core/shell QDs have near-unity PLQY and exhibit single-exponential PL decays. For these particles, an analysis of the absorption extinction coefficients through the Einstein relations predicts a radiative lifetime that is on the order of 2 ns.[88] The observed radiative lifetime is an order of magnitude longer, on the 20–30 ns timescale.[89] This difference is well understood and results from the angular momentum fine structure.[90, 91] The lowest energy exciton consists of several fine structure states. The lowest energy fine structure state is optically dark, and emission occurs from a thermal population of higher lying optically allowed states. The fractional population in the bright states determines the overall exciton radiative lifetime and hence PL decay rates.

In this chapter we examine the spectroscopy and photophysics of very high quality AIGS QDs with the goal of understanding the spectroscopy and unusual radiative kinetics seen in these particles. The present QDs exhibit band-edge PL that is almost

completely free of trap state emission and has a very high PLQY (∼90%). The structure of these quaternary particles is complicated and directly linked to their spectroscopic characteristics. The nature of any quaternary alloy is to exhibit considerable structural inhomogeneity which can make the analysis of spectroscopic data difficult and ambiguous. We address this problem and characterize the structural complexity through elemental energy dispersive x-ray spectroscopy (EDX) linescan data. These data, along with the overall elemental analysis, allow for the accurate determination of the average radial composition profile (RCP) for each element. This average RCP, along with the random nature of how the metals are incorporated into the sulfide lattice during particle growth, provides the basis for Monte Carlo calculations of nanocrystal structures. The calculated heterogeneous structures along with known band offsets and effective masses permit the calculations of the electron and hole wavefunction for each structure. The calculated wavefunctions and the inhomogeneity of these wavefunctions and their energies facilitate modeling of several aspects of the spectroscopy and radiative dynamics.

4.3 Spectroscopy of AIGS Dots

The absorption spectrum shown in Figure 4.1 is very broad and almost featureless; it has no sharp, resolved lowest exciton. This is quite unlike II-VI and III-V QDs which show several well-resolved excitonic features. However, the PL spectra are narrow and have very little trap PL, which is not very different than what is seen in II-VI and III-V QD PL spectra. The narrowness of the PL spectrum eliminates the possibility that the diffuse nature of the absorption spectrum is due to inhomogeneous broadening. The above comparisons suggest that the electronic structure of AIGS QDs is very different than that of the more conventional II-VI and III-V QDs. Figure 4.1 also shows that the PL spectrum in chloroform is red shifted from that in toluene by a small amount, about 0.6 nm. This shift is small but completely reversible. It suggests that the excited state has a significant dipole, and that the dipole is stabilized by the higher dielectric constant of the chloroform solvent. This indicates that there is some charge transfer character in the excited state and that the electron and hole wavefunctions are not spherically symmetric. The magnitude of the excited state dipole is discussed in Section 4.7. The assignment of some excited state charge transfer character is consistent with the PLE anisotropy spectrum, shown in Figure 4.2. If the absorbing and emitting oscillators are perpendicular, an anisotropy of -0.2 is obtained. Anisotropies of 0.1 and 0.4 are characteristic of planar and linear oscillators, respectively.[92] Figure 4.2 shows that at small energies, the anisotropy is greater than 0.10, implying that the absorption and emission approach being colinear, as one would expect for a transition with significant charge transfer character in the excited state. We will return to this point later. Figure 4.2 also shows a comparison with a PLE anisotropy spectrum of InP/ZnSe/ZnS QDs. This spectrum shows far less positive anisotropy at small energies and negative anisotropies between 100 and 350 meV, underscoring the difference in the electronic structure of AIGS compared to InP-based QDs.

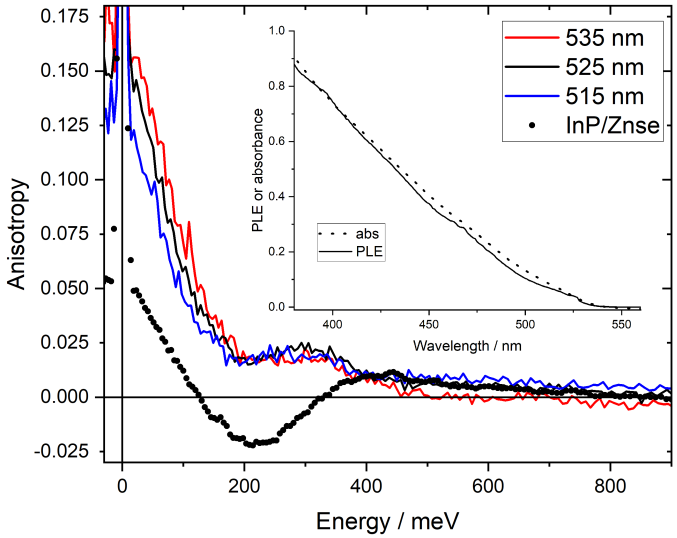


FIGURE 4.2: Photoluminescence excitation anisotropy spectra of the AIGS QDs at the indicated detection wavelengths. Also shown (for comparison) is the PLE anisotropy of InP/ZnSe/ZnS QDs [23] having a comparable PL maximum wavelength.

Much of the nature of the excited state is elucidated by the PL decay kinetics, which are shown in Figure 4.3. These kinetics are simplified by the high PLQY (∼90%), which allows us to ignore nonradiative processes. These kinetics are strongly nonexponential but can be adequately fit by a biexponential. Residuals indicate that the decays do not follow a clean biphasic decay; there are faster, slower, and intermediate components. However, a two-exponential fit gives a reasonable measure of the decay timescales. The fitting parameters are given in Table 4.1.

TABLE 4.1: Biexponential fitting parameters to $I(t) = A_f \exp\left(-t/\tau_f\right) + A_s \exp(-t/\tau_s)$, where τ_f and τ_s are the fast and slow decay times and A_f and A_s are the fast and slow amplitudes, respectively. The decays are normalized such that $A_f + A_s = 1$.

	Chloroform		Toluene	
	τ_f, A_f	τ_s	τ_f, A_f	τ_s
Blue	45.2 ns, 0.579	124.6 ns	41.5 ns, 0.615	115.5 ns
Peak	48.6 ns, 0.601	136.1 ns	44.4 ns, 0.647	128 ns
Red	53.2 ns, 0.617	152 ns	45.4 ns, 0.631	134 ns

In both chloroform and toluene solvents, the fast and slow decay times vary with detection wavelength across the PL band. Comparison of the fast and slow time constants at different detection wavelengths shows that they approximately follow the ν^3 dependence required by electrodynamic coupling of a dipole to the radiation field.[93]

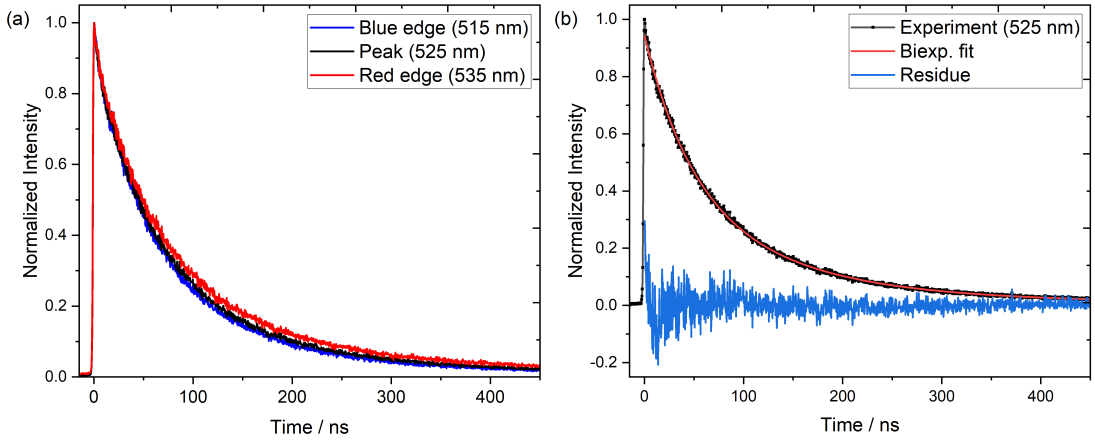


FIGURE 4.3: (a) PL decays of AIGS QDs in chloroform, taken with detection on the blue edge (515 nm), center (525 nm), and on the red edge (535 nm) of the band edge PL spectrum. The decays are fit to biexponentials and the fitting parameters are given in Table 4.1 (b) The fit and residuals for the 525 nm fit.

The relative amplitudes of the fast and slow components are independent of detection wavelength within experimental error.

4.4 Structural Characterization

In the analysis presented here, we consider the spectroscopy described above in the context of the structure, and specifically, the structural inhomogeneity. The average structure is characterized by the RCP for each element and is obtained from a combination of EDX measurements (Figure 4.4) and ICP elemental analysis. The RCP calculated is further used to model the inhomogeneity in these QDs via Monte Carlo calculation of structures that on average follow the RCP. EMA wavefunctions were calculated for these structures to interpret the photophysics of these QDs.

4.4.1 EDX Results and RCP Calculation

This section presents and discusses the EDX data collected by our collaborators at Nanosys-Shoei Chemicals, and RCP calculations from this data, performed by Professor David Kelley.

EDX directly images the positions of different atoms across a line-scan that goes through the center of the particle. As we discuss below, this does not yield the RCP directly and EDX linescans are inherently noisy (see Figure 4.5). To circumvent these difficulties, we take an approach of calculating the RCP for particles in which particle growth is modeled by a set of rate equations appropriate to the precursor concentrations used in the synthesis. This set of coupled differential equations can be integrated

using the known starting precursor concentrations as initial conditions and the precursor reaction rate constants as adjustable parameters. Although the actual particle growth reactions are probably more complicated than this assumption, this provides a reasonable and tractable approximation to the overall particle structure. The relative reaction rate constants are set to meet two criteria: the calculated linescan-integrated EDX vs. ICP elemental ratios match the experimentally determined values, and the calculated RCP fits the position-dependent linescan data, averaged over 10 particles. Taking the total elemental compositions obtained by summing several linescans averages out much of the noise and the integrated elemental ratios can be obtained quite accurately. The RCP calculated for each element is shown in Figure 4.6 and the experimental and calculated atomic fractions are given in Table 4.2.

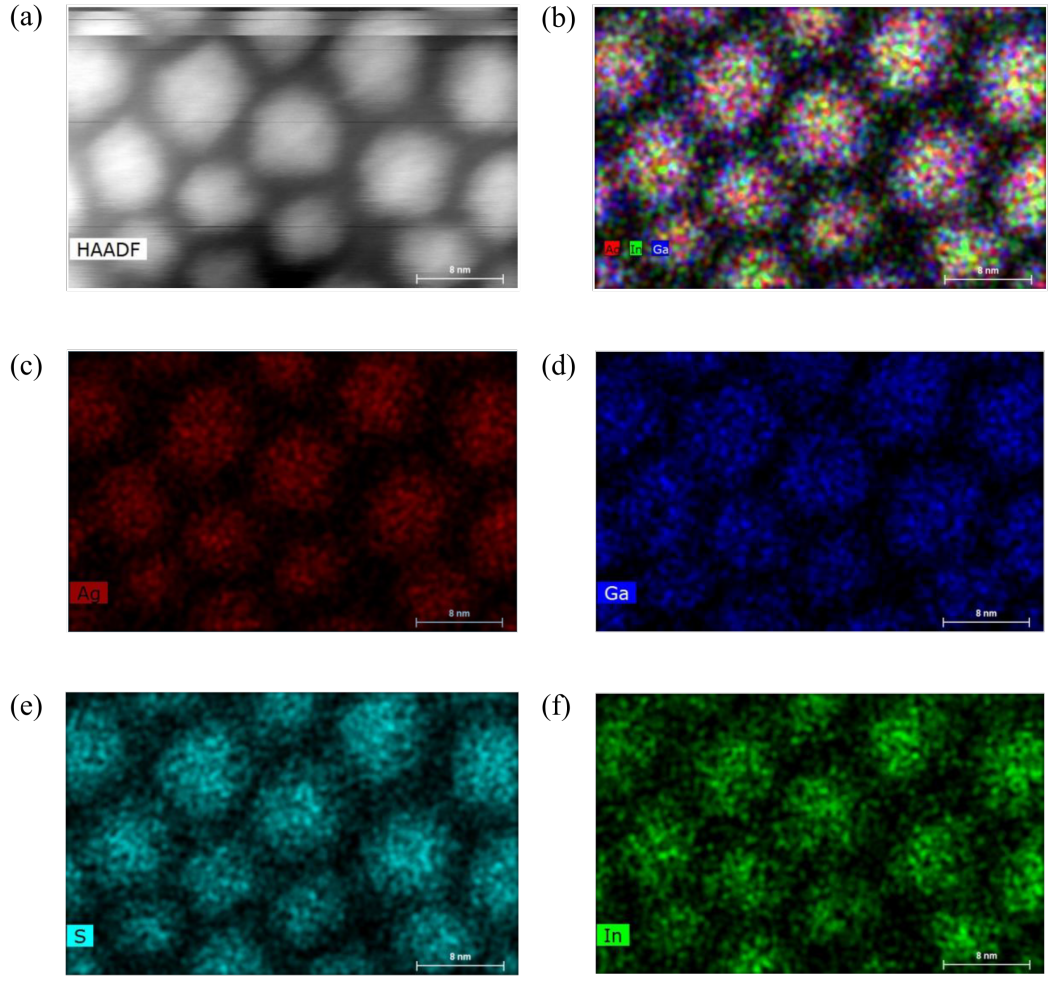


FIGURE 4.4: (a) The high-angle annular dark field TEM image of a representative sample. (b) The same image with the composite of the different elemental components: Ag (red), Ga (dark blue), S (light blue) and In (green), obtained through EDX measurements. (c-f) The elemental maps of the individual elements as shown at the lower left corner of each panel.

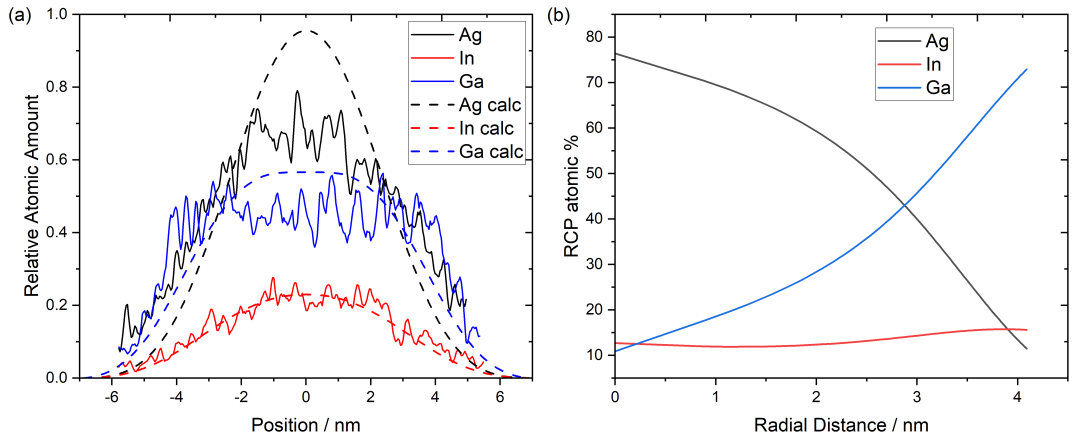


FIGURE 4.6: (a) The radial profiles of atomic contributions obtained from averaging linescans from 10 particles (solid lines) and the fitted radial profiles (dashed lines). (b) The radial composition profile of the metals calculated from the differential equations describing the particle growth process and the relative atomic amounts.

TABLE 4.2: Experimental and calculated atomic fractions.

	ICP		EDX linescan		ratio	
	Exp.	(Calc.)	Exp.	(Calc.)	Exp.	(Calc.)
Ag	0.397	(0.388)	0.473	(0.458)	1.19	(1.18)
In	0.143	(0.150)	0.142	(0.135)	1.0	(0.90)
Ga	0.461	(0.462)	0.385	(0.407)	0.835	(0.88)

Central to this approach is the simple observation that the elemental composition obtained by integrating a linescan through the particle center oversamples the core of the particle. Thus, comparison of integrated linescan elemental analysis with ICP elemental analysis gives a measure of how much each element is concentrated or depleted in the core of the particle. This idea is somewhat non-intuitive but can be qualitatively seen from the following considerations. Integration of a set of non-overlapping elemental linescans that cover the entire particle will obviously give the same total composition as an ICP elemental analysis. However, integration of linescans that do not go through the center or just graze the edge of the particle only sample the outer part of the particle. It follows that linescans through the center of the particle oversample the core. This is not a small effect. Consider the comparison of a core/shell particle with the core and shell having equal volumes, to the corresponding uniform alloy. In the case of the core/shell particle, the core radius is $(1/2)^{1/3}R = 0.794\,R$, where R is the total radius. As derived in the Reference [81], the integrated EDX signal for the core atom in the core/shell morphology is $S_{\text{tot}} = \pi(0.794R)^2\Delta y$, where Δy is the width of the EDX beam. By comparison, the signal in the uniform alloy case is $S_{\text{tot}} = 0.5\pi R^2\Delta y$. Thus, the core atom signal for the core/shell case is larger by a factor of 1.26. Similarly,

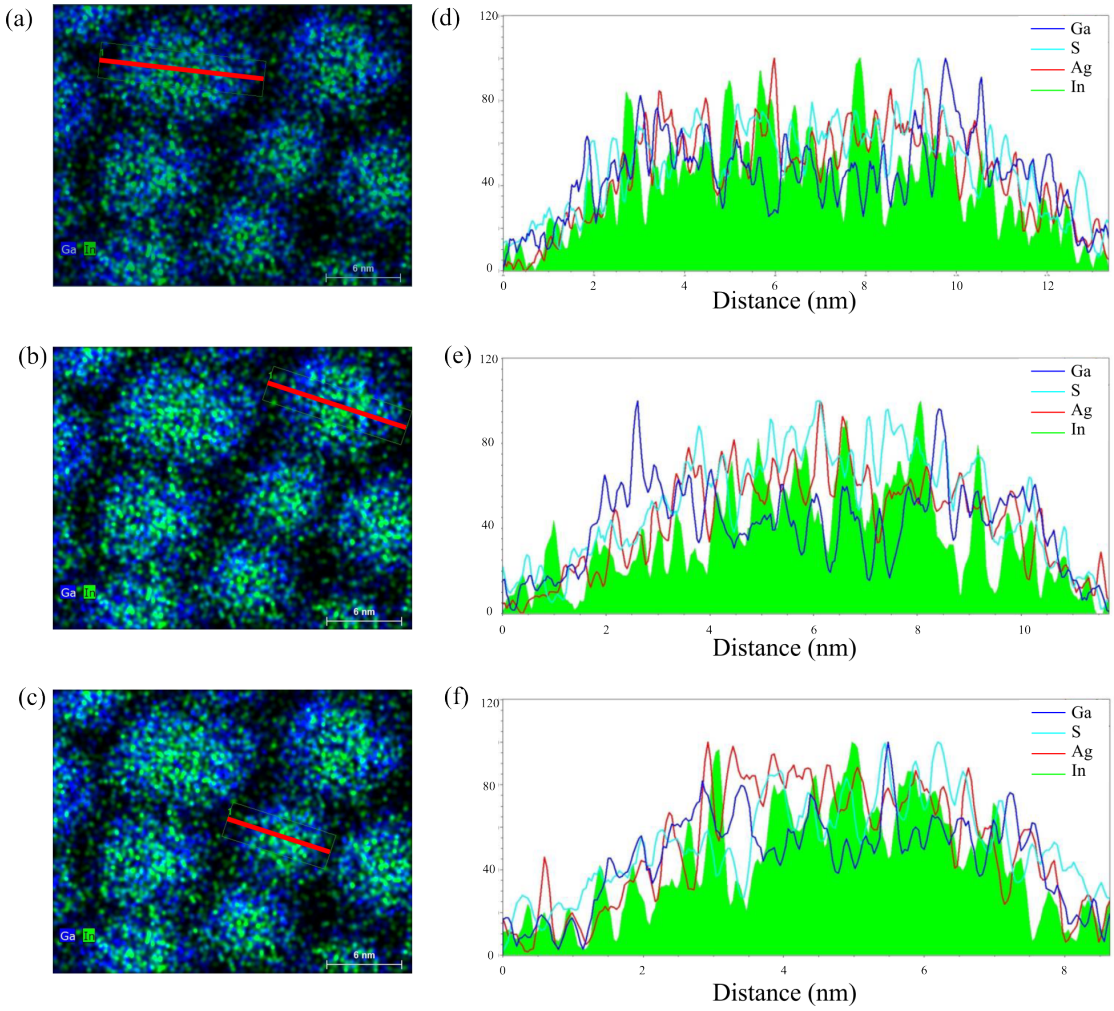


FIGURE 4.5: Figures a – c show representative elemental composites obtained through EDX measurements. The red line marks the region scanned to produce the elemental cross section plots shown in Figures d-f. Figures d – f show the occurrence of Ga (dark blue line), S (light blue line), Ag (red line) and In (green area) across the respective cross sections. The noisy signal makes it difficult to directly estimate the radial composition profiles from EDX scan cross-sections.

the shell atom signal is $0.37\pi R^2 \Delta y$, a decrease of 26% compared to the uniform alloy case. This example, and all the analysis done here, assumes the simplest possible case where the sample is much thinner than the electron penetration depth and the x-ray scattering length. This is a good approximation for 8.1 nm QDs on a TEM grid. The more general cases are rather complicated but well understood.[94]

Based on the RCP in Figure 4.6 (b) and the known band offsets one can use a simple particle-in-a-sphere effective mass model to estimate the electron quantum confinement energy. If the sphere is taken to have a radius of 4.1 nm and the effective mass is taken to be $0.15\,m_e$, then an energy of 150 meV is calculated. This is significant, but not very large. However, the conduction band offset between Ag_2S and Ga_2S_3 is about 0.8 eV. When considered in the context of the RCP in Figure 4.6 we conclude that a reasonable approximation is to consider the particle to be a graded-interface core/shell particle. In that case the electron is spread over the entire particle, but somewhat localized within a radius of about 2.5 nm. With this approximation, the quantum confinement energy is calculated to be about 400 meV, which is very significant. From these considerations we conclude that the lowest exciton energy in these particles depends primarily on the overall composition, but significantly on quantum confinement considerations of the size and RCP.

4.4.2 Structural Inhomogeneity and Wavefunction Calculations

This section presents the Monte Carlo calculations performed by our collaborator Prof. Anne Myers Kelley to model the structural inhomogeneity in the AIGS strucutres based on the RCP calculated in the last section. This calculation starts with a sphere of face-centered cubic sulfur atoms having a radius of 4.1 nm. There are twice as many tetrahedral holes as there are sulfur atoms and each tetrahedral hole has either an Ag, an In, a Ga, or is vacant. The overall approach to modeling this local inhomogeneity treats the probabilities of each tetrahedral hole having one of the metal ions or being vacant as being random, subject to the constraint of producing the correct RCP on average. This is implemented in the following way. The identity of the species in each tetrahedral hole is determined by first putting in Ag, Ga, or neither (an unoccupied tetrahedral hole), and then converting the appropriate fraction of the Ga to In in a second step. In the first step, let $F(r)$ be the fraction of cations that are Ag from the radial composition profile, while $A(r)$ is the fraction of all tetrahedral holes occupied by Ag and $G(r)$ is the fraction of all tetrahedral holes occupied by Ga. With these definitions,

$$F(r) = \frac{A(r)}{A(r) + G(r)} \tag{4.1}$$

and charge balance requires $1 = A(r) + 3G(r)$. Solving these two equations gives

$$A(r) = \frac{F(r)}{3 - 2F(r)}, \tag{4.2}$$

from which we can solve for $A(r)$ and $G(r)$ in terms of $F(r)$. The fraction of unoccupied tetrahedral holes is then $1 - A(r) - G(r)$. This is implemented using a Fortran

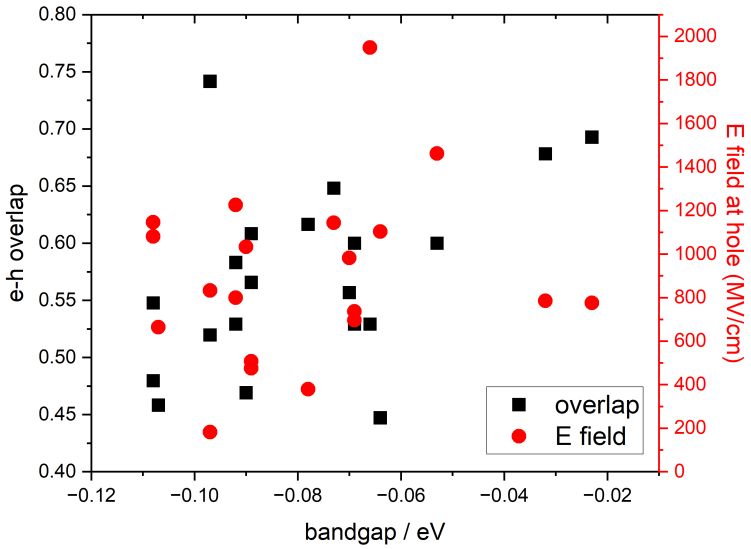


FIGURE 4.7: Calculated electron-hole overlap and electric field strength averaged over the hole density, plotted versus the relative energy of the lowest exciton, for 20 structures.

function which returns a random real number R between 0 and 1. The species in each site is set to Ag if $R \leq A(r)$, to Ga if $A(r) < R \leq A(r) + G(r)$, and to empty if $R > A(r) + G(r)$. In the second step, Ga is converted randomly to In with a probability to match the RCP. The structural characterization described above shows that these particles have a large spatial gradient in the concentrations of the different cations. Superimposed on these gradients is considerable randomness in the local cation environment in different regions of the particle, as well as inhomogeneities among different particles. This approach mimics the random nature of particle growth and models both types of structural inhomogeneities. After establishing the atomic structure of the Monte Carlo generated particles, the next step is to construct position-dependent valence and conduction band potentials. The valence band energy for Ag_2S is considerably less negative (closer to the vacuum level) than for $AgInS_2$ or $AgGaS_2$, while the conduction band energy is higher for $AgGaS_2$ than for $AgInS_2$ or Ag_2S.[95–103] The details of how these values are used to construct the locally variable band potentials are given in Appendix **??**. One limitation of these calculations is that they ignore band-bowing considerations. Although band-bowing parameters are available for many II-VI alloys,[104] as far as we can determine, these parameters for AIGS alloys are not available in the literature. The large potential differences result in considerable inhomogeneity in the electron and, particularly, hole wavefunctions within each particle and from one particle to another. The holes, with their greater effective mass,[97] tend to localize at Ag-rich regions near the center of the particle, while the electrons are more delocalized. To the extent that the holes are not at the particle center, the interaction with the electron will create an excited-state dipole. We suggest that this is the

reason for the linear oscillator component in the PLE anisotropy spectra shown in Figure 4.2 and the red shift of the PL spectrum in chloroform compared to toluene. The magnitudes of these calculated dipoles are discussed in the Section 4.7.

To explore the effects of this structural inhomogeneity on the spectroscopic properties, effective mass approximation wavefunction calculations were carried out on the atomistic models of the AIGS QDs described above. The electron and hole wavefunctions and energies were found by diagonalizing the effective mass approximation Hamiltonian in a basis of particle-in-a-sphere wavefunctions.[105] The potential energies for electrons and holes at each location in the particle were determined by their nearest neighbor cations: for holes, -0.8 eV (for all Ag) to 0 (for no Ag), and for electrons, 0 (no Ga) to $+0.8$ eV (all Ga). The potentials for both electrons and holes were set to $+3.0$ eV outside the particle to model the ligand shell. The lowest exciton energy for each structure was obtained as the sum of the lowest electron and hole energies. The overlap integral between the electron and hole wavefunctions was calculated numerically from the wavefunction coefficients.

With AIGS QDs having the radial composition profile shown in Figure 4.6, these calculations indicate that photoexcitation produces an electron-hole pair in which the electron is delocalized and the hole is localized to a small fraction of the particle. This suggests that the featureless absorption spectrum is due to production of holes that are localized in different parts of the particle. Specifically, a hole in the outer, gallium-rich part of the particle will have a higher energy than one produced near the center, silver-rich part of the particle. Since the electron is delocalized over the entire particle, all the localized holes have significant overlap with the lowest few electron wavefunctions and therefore have significant oscillator strength. We suggest that it is this continuum of optically accessible hole energies that results in the broad absorption spectrum. A calculated absorption spectrum can be obtained by considering transitions involving the lowest energy electrons and holes for a typical particle. Each peak in this spectrum is convolved with a Gaussian to account for inhomogeneous broadening. This crude model qualitatively reproduces the observed unstructured absorption spectrum. We suggest that in all cases, the nascent holes relax to the lowest energy states, resulting in a narrow luminescence spectrum. It is also of interest to note that the PLE spectrum closely matches the absorption spectrum (see Figure 4.2 inset). This indicates that relaxation of hot electrons and holes occurs without intervention of nonradiative processes. The change in dipole moment caused by creation of an electron-hole pair was also calculated from these structures. It is obtained as the sum over all atoms of the charge density (electron or hole) multiplied by the position. The electric field at the hole produced by the static ionic charges was calculated assuming that the charge on each ion is half its valence, and weighting the field at each atom by the hole density on that atom. While this is a crude approximation, it gives a reasonable estimate of the magnitude and variability of the internal electric fields. Further details on the calculations are provided in Reference [81].

Figure 4.7 plots the electron-hole overlap and the average electric field strength at the hole versus the relative energy of the lowest exciton for 20 different structures. The

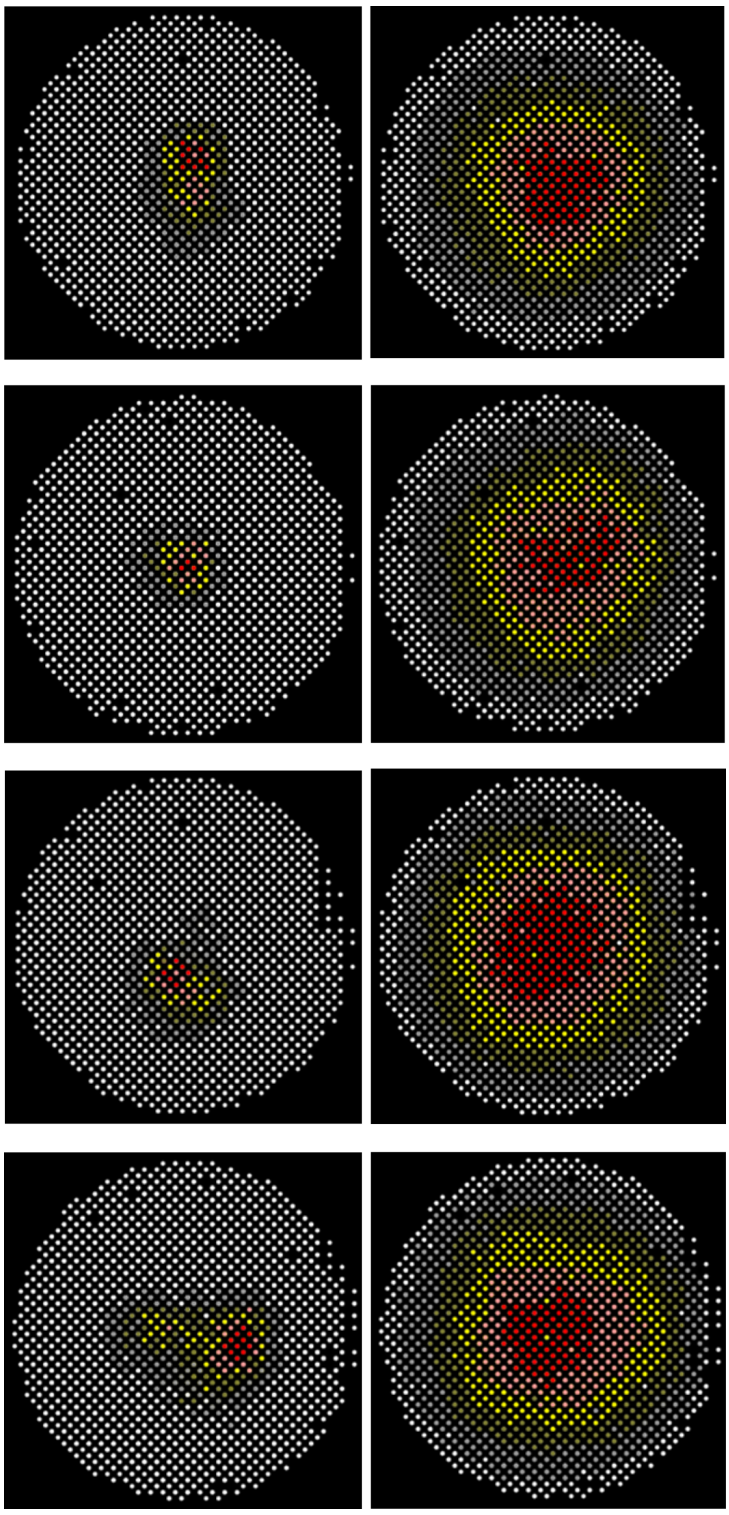


FIGURE 4.8: Hole (left) and electron (right) wavefunctions for two gradient alloy structures. Plots show a cross-section through the center of each structure. The amplitude of the wavefunction on each atom is shown, color-coded with increasing amplitude: white < gray < tan < yellow < pink < red. Graphics were prepared using VMD.13 Note that some of the tetrahedral holes are empty, resulting in gaps that can be seen in the Figure.

electron-hole overlap is somewhat correlated with exciton energy; lower exciton energies are associated with smaller overlaps. This suggests that the particles with regions of higher local Ag concentration localize the holes more effectively in regions where the hole energy is lower. However, the variation in overlap across the ensemble is not large enough by itself to explain the large variation in radiative rates found experimentally. The electric field averaged over the hole density is nearly uncorrelated with exciton energy and varies by more than a factor of three across the ensemble. Since perturbations to the local symmetry should be proportional to the square of the field, this would predict an order of magnitude difference between different particles. The absolute field strength depends on the assumed dielectric constant (taken to be 1 here) and the charges assumed for the atoms; however, the magnitude of the dispersion in field strengths across different particles arises from the randomness in the local cation environment and should be fairly independent of these details.

The calculated change in dipole moment upon excitation ranges from 12–65 D. This suggests that the exciton energy should be a weak function of solvent dielectric constant, consistent with the chloroform versus toluene shift seen in Figure 4.1. The structures used to calculate the electric fields and overlaps shown in Figure 4.7 use the average RCP shown in Figure 4.6. We note that the overall conclusions that follow from Figure 4.7 do not depend on the details of the RCP. Figures 4.8 show typical electron and hole distributions for gradient alloy and random alloy particles.

Even within the limitations of the simple effective mass approximation model, these results are not expected to give quantitative estimates of the bandgap energies for a variety of reasons addressed further in Reference [81]. However, they do suggest that inhomogeneities in both electron-hole overlap and, particularly, local electric field strengths are likely to play important roles in determining the spectroscopy and photophysics.

4.5 Inhomogeneity in Oscillator Strengths

We suggest that the large range of time constants seen in the multi-exponential PL decays is due to inhomogeneity in the radiative rates. This assignment is based on the idea that the lowest energy (band edge) transition is nominally forbidden and acquires oscillator strength through symmetry breaking of the local environment. The lowest transition is dark because of the even/odd parity of the valence band. Efros presents theory and calculations on $CuInS_2$ indicating that the parity selection rule can be broken by local crystal structure and by local electric fields.[106] Although the orbital composition of the valence band states is different,[107] the results are qualitatively applicable to AIGS particles.[106] In the absence of a tetragonal distortion, the chalcopyrite crystal structure of $CuInS_2$ or $AgInS_2$ is very similar to the cubic zincblende structure. Ref. [106] shows that in the cubic structure, parity is maintained and the lowest excited (odd) state is optically dark. It becomes allowed by a tetragonal distortion or any uniaxial perturbation. The spectroscopic manifestations of the parity-forbidden lowest transition and the allowed transition at slightly higher energy have been seen

in $CuInS_2/ZnS$ particles. In this case, there are two features in the absorption spectrum that are assigned to transitions from the even and odd valence band states. The band-edge transition gets stronger upon zinc incorporation into the crystal due to increased oscillator strength in the odd-parity transition.[108] The presence of the odd and even parity bands has also been reported in transient absorption studies.[109] In this case, transient absorption measurements reveal the signatures of the two low-lying subbands having opposite parity, and photoluminescence studies at cryogenic temperatures reveal the dark state emission.

Any perturbation that breaks the parity of the lowest state results in oscillator strength in that state. The effect of parity symmetry breaking in the local crystal structure may be very significant in a random alloy particle. However, calculation of these effects is not within the scope of this work. Local electric fields at the hole can also break parity and the values shown in Figure 4.7 indicate that the magnitude of these fields varies over a very large range. We suggest that this effect alone is sufficient to cause inhomogeneity in the extent to which the lowest transition is allowed and hence the inhomogeneity in the radiative lifetimes. We note that the wavelength dependence of the radiative lifetimes in Table 4.1 approximately follows the ν^3 dependence of the electrodynamic coupling,[93] and otherwise does not depend on the PL detection wavelength. Consistent with Table 4.1, Figure 4.7 shows that the calculated electric fields are uncorrelated with the bandgap.

Inhomogeneity in the electron/hole overlap may also contribute to the radiative lifetime inhomogeneity. However, Figure 4.7 shows that the variation in electron/hole overlap is insufficient to explain the wide range of radiative lifetimes. Figure 4.7 also shows a weak correlation of the electron/hole overlap with bandgap energy, which is contrary to the lifetimes in Table 4.1. For both these reasons, we conclude that the overlap inhomogeneity is probably not the dominant source of lifetime dispersion.

4.6 Delayed Emission Model

A delayed emission model of the PL decay kinetics can also be considered to explain the biphasic PL decay kinetics. We consider this model but think it to be unlikely for reasons discussed below. In this model, the PL decay kinetics and the wavelength dependence are understood in terms of a three-state model: the ground, band-edge (BE) and trap (T) states. The trap state may be similar to the traps discussed by Kobosko and Kamat,[110] and is assumed to have a very low oscillator strength. Thus, in this model all luminescence is assumed to come from the band-edge state. The population dynamics of these states are described by a simple set of coupled linear differential equations:

$$\frac{dT}{dt} = -k_{-1}T + k_1 BE, \qquad \frac{dBE}{dt} = k_{-1}T - (k_1 + k_{\mathrm{rad}})BE, \tag{4.3}$$

where k_1 (k_{-1}) is the trapping (de-trapping) rate constant and k_{rad} is the radiative rate constant. The PL quantum yield of these particles is close to unity, so to a good

approximation nonradiative processes to the ground state can be ignored. The low oscillator strength of the trap state results in photoexcitation populating only the band-edge state. Integration of these equations with the initial conditions $T(0) = 0$ and $BE(0) = 1$ gives a biphasic band-edge decay:

$$BE(t) = \frac{k_+ - k_{-1}}{k_+ - k_-} e^{-k_+ t} + \frac{k_{-1} - k_-}{k_+ - k_-} e^{-k_- t}, \tag{4.4}$$

where $k_\pm = k_T/2 \pm (k_T^2 - 4k_{-1}\,k_{\text{rad}})^{1/2}/2$ and $k_T = k_1 + k_{-1} + k_{\text{rad}}$. The detailed balance constraint requires $k_{-1}/k_1 = \exp(\Delta E/k_b T)$, where ΔE is the trap state energy above the band edge. This simple model gives the fast and slow decay times and relative amplitudes in terms of k_{rad}, k_1, and k_{-1}. These decay kinetics make good intuitive sense; in the limiting case in which $k_1, k_{-1} \ll k_{\text{rad}}$, the fast component corresponds to the BE and T equilibration time, and the slow component corresponds to the decay time with the equilibrium fraction in the BE state.

4.6.1 Analysis of AIGS Radiative Dynamics & Comparison with Literature

The radiative rates, trapping rates, and trap energetics in chloroform and toluene can be calculated from the fit parameters in Table 4.1 and the equations for the fast and slow decay components and their contributions. These values for different solvents and wavelengths are shown in Table 4.3, with the rates given as inverse times.

TABLE 4.3: Parameters of the shallow trap model calculated using the fit values in Table 4.1. Here τ_1 (τ_{-1}) is the trapping (de-trapping) time constants, τ_{rad} is the radiative time constant (inverse of the respective rates, k_1, k_{-1} & k_{rad}), and ΔE is the energy separation of the trap states from the band edge.

	Chloroform			Toluene		
	τ_{-1}, τ_1	τ_{rad}	ΔE	τ_{-1}, τ_1	τ_{rad}	ΔE
Blue	52 ns, 274 ns	76 ns	43 meV	54 ns, 272 ns	71 ns	42 meV
Peak	56 ns, 289 ns	80 ns	42 meV	59 ns, 264 ns	71 ns	38 meV
Red	63 ns, 317 ns	87 ns	42 meV	58 ns, 260 ns	75 ns	39 meV

Several aspects of the values in Table 4.3 are notable. The radiative rates get slower at redder detection energies, and approximately follow a ν^3 dependence, indicating that the oscillator strength is essentially unchanged across the inhomogeneous PL band. We note that the energy difference between the blue (515 nm) and red (535 nm) detection wavelengths is 90 meV. Despite this change in bandgap energy, the energy of the reservoir (trap) state with respect to the quantum-confined valence band edge is essentially constant.

The radiative dynamics data reported by Uematsu in 2018 and 2023 [111, 112] were analyzed using the delayed emission model described above. These studies report the spectroscopy of quantum dots emitting at 585 nm and 533 nm, respectively. The biexponential decay parameters extracted from both datasets are summarized in Table 4.4.

TABLE 4.4: Biexponential decay parameters for as-grown and TBP-treated quantum dots reported by Uematsu (2018[111], 2023[112]).

	As Grown			TBP Treated		
	τ_f	A_f	τ_s	τ_f	A_f	τ_s
Ref [111] (QY $\sim$ 22–56%)	52.3 ns	0.592	203.4 ns	50.5 ns	0.704	157.5 ns
Ref [112] (QY $\sim$ 58–74%)	51.5 ns	0.800	187 ns	64.8 ns	0.880	238 ns

Applying the delayed emission model to these decay parameters yields the radiative rate, trapping rate, and energetic separation between the trap states and the band edge, as reported in Table 4.5.

TABLE 4.5: Radiative and trapping parameters derived from the delayed emission model for as-grown and TBP-treated quantum dots.

	As Grown			TBP Treated		
	τ_{-1}, τ_1	τ_{rad}	ΔE	τ_{-1}, τ_1	τ_{rad}	ΔE
Uematsu 2018	93 ns, 220 ns	113 ns	22 meV	96.8 ns, 274 ns	82 ns	27 meV
Uematsu 2023	83 ns, 244 ns	116 ns	28 meV	125 ns, 238 ns	122 ns	21 meV

The same conclusion follows from the comparison of these results with those in Refs. [82, 83]. Even though the band energies of the particles are 240 meV and 35 meV below the bandedge of the AIGS particles studied in this work, the radiative rates and energy seperations obtained from the delayed emission analysis are similar to ones obtained for our samples. Thus, even in particles having significantly lower band energies the reservoir (trap) state would have to be pinned to the band edge. There is no obvious reason why this would occur. The particles discussed in those references have significantly different band gaps than ours, but exhibit very similar PL kinetics. The delayed emission model therefore requires that the trap depths are independent of changes in RCP and therefore bandgap. It is not clear how that could be the case, and this is why we do not favor this model.

4.7 Calculation of average dipole moment of the excited state

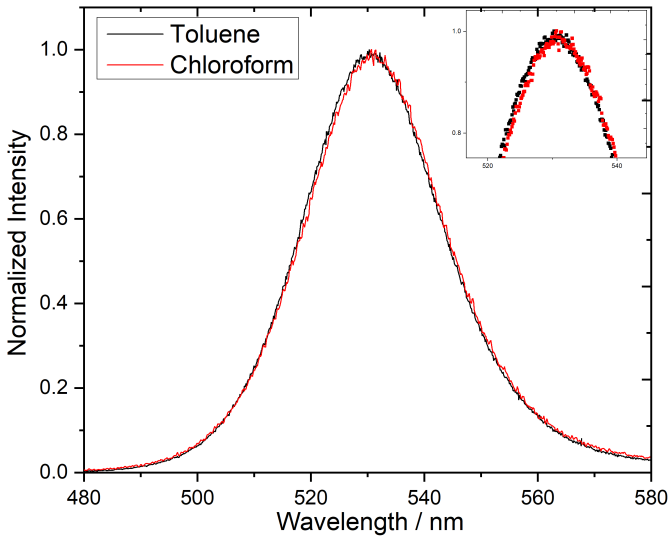


FIGURE 4.9: Emission spectra of AIGS QDs in toluene (black) and chloroform (red). The wavelength shift is about 0.6 nm.

A simple calculation of the average dipole moment (μ_{avg}) of the excited state in AIGS QDs involves considering the Onsager reaction field (R) produced in response to a dipole with a spherical volume (radius a_0) surrounded by a medium with dielectric constant ε_r.

$$R = \frac{1}{4\pi\varepsilon_0} \cdot \frac{2(\varepsilon_r - 1)}{2\varepsilon_r + 1} \cdot \frac{\mu_{\text{avg}}}{a_0^3} \tag{4.5}$$

The energy drop associated with this reaction field is given by:

$$\Delta E = R \cdot \mu_{\text{avg}} = \frac{1}{4\pi\varepsilon_0} \cdot \frac{2(\varepsilon_r - 1)}{2\varepsilon_r + 1} \cdot \frac{\mu_{\text{avg}}^2}{a_0^3} \tag{4.6}$$

A roughly 0.6 nm shift in the PL spectra centered at 530 nm produces an energy shift of about 2.7 meV. Using this energy shift, the radius of the AIGS QDs (~4.1 nm) and approximate values of the dielectric constants of chloroform and toluene (4.81 and 2.38 respectively), the average dipole moment of the excited state in these QDs is 1.2×10^{-28} C m or 35 Debye (1 Debye $= 3.3564 \times 10^{-30}$ C m).

4.8 Conclusions

The static spectroscopy and radiative dynamics of AIGS QDs are very different from what is seen in their more extensively studied II-VI and III-V analogs. In AIGS QDs, the absorption spectrum is broad and featureless, while the PL spectrum is quite sharp. The PL exhibits a long lived and nonexponential decay, having time constants ranging from 40 to 150 ns. The spectroscopy and radiative kinetics are understood in the context of the radial composition profile of each element, as determined by the analysis of EDX line profiles. These RCPs show that the core is largely Ag_2S with the fraction of gallium increasing with radial distance. As with any random alloy, there are spatial fluctuations in the local silver concentration and holes will localize at the most silver-rich regions of the particle. The sites at which holes localize have varying degrees of local crystal asymmetry and varying magnitudes of internal electric fields. This is important because of the parity-forbidden nature of the lowest transition. In the random alloy crystal environment, the parity selection rule is partially relaxed and both the local crystal asymmetry and the local electric fields can break the symmetry of the exciton's environment, mixing the even (allowed) and odd (forbidden) parity states. The varying extent to which the parity selection rule is relaxed gives rise to inhomogeneity in the radiative rates and hence the wide distribution of radiative lifetimes in the experimentally observed nonexponential PL decay kinetics.

We also consider the possibility that the nonexponential PL decay kinetics can be explained by a delayed emission model. Although this model cannot be completely ruled out, for several reasons we consider this to be less likely than the inhomogeneous radiative rate model.

5 Summary & Outlook

The central theme of this thesis is to further explore the role of surface chemistry and local field effects in colloidal quantum dot photophysics. It also demonstrates that very simple physical models can be implemented to model these properties and capture, in an intuitive way, the essence of the phenomenon.

5.0.1 Ligand Effects on the Fine Structure of CdTe QDs

Chapter 2 examined how the charge state of surface ligands perturbs the angular momentum fine structure of 3.2 nm CdTe QDs. Polarized photoluminescence excitation (PLE) spectroscopy and time-resolved photoluminescence measurements are used to extract the fine structure splitting of high-quality CdTe QD cores under varying ligand environments. This study demonstrates the core idea that surface charges play a crucial role in the photophysics of these QDs, that so far, has been largely overlooked. Charged ODPA ligation produces larger anisotropies, a larger Stokes shift (64 versus 51 meV), and a shorter radiative lifetime (23.0 versus 27.3 ns) than weakly charged octanethiol ligation. These observations point in the direction of an increased fine structure splitting and more oscillator strength into the weakly allowed lower $\pm 1^L$ state. The near-complete reversibility demonstrated by the restoration of the optical spectra upon reversal to charged ligation rules out etching or ripening artifacts.

The most significant result of this chapter is the quantitative failure of the standard model. No single pair of exchange energy (η) and light-heavy hole splitting (Δ) simultaneously account for the measured anisotropies and radiative lifetimes. Physically reasonable η values predict lifetimes that are about a factor of three too long, while very small η values reproduce the measured lifetimes but make the calculated observables almost completely insensitive to Δ, contrary to the ligand dependence found experimentally. The standard model considers only oblate/prolate perturbations (Y_{20} type perturbation), which maintain the x, y degeneracy. In contrast, the electric fields produced by discrete charged ligands on crystal facets contain other lower symmetry components. These perturbations mix all of the fine structure states, and oscillator strengths in ways that the two-parameter model cannot describe.

5.0.2 Surface Stoichiometry and the Continuum

Chapter 3 addressed the chemical origins of the broad, featureless continuum absorption underlying the discrete excitonic transitions and, in some cases, extends to energies below the lowest quantum confined exciton. The surfaces of 3.2 nm CdTe QDs were systematically converted from cadmium-rich to tellurium-rich, to demonstrate that the

continuum consists of two physically distinct contributions. The low-energy continuum, which overlaps the region between the $1S_e$-$1S_h$ and $1S_e$-$2S_h$ excitons, increases strongly with surface tellurium content and decreases upon cadmium passivation. It is assigned to transitions from occupied surface chalcogenide dangling-bond levels near the valence band edge into quantum-confined conduction band states. In contrast, the high-energy ($\sim$3.5 eV) continuum is nearly insensitive to surface treatment and scales with particle volume, consistent with its conventional assignment to bulk-like transitions.

A simple electron tunneling model explains material dependent variations in the low-energy continuum particularly in Se-capped ZnSe reported by Lin *et al.* [113]. The electron tunneling mode along with thermochemical estimates of the metal-chalcogenide bond energies further provides with a framework to understand this complex phenomenon. We also find that the same framework applies to surface ligand based dangling bonds. Octanethiol ligation also introduces a reversible continuum contribution with an onset of about 200 meV, demonstrating a parallel to the surface chalcogenide-based continuum.

5.0.3 Photophysics of AIGS Quantum Dots

Chapter 4 examined the complex photophysics and dynamics of $AgIn_xGa_{1-x}S_2$ QDs. These particles have a broad, featureless absorption spectrum, narrow ($\sim$30 nm) band-edge emission, high quantum yield ($\sim$90%) and multiphasic exponential PL decays with components ranging from about 40 to 150 ns. The high PLQY rules out the conventional explanation of multiexponential decays in terms of the contributions from recombination of quantum confined e-h pairs and recombinations with-in donor-acceptor pair.

This chapter demonstrated the use of averaged EDX linescans to produce a more informative radial composition profile (RCP). This RCP can then be used to construct Monte Carlo atomistic structures. Effective mass wavefunction calculations on these structures reveal that the holes localize at randomly located silver-rich regions, while the electrons remain delocalized in the QD. This produces large excited-state dipoles (12–65 D), consistent with the observed solvent-dependent PL shift and the PLE anisotropy, and internal electric fields at the hole that result in local symmetry breaking allowing the lower dark states to varying amounts resulting in multiphasic decay.

5.1 Outlook & Future Directions

The work outlined in this thesis has significance to future and published work in the field to probe the fine structure of colloidal quantum dots. Specifically, the method developed in Chapter 2, where in surface charges are demonstrated as a means to measurably tune the fine structure. This allows for the testing of the 'Efros' model demonstrating the need for lower symmetry perturbations to attain quantitative agreement with the data. This also gives an independent probe for the fine structure of the upper

manifold, revealing that the upper manifold has a 20 meV splitting (in 3.2 nm dots), which is significantly larger than the 6 meV splitting measured in the lower manifold via temperature-dependent dependence radiative decay measurements reported earlier. The addition of a lower symmetry term (Y_{1m}) could break x,y symmetry and cause the fine structure splitting in the lower state (between ± 2 and + 1^L or - 1^L) from the 20 meV reported in the PLE data set to somewhat closer to ones expected from the temperature dependent decay data, making the two sets of measurements consistent with the theoretical model. Although this may not be of direct significance to single particle measurements, it might be of value for a general understanding of the fine structure levels and its complexity for peak assignment purposes.

While the work in Chapter 3 is not a quantitative analysis of the photophysics of quantum dots and the underlying electronic structure, it is an incredibly important assignment to so far overlooked transitions in the vicinity of the lowest excitonic states. These transitions are important from the stand point of tuning the extinction coefficients of these dots, and particularly can be of consequence when looking the excited excitonic states where these transitions have significant contributions and given that they are unpolarized, it is important to account for their presence in any polarized spectroscopy.

Chapter 4 presents the photophysics of quaternary alloyed QDs in terms of the inhomogeneities of the ion distributions and brings to the center the ideas of symmetry breaking in these systems and their role in dictating the radiative dynamics. The larger work also demonstrates how EDX scans can be used to make informative radial composition profiles that can inform on the random distributions that underlie these averaged scans via Monte Carlo calculations.

The next subsections discuss future directions that can be pursued in each of these projects to improve the modeling, understand these phenomena quantitatively and probe these systems further to come to more precise answers to the source of these properties.

5.1.1 Quantifying Ligand Fields

On the theory side the next step is a fine structure model that includes lower symmetry perturbations, extending the two paremeter model by Efros *et al.*. It is not clear at this point as to how this generalization should be pursued and which Y_{lm} components to focus on. On the experimental side, temperature-dependent lifetime measurements down to cryogenic temperatures would be helpful in an independent measurement of the lowest emitting state and dark state splitting. The observation that particles synthesized at higher nucleation temperatures show smaller ligand exchange effects suggests facet-dependent ligand densities, which could be tested by correlating the spectroscopy with high-resolution (HR)-TEM and ligand NMR measurements.

5.1.2 A More Quantitative Study of the Continuum

A direct measurement of surface stoichiometry through XPS or ICP could help bolster the claims presented here. On the theoretical side, the tunneling model used here is deliberately simple, and atomistic calculations such as DFT on realistic reconstructed surfaces could address the energetic distribution of the surface dangling-bond states. The facet dependence of the continuum can also be studied via HR-TEM and ligand-NMR based approach.

5.1.3 Engineering Disorder in Ternary Quantum Dots

A temperature dependent radiative dynamics study could shed more light on the relevant fine structure levels in these systems. Synthesis strategies that control the cation ordering, such as annealing or slower growth, should narrow the distribution and push the decays toward single-exponential kinetics.

A Synthesis & Ligand Exchange of CdTe Dots

Chemicals

Chloroform, toluene and acetonitrile were obtained from Sigma-Aldrich (ACS grade) and were dried by distilling with P_2O_5. Octanethiol (97%), octadecene (ODE, 90%), oleic acid (OA, 90%), cadmium acetate dihydrate ($CdAc_2{\cdot}2H_2O$, >98%), cadmium oxide (CdO, 99.99%), tellurium (99.8%), and tri-octyl phosphine (TOP, 90%) were also obtained from Sigma-Aldrich. Stearic acid (90%) was obtained from Alfa Aesar and recrystallized in anhydrous toluene before use. Octadecyl phosphonic acid (ODPA) was obtained from PCI Synthesis. The ODPA is washed with cold deionized water, followed by washing with acetonitrile and drying under vacuum in a Büchner funnel. It is then recrystallized from anhydrous toluene and stored under nitrogen.

Synthesis of $Cd(ODPA)_2$

The $Cd(ODPA)_2$ is produced by adding 0.2 mmol CdO (25.6 mg), 0.45 mmol ODPA (135 mg) and 3.5 mL ODE under vacuum at 120 °C for 30 min to remove water from all the reactants. The mixture is then heated to 260 °C in a three-neck flask under nitrogen until the solution turns transparent, then cooled to 120 °C and evacuated for 20 min.

Synthesis of CdTe Quantum Dots (with oleic acid)

CdTe QDs were synthesized by adapting the procedure in Gong *et al.*[25] where a mixture of 0.2 mmol CdO (25.6 mg), 3.2 mmol oleic acid (1 mL), 0.15 mmol ODPA (45 mg) and 3.5 mL ODE in a three-neck flask was degassed at 100 °C and then heated to 300 °C until the solution turns transparent. The solution is degassed again at 100 °C and heated to 275 °C, at which point 0.5 mL of tellurium precursor is injected and allowed to grow for 7 minutes. The solution is then rapidly cooled to produce particles with a $1S$–$1S$ absorption peak at ∼565–570 nm. The tellurium precursor is produced by dissolving 6 mmol tellurium powder (768 mg) and 19 mmol TOP (9 mL) in 30 mL ODE, stirred at 80 °C for 3–4 hours to produce a yellow solution. This solution is centrifuged to remove any tellurium oxide. The supernatant is stored in the glovebox.

Synthesis of CdTe Quantum Dots (with stearic acid)

A mixture of 0.2 mmol $Cd(Ac)_2$ (53.3 mg), 0.8 mmol stearic acid (230 mg), 0.17 mmol ODPA (57 mg) and 4.5 mL ODE in a three-neck flask was degassed at 150 °C and then

heated to 270 °C until clear, followed by degassing at 150 °C. The Te-precursor (0.5 mL) is injected at 285 °C and growth occurs at 260–255 °C for 6–7 min. The solution is then rapidly cooled to produce particles with a 1*S*–1*S* absorption peak at ∼560–565 nm and a PLQY of 80–90%. For ease of solubility, 1 mL of the reaction mixture is diluted in 1 mL anhydrous toluene and 0.5 mL oleic acid and heated to 130 °C to perform a ligand exchange. The resulting oleic acid-capped particles have a PLQY of 75–80%.

Purification of ODPA-Ligated Particles

The purification process is a modification of the one described in Yang *et al.*[114] In the process used here, 0.5 mL of the reaction mixture is dissolved in 0.5 mL anhydrous chloroform and 20 μL oleic acid. 0.5 mL anhydrous acetonitrile is added at 60 °C and the mixture is centrifuged. The supernatant is removed and the particles are redissolved in 1 mL 1:1 (v/v) toluene/ODE. 150 μL $Cd(ODPA)_2$ is added and heated to 120 °C under nitrogen for 1 hour to produce ODPA-ligated particles with PLQY of 70–80%. ODE is added to increase the viscosity of the solution and ensure rotational diffusion effects are negligible.

Ligand Exchange to Octanethiol

0.5 mL of the reaction mixture is dissolved in 0.5 mL anhydrous chloroform and 20 μL octanethiol and heated to 60 °C. After cooling, 0.5 mL anhydrous acetonitrile is injected, the mixture is centrifuged, and the supernatant is drawn off. The precipitated particles are redissolved in 1 mL (1:1, v/v) toluene/ODE with 20 μL octanethiol and heated to 110 °C under nitrogen for 1 hour, producing octanethiol-ligated particles with PLQY of ∼60%.

Ligand Exchange to Oleic Acid

0.5 mL of the reaction mixture is dissolved in 0.5 mL anhydrous chloroform and 20 μL oleic acid and heated to 60 °C. After cooling, 0.5 mL anhydrous acetonitrile is injected, the mixture is centrifuged, and the supernatant is drawn off. The precipitated particles are redissolved in 1 mL (1:1, v/v) toluene/ODE with 0.2 mL oleic acid and heated to 130 °C under nitrogen for 1 hour, producing oleic acid-ligated particles with PLQY of ∼40%.

Reverse (Octanethiol to ODPA) Ligand Exchange

Reverse ligand exchange is accomplished by adding 20 μL ODPA solution to octanethiol-ligated particles dissolved in 1 mL (1:1, v/v) toluene/ODE and heating to 110 °C for 1 hour, producing ODPA-ligated particles with PLQY of 50–60%. The ODPA solution is produced by dissolving 50 mg ODPA in 5 mL ODE maintained at 80 °C.

B CdTe Synthesis & Surface Treatment

Chemicals.

Chloroform, toluene and acetonitrile were obtained from Sigma-Aldrich (ACS grade) and were dried by distilling with P_2O_5. Octanethiol (97%), octadecene (ODE, 90%), oleic acid (OA, 90%), cadmium acetate dihydrate ($CdAc_2 \cdot 2H_2O$, >98%), tellurium (99.8%), and tri-octyl phosphine (TOP, 90%) were also obtained from Sigma-Aldrich. Stearic acid (90%) was obtained from Alfa Aesar, and it is recrystallized in anhydrous toluene before use. Octadecyl phosphonic acid (ODPA) was obtained from PCI synthesis. The ODPA is washed with cold deionized water, followed by washing with acetonitrile and drying under vacuum in a Buchner funnel. The dried ODPA powder is dissolved in anhydrous toluene under nitrogen at 80 °C. The solution is put in an ice bath to recrystallize and then dried further under vacuum in a Buchner funnel. The dried recrystallized ODPA is stored under nitrogen.

Synthesis of $Cd(St)_2$.

The cadmium stearate ($Cd(St)_2$) is produced by adding 0.2 mmol of cadmium acetate (53.3 mg) and 0.4 mmol stearic acid (115 mg) to 5 mL octadecene (ODE). The mixture is put under vacuum at 120 °C for 30 mins to remove water from all the reactants. It is then heated to 260 °C in a three-neck flask under nitrogen until the solution turns transparent, cooled to 120 °C and put under vacuum for 20 mins.

Synthesis of CdTe dots (with oleic acid).

CdTe QDs were synthesized by adapting the procedure in Gong *et al.*[25] where a mixture of 0.2 mmol CdO (25.6 mg), 3.2 mmol oleic acid (1 mL), 0.15 mmol octadecylphosphonic acid (45 mg) and 3.5 mL octadecene (ODE) in a three-neck flask was degassed at 100 °C and then heated to 300 °C until the solution turns transparent. The solution is degassed again at 100 °C and heated to 275 °C at which point 0.5 ml of tellurium precursor is injected into the solution and allowed to grow for 7 minutes. The solution is then rapidly cooled to produce particles with 1S-1S absorption peak at ∼565-570 nm. The tellurium precursor is produced by dissolving 6 mmol tellurium powder (768 mg) and 19 mmol TOP (9 mL) in 30 mL ODE is stirred at 80 °C for 3-4 hours to produce a yellow solution. This solution is centrifuged thoroughly to remove any tellurium oxide present in the solution. The supernatant is syringed out and stored in the glovebox.

Treatment with 1:1 TOPTe.

1 mmol Te-powder is stirred with 0.5 ml TOP in 2.5 mL ODE for 24 hrs. The solution was centrifuged to remove any excess tellurium or tellurium oxide. A 0.15 mL volume of 1:1 TOPTe is added to 0.5 ml of purified sample in 2 ml ODE under nitrogen and heated to 155-160 °C for 30 mins.

Purification of particles.

The purification process is a modification of the one described in Yang *et al.*.[114] In the present case, 0.5 ml of the reaction mixture is dissolved in 0.5 mL anhydrous chloroform. 0.5 mL anhydrous acetonitrile is added to this solution at 60 °C and centrifuged. The supernatant is removed and the particles are redissolved in 3 mL 1:2 (v/v) toluene/ODE. This produces ODPA ligated particles with a photoluminescence quantum yield (PLQY) of 70%-80%.

Ligand exchange to octanethiol.

The purification and ligand exchange process used here is also a modification of the one used in reference 6. In this case, 0.5 ml of the reaction mixture is dissolved in 0.5 ml anhydrous chloroform and 20 μL octanethiol and heated to 60 °C. After cooling, 0.5 ml anhydrous acetonitrile injected, the mixture is centrifuged and the supernatant is drawn off. The precipitated particles are redissolved in 1 ml (1:1, v/v) toluene/ODE and 20 μL octanethiol and heated to 110 °C under nitrogen for 1 hour to produce octanethiol ligated particles with PLQY of $\sim$60%.

Ligand exchange to oleic acid.

The purification and ligand exchange process used here is a different modification of the one used in reference 6. In this case, 0.5 ml of the reaction octanethiol ligated sample is dissolved in 0.5 ml anhydrous chloroform and 20 μL oleic acid and heated to 60 °C. After cooling, 0.5 ml anhydrous acetonitrile injected, the mixture is centrifuged and the supernatant is drawn off. The precipitated particles are redissolved in 1 ml (1:1, v/v) toluene/ODE and 0.2 mL oleic acid and heated to 130 °C under nitrogen for 1 hour to produce oleic acid ligated particles with PLQY of $\sim$40%.

Ligand exchange to oleic acid (with cadmium oleate).

The purification and ligand exchange process used here is a different modification of the one used in reference 6. In this case, 0.5 ml of the octanethiol ligated sample is dissolved in 0.5 ml anhydrous chloroform and 20 μL cadmium oleate and heated to 60 °C. After cooling, 0.5 ml anhydrous acetonitrile injected, the mixture is centrifuged and the supernatant is drawn off. The precipitated particles are redissolved in 1 ml (1:1, v/v) toluene/ODE and 0.2 mL cadmium oleate and heated to 130 °C under nitrogen for 1 hour to produce oleic acid ligated particles with PLQY of $\sim$50%.

UV-VIS PL and absorption spectroscopy.

The polarization-resolved photoluminescence excitation (PLE) and static luminescence spectra were measured on a Jobin-Yvon Fluorolog 3. The static absorption spectra were measured using a Cary 50 UV-vis spectrophotometer. All UV-VIS spectroscopy was performed on $\sim$50 μL of the sample dissolved in 4 mL of toluene or chloroform in a 1 cm path length cuvette with concentrations that produce 400 nm absorbances of 0.15 – 0.19.

Vibrational spectroscopy.

All IR spectra were obtained in attenuated total reflectance (ATR) mode on a Vertex 70 (Bruker) FTIR spectrometer, operating with a diamond ATR accessory. The ATR mode allows measurements of the vibrational signal from the evanescent field and minimizes noise from the water background. The Bruker OPUS 7.5 software for Windows was used for instrument management and spectra acquisition. The instrument was operated at a resolution of ± 4 cm^{-1}.

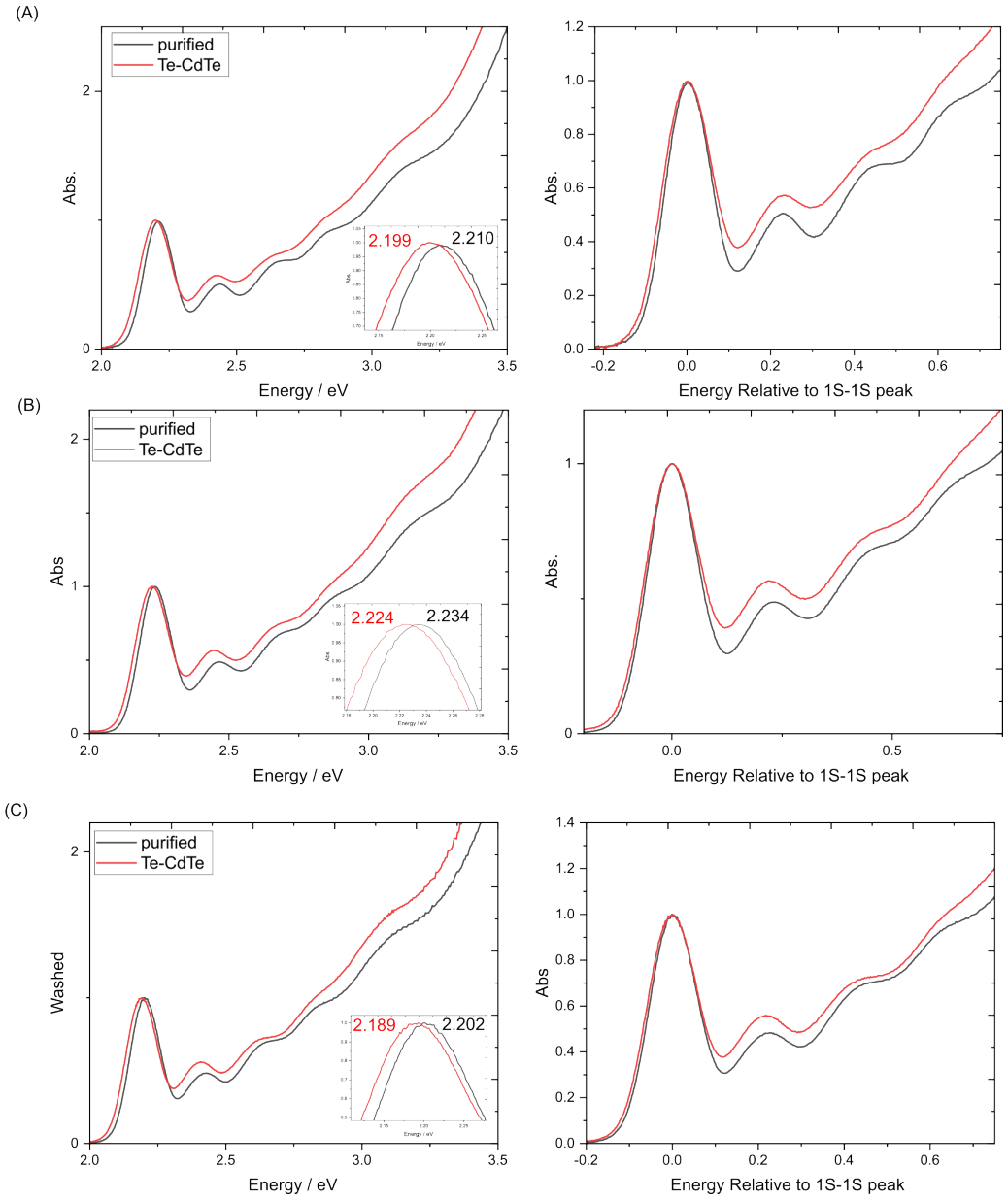


FIGURE B.1: (A-C) Shows example absorption spectra of the purified (black) and Te-CdTe (red) QD samples of 3.3-3.4 nm in diameter. The Te-capped particles are obtained via treatments similar to ones described above.

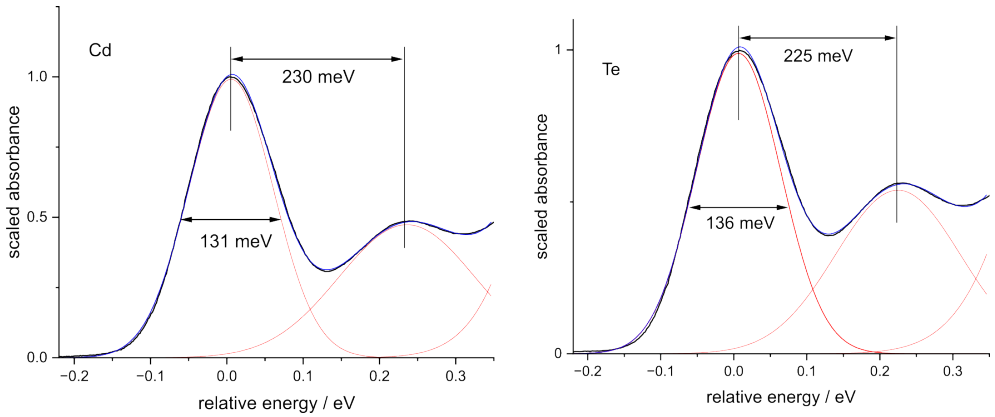


FIGURE B.2: The lowest energy region of the Cd-rich and Te-rich QD absorption spectra are fitted to a sum of three Gaussians. The absorption spectra are indicated in black, the contributing Gaussians in red and the fitted sum peaks in blue. The highest energy fitting peaks contain contributions from both quantum confined transitions and the low energy continuum. The widths (fwhm) of the lowest energy Cd-rich and Te-rich peaks are 131and 136 meV, as indicated. Making the surface Te rich slightly decreases the 2S-1S splitting by 5 meV, from 230 to 225 meV. The statistical error in this fitting ± 2 meV, so this difference is very small, but statistically significant

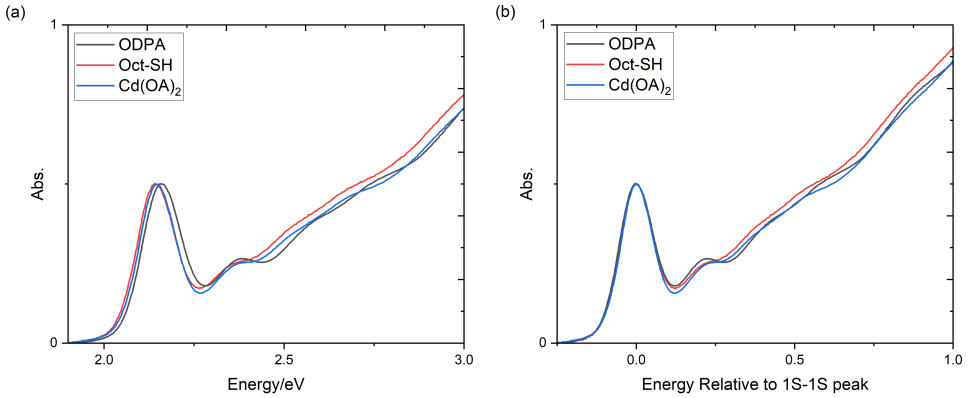


FIGURE B.3: (a) Absorption spectra of CdTe QDs ligated with ODPA (black), octanethiol (red) and oleic acid (cadmium oleate treated) (blue). (b) The same ODPA and octanethiol spectra as in (a), except plotted as a function of energy from the lowest exciton peak.

C Herzberg Teller Coupling

The transition from $|2, \pm 2\rangle$ state to ground state is angular momentum forbidden and can become weakly allowed if the wavefunction is deformed by a vibrational mode. The coupling of different transition dipoles via the deformation of the Hamiltonian is described by Herzberg-Teller (HT) coupling [37]. The transition dipole can be between an initial state (Ψ_i) and a final state (Ψ_i) can be rewritten:

$$\langle \Psi_f(Q) | \mu | \Psi_i(Q) \rangle = M_{if}(Q) = M_{if}(Q_0) + \sum_{j \neq f} \sum_k \left\langle f \left| \frac{\partial H_e}{\partial Q_k} Q_k \right| j \right\rangle \frac{M_{ji}}{E_f - E_j} \tag{C.1}$$

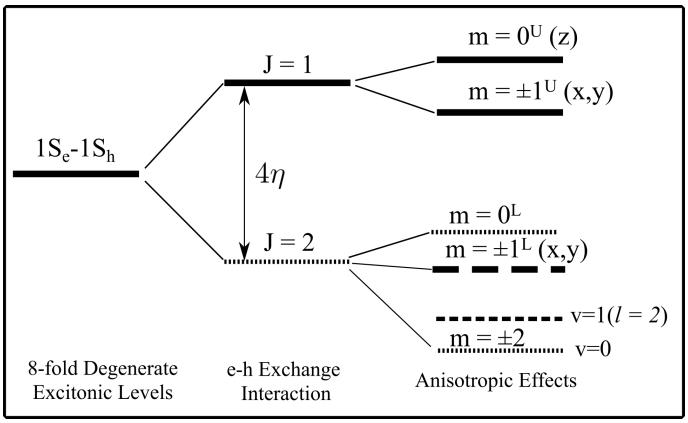


FIGURE C.1: The electronic fine structure of the $1S_e - 1S_h$ transition showing the e-h exchange splitting and effects of anisotropies in the nanocrystals

The $\frac{\partial H_e}{\partial Q_k}$ term has the same symmetry as the vibration mode Q_k, therefore the term $\langle \Psi_j | \frac{\partial H_e}{\partial Q_k} | \Psi_i \rangle$ is non-zero if the direct product of the representation of Ψ_j, Ψ_i and Q_k contains a totally symmetric representation. In the case of the ± 2 states, the oscillator strength of a phonon copy of the state ($f_{2,ph}$) can be written in terms of the oscillator strengths of the bright states in the $1S_e - 1S_h$ transition manifold.

$$\begin{aligned} f_{2,ph} = \sum_k \left\langle 1L \left| \frac{\partial H_e}{\partial Q_k} Q_k \right| 2 \right\rangle \frac{f_{1L}}{E_{1L} - E_2 - E_{Q_k}} + \sum_k \left\langle 1U \left| \frac{\partial H_e}{\partial Q_k} Q_k \right| 2 \right\rangle \frac{f_{1U}}{E_{1U} - E_2 - E_{Q_k}} \\ + \sum_k \left\langle 0U \left| \frac{\partial H_e}{\partial Q_k} Q_k \right| 2 \right\rangle \frac{f_{0U}}{E_{0U} - E_2 - E_{Q_k}} \end{aligned} \tag{C.2}$$

$$Q_{lm}(r,t) = j_l(kr)Y_{lm}(\theta,\phi) \tag{C.3}$$

Here, $k = \frac{\omega}{V_T}$ is the wave vector corresponding to the vibrational mode Q_k. We consider the lowest energy acoustic phonons (l=2) as a means to mix the ± 2 states with the other bright states. The HT coupling terms can be calculated in terms of the contraction of the spherical harmonic corresponding to the two electronic states and the phonon mode.

$$\iint Y^*_{l_1m_1}(\Omega)Y_{l_2m_2}(\Omega)Y_{l_3m_3}(\Omega)d\Omega = \sqrt{\frac{(2l_1+1)(2l_2+1)}{4\pi(2l_3+1)}}\begin{pmatrix} l_1 & l_2 & l_3 \\ m_1 & m_2 & m_3 \end{pmatrix}\begin{pmatrix} l_1 & l_2 & l_3 \\ 0 & 0 & 0 \end{pmatrix} \tag{C.4}$$

The HT-coupling terms between the ± 2 states and the other bright states are given by:

$$\begin{aligned}
\left\langle \pm 1L \left| \frac{\partial H_e}{\partial Q_k} Q_k \right| \pm 2 \right\rangle &= \chi \frac{C^-}{4\pi\sqrt{6}} \iint Y^*_{10}(\Omega)Y_{2m}(\Omega)Y_{1\pm1}(\Omega)d\Omega \\
&= \chi \frac{C^-}{4\pi\sqrt{6}} \sqrt{\frac{5}{4\pi}} \begin{pmatrix} 1 & 2 & 1 \\ 0 & m & \pm 1 \end{pmatrix}\begin{pmatrix} 1 & 2 & 1 \\ 0 & 0 & 0 \end{pmatrix} \\
&= \chi \frac{C^-}{8\sqrt{10}\pi^{3/2}}, \quad m = \pm 1 \\
\left\langle \pm 1U \left| \frac{\partial H_e}{\partial Q_k} Q_k \right| \pm 2 \right\rangle &= \chi \frac{C^+}{4\pi\sqrt{6}} \iint Y^*_{10}(\Omega)Y_{2m}(\Omega)Y_{1\pm1}(\Omega)d\Omega \\
&= \chi \frac{C^+}{4\pi\sqrt{6}} \sqrt{\frac{5}{4\pi}} \begin{pmatrix} 1 & 2 & 1 \\ 0 & m & \pm 1 \end{pmatrix}\begin{pmatrix} 1 & 2 & 1 \\ 0 & 0 & 0 \end{pmatrix} \\
&= \chi \frac{C^+}{8\sqrt{10}\pi^{3/2}}, \quad m = \pm 1 \\
\left\langle 0U \left| \frac{\partial H_e}{\partial Q_k} Q_k \right| \pm 2 \right\rangle &= \chi \frac{1}{8\pi\sqrt{6}} \iint Y^*_{1\mp1}(\Omega)Y_{2m}(\Omega)Y_{1\pm1}(\Omega)d\Omega \\
&= \chi \frac{1}{8\pi\sqrt{6}} \sqrt{\frac{5}{4\pi}} \begin{pmatrix} 1 & 2 & 1 \\ \mp 1 & m & \pm 1 \end{pmatrix}\begin{pmatrix} 1 & 2 & 1 \\ 0 & 0 & 0 \end{pmatrix} \\
&= \chi \frac{1}{16\sqrt{5}\pi^{3/2}}, \quad m = \pm 2
\end{aligned} \tag{C.5}$$

Here, $\chi = \frac{2}{a}\int Sin^2(\pi r/a)[R_0(r) + R_2(r)]^2 j_2(kr)\left(\frac{\partial H}{\partial Q_2}\right)dr$ and the other HT-coupling terms between $+2$ and $-1L/-1U/0U$ states are zero due to the spin part of the wave function. The oscillator strengths of ± 2 level is given as:

$$\begin{aligned}
f_{\pm 2,ph} = \frac{C^-}{8\sqrt{10}\pi^{3/2}} \frac{\chi f_{1L}}{E_2 - E_{1L} - E_{ph}} + \frac{C^+}{8\sqrt{10}\pi^{3/2}} \frac{\chi f_{1U}}{E_2 - E_{1U} - E_{ph}} \\
+ \frac{1}{16\sqrt{5}\pi^{3/2}} \frac{\chi f_{0U}}{E_2 - E_{0U} - E_{ph}}
\end{aligned} \tag{C.6}$$

The polarization of the resulting transition would depend on the proportion of the oscillator strength coming from the xy-polarized $\pm 1U/L$ states and the z-polarized $0U$ state. We define a quantity ρ as a ratio of the contribution of oscillator strengths coming from $\pm 1^{U/L}$ and 0^{U} states.

$$\begin{aligned}\rho &= \frac{C^-}{8\sqrt{10}\pi^{3/2}}\frac{\chi f_{1L}}{E_2 - E_{1L} - E_{ph}} + \frac{C^+}{8\sqrt{10}\pi^{3/2}}\frac{\chi f_{1U}}{E_2 - E_{1U} - E_{ph}}\frac{16\sqrt{5}\pi^{3/2}}{1}\frac{E_2 - E_{0U} - E_{ph}}{\chi f_{0U}} \\ &= \sqrt{2}(E_2 - E_{0U} - E_{ph})\left[\frac{C^- f_{1L}/f_{0U}}{E_2 - E_{1L} - E_{ph}} + \frac{C^+ f_{1U}/f_{0U}}{E_2 - E_{1U} - E_{ph}}\right]\end{aligned} \tag{C.7}$$

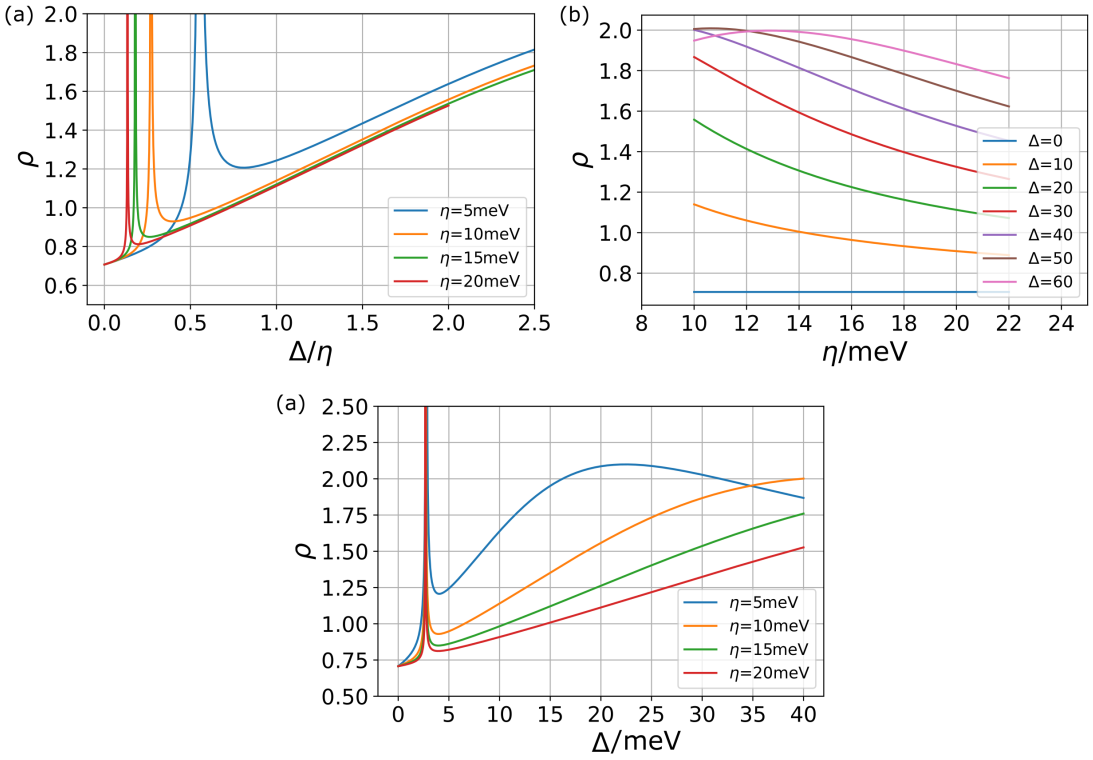


FIGURE C.2: Shows the depolarization ratio (ρ) as a function of (a) Δ/η (b) η and (c) Δ

The energy of the $l = 2$ spherical phonon mode (E_{ph}) in CdSe is roughly $2meV$. All other quantities are defined in terms of η and Δ in equations (1.14), (1.15) and (1.12). C.2 shows $\rho_{xy,z}$ as a function of Δ and for various η. For a fully spherical dot ($\Delta = 0$), the depolarization ratio is 0.71. This is a downstream effect of their corresponding Wigner-3j symbols being different. The resonance feature in the polarizability (in C.2(a)) arises from the fact that at certain small values of Δ, the phonon level becomes resonant with the $\pm 1L$ state around which point the denominator of the first term in Equation (C.7) blows up.

References

[1] J. Yang, D. Hahm, K. Kim, S. Rhee, M. Lee, S. Kim, J. H. Chang, H. W. Park, J. Lim, M. Lee, H. Kim, J. Bang, H. Ahn, J. H. Cho, J. Kwak, B. Kim, C. Lee, W. K. Bae, and M. S. Kang, "High-resolution patterning of colloidal quantum dots via non-destructive, light-driven ligand crosslinking", Nat Commun **11**, 2874 (2020).

[2] Y. Jiang, S.-Y. Cho, and M. Shim, "Light-emitting diodes of colloidal quantum dots and nanorod heterostructures for future emissive displays", J. Mater. Chem. C **6**, 2618 (2018).

[3] B. le Feber, F. Prins, E. De Leo, F. T. Rabouw, and D. J. Norris, "Colloidal-Quantum-Dot Ring Lasers with Active Color Control", Nano Lett. **18**, 1028 (2018).

[4] H. Jung, N. Ahn, and V. I. Klimov, "Prospects and challenges of colloidal quantum dot laser diodes", Nat. Photon. **15**, 643 (2021).

[5] J. Song, Y. Zhang, Y. Dai, J. Hu, L. Zhu, X. Xu, Y. Yu, H. Li, B. Yao, and H. Zhou, "Polyelectrolyte-Mediated Nontoxic AgGaxIn1–xS2 QDs/Low-Density Lipoprotein Nanoprobe for Selective 3D Fluorescence Imaging of Cancer Stem Cells", ACS Appl. Mater. Interfaces **11**, 9884 (2019).

[6] L. Fu, K. Fu, X. Gao, S. Dong, B. Zhang, S. Fu, H.-Y. Hsu, and G. Zou, "Enhanced Near-Infrared Electrochemiluminescence from Trinary Ag–In–S to Multinary Ag–Ga–In–S Nanocrystals via Doping-in-Growth and Its Immunosensing Applications", Anal. Chem. **93**, 2160 (2021).

[7] C. R. Kagan, L. C. Bassett, C. B. Murray, and S. M. Thompson, "Colloidal Quantum Dots as Platforms for Quantum Information Science", Chem. Rev. **121**, 3186 (2021).

[8] A. E. K. Kaplan, C. J. Krajewska, A. H. Proppe, W. Sun, T. Sverko, D. B. Berkinsky, H. Utzat, and M. G. Bawendi, "Hong–Ou–Mandel interference in colloidal CsPbBr3 perovskite nanocrystals", Nat. Photon. **17**, 775 (2023).

[9] S. M. Thompson, C. Şahin, S. Yang, M. E. Flatté, C. B. Murray, L. C. Bassett, and C. R. Kagan, "Red Emission from Copper-Vacancy Color Centers in Zinc Sulfide Colloidal Nanocrystals", ACS Nano **17**, 5963 (2023).

[10] J. Almutlaq, Y. Liu, W. J. Mir, R. P. Sabatini, D. Englund, O. M. Bakr, and E. H. Sargent, "Engineering colloidal semiconductor nanocrystals for quantum information processing", Nat. Nanotechnol., 1 (2024).

[11] M. J. J. Mangnus, J. W. de Wit, S. J. W. Vonk, J. J. Geuchies, W. Albrecht, S. Bals, A. J. Houtepen, and F. T. Rabouw, "High-Throughput Characterization of Single-Quantum-Dot Emission Spectra and Spectral Diffusion by Multiparticle Spectroscopy", ACS Photonics **10**, 2688 (2023).

[12] E. Prin, C. Xia, Y.-H. Won, E. Jang, S. V. Goupalov, P. Tamarat, and B. Lounis, "Revealing the Band-Edge Exciton Fine Structure of Single InP Nanocrystals", Nano Lett. **23**, 6067 (2023).

[13] L. Biadala, B. Siebers, Y. Beyazit, M. D. Tessier, D. Dupont, Z. Hens, D. R. Yakovlev, and M. Bayer, "Band-Edge Exciton Fine Structure and Recombination Dynamics in InP/ZnS Colloidal Nanocrystals", ACS Nano **10**, 3356 (2016).

[14] D. B. Berkinsky, A. H. Proppe, H. Utzat, C. J. Krajewska, W. Sun, T. Šverko, J. J. Yoo, H. Chung, Y.-H. Won, T. Kim, E. Jang, and M. G. Bawendi, "Narrow Intrinsic Line Widths and Electron–Phonon Coupling of InP Colloidal Quantum Dots", ACS Nano **17**, 3598 (2023).

[15] S. Liu, Y. Shu, M. Zhu, H. Qin, and X. Peng, "Anomalous Emission Shift of CdSe/CdS/ZnS Quantum Dots at Cryogenic Temperatures", Nano Lett. **22**, 3011 (2022).

[16] D. F. Kelley, "Angular Momentum Fine Structure in InP/ZnSe Quantum Dots", J. Phys. Chem. Lett. **15**, 6279 (2024).

[17] A. L. Efros, M. Rosen, M. Kuno, M. Nirmal, D. J. Norris, and M. Bawendi, "Band-edge exciton in quantum dots of semiconductors with a degenerate valence band: Dark and bright exciton states", Phys. Rev. B **54**, 4843 (1996).

[18] E. P. Warekois, M. C. Lavine, A. N. Mariano, and H. C. Gatos, "Crystallographic polarity in the ii-vi compounds", J Appl. Phys. **33**, 690 (1962).

[19] P. YU and M. Cardona, *Fundamentals of Semiconductors: Physics and Materials Properties* (Springer Science & Business Media, Apr. 2010).

[20] M. Cardona, N. E. Christensen, and G. Fasol, "Relativistic band structure and spin-orbit splitting of zinc-blende-type semiconductors", Phys. Rev. B **38**, 1806 (1988).

[21] W. Feng, D. Xiao, Y. Zhang, and Y. Yao, "Half-Heusler topological insulators: A first-principles study with the Tran-Blaha modified Becke-Johnson density functional", Phys. Rev. B **82**, 235121 (2010).

[22] L. E. Brus, "Electron–electron and electron-hole interactions in small semiconductor crystallites: The size dependence of the lowest excited electronic state", J. Chem. Phys. **80**, 4403 (1984).

[23] P. Cavanaugh, X. Wang, M. J. Bautista, I. Jen-La Plante, and D. F. Kelley, "Spectral widths and Stokes shifts in InP-based quantum dots", J. Chem. Phys. **159**, 134704 (2023).

[24] D. J. Norris and M. G. Bawendi, "Measurement and assignment of the size-dependent optical spectrum in CdSe quantum dots", Phys. Rev. B **53**, 16338 (1996).

[25] K. Gong, Y. Zeng, and D. F. Kelley, "Extinction Coefficients, Oscillator Strengths, and Radiative Lifetimes of CdSe, CdTe, and CdTe/CdSe Nanocrystals", J. Phys. Chem. C **117**, 20268 (2013).

[26] R. Rossetti, S. Nakahara, and L. E. Brus, "Quantum size effects in the redox potentials, resonance Raman spectra, and electronic spectra of CdS crystallites in aqueous solution", J. Chem. Phys. **79**, 1086 (1983).

[27] C. B. Murray, D. J. Norris, and M. G. Bawendi, "Synthesis and characterization of nearly monodisperse CdE (E = sulfur, selenium, tellurium) semiconductor nanocrystallites", J. Am. Chem. Soc. **115**, 8706 (1993).

[28] M. G. Bawendi, A. R. Kortan, M. L. Steigerwald, and L. E. Brus, "X-ray structural characterization of larger CdSe semiconductor clusters", J. Chem. Phys. **91**, 7282 (1989).

[29] B. O. Dabbousi, J. Rodriguez-Viejo, F. V. Mikulec, J. R. Heine, H. Mattoussi, R. Ober, K. F. Jensen, and M. G. Bawendi, "(CdSe)ZnS Core−Shell Quantum Dots: Synthesis and Characterization of a Size Series of Highly Luminescent Nanocrystallites", J. Phys. Chem. B **101**, 9463 (1997).

[30] Y. Yin and A. P. Alivisatos, "Colloidal nanocrystal synthesis and the organic–inorganic interface", Nature **437**, 664 (2005).

[31] X. Peng, J. Wickham, and A. P. Alivisatos, "Kinetics of II-VI and III-V Colloidal Semiconductor Nanocrystal Growth: "Focusing" of Size Distributions", J. Am. Chem. Soc. **120**, 5343 (1998).

[32] X. Peng, M. C. Schlamp, A. V. Kadavanich, and A. P. Alivisatos, "Epitaxial Growth of Highly Luminescent CdSe/CdS Core/Shell Nanocrystals with Photostability and Electronic Accessibility", J. Am. Chem. Soc. **119**, 7019 (1997).

[33] M. Liu, G. Tang, Y. Liu, and F.-L. Jiang, "Ligand Exchange of Quantum Dots: A Thermodynamic Perspective", J. Phys. Chem. Lett. **15**, 1975 (2024).

[34] A. V. Rodina and A. L. Efros, "Radiative recombination from dark excitons in nanocrystals: Activation mechanisms and polarization properties", Phys. Rev. B **93**, 155427 (2016).

[35] A. V. Rodina and A. L. Efros, "Band-edge biexciton in nanocrystals of semiconductors with a degenerate valence band", Phys. Rev. B **82**, 125324 (2010).

[36] D. J. Norris and M. G. Bawendi, "Measurement and assignment of the size-dependent optical spectrum in CdSe quantum dots", Phys. Rev. B **53**, 16338 (1996).

[37] A. Kelley, *Condensed-Phase Molecular Spectroscopy and Photophysics* (Wiley, 2012).

[38] A. Bajpai and D. F. Kelley, "Ligand effects on the angular momentum fine structure of CdTe quantum dots", J. Chem. Phys. **163**, 154308 (2025).

[39] P. C. Sercel and A. L. Efros, "Band-Edge Exciton in CdSe and Other II–VI and III–V Compound Semiconductor Nanocrystals − Revisited", Nano Lett. **18**, 4061 (2018).

[40] P. C. Sercel, A. Shabaev, and A. L. Efros, "Photoluminescence Enhancement through Symmetry Breaking Induced by Defects in Nanocrystals", Nano Lett. **17**, 4820 (2017).

[41] S. J. Strickler and R. A. Berg, "Relationship between absorption intensity and fluorescence lifetime of molecules", J. Chem. Phys. **37**, 814 (1962).

[42] W. W. Yu, L. Qu, W. Guo, and X. Peng, "Experimental Determination of the Extinction Coefficient of CdTe, CdSe, and CdS Nanocrystals", Chem. Mater. **15**, 2854 (2003).

[43] J. Jasieniak, L. Smith, J. van Embden, P. Mulvaney, and M. Califano, "Re-examination of the Size-Dependent Absorption Properties of CdSe Quantum Dots", J. Phys. Chem. C **113**, 19468 (2009).

[44] J. S. Kamal, A. Omari, K. Van Hoecke, Q. Zhao, A. Vantomme, F. Vanhaecke, R. K. Capek, and Z. Hens, "Size-Dependent Optical Properties of Zinc Blende Cadmium Telluride Quantum Dots", J. Phys. Chem. C **116**, 5049 (2012).

[45] C. de Mello Donegá and R. Koole, "Size Dependence of the Spontaneous Emission Rate and Absorption Cross Section of CdSe and CdTe Quantum Dots", J. Phys. Chem. C **113**, 6511 (2009).

[46] E. D. Palik, *Handbook of optical constants of solids*, Vol. II (Academic Press, 1998).

[47] R. Luschtinetz, G. Seifert, E. Jaehne, and H.-J. P. Adler, "Infrared Spectra of Alkylphosphonic Acid Bound to Aluminium Surfaces", Macromolecular Symposia **254**, 248 (2007).

[48] J. G. Son, E. Choi, Y. Piao, S. W. Han, and T. G. Lee, "Probing organic ligands and their binding schemes on nanocrystals by mass spectrometric and FT-IR spectroscopic imaging", Nanoscale **8**, 4573 (2016).

[49] J. J. Grenland, C. J. A. Maddux, D. F. Kelley, and A. M. Kelley, "Charge trapping versus exciton delocalization in CdSe quantum dots", J. Phys. Chem. Lett. **8**, 5113 (2017).

[50] A. Bajpai and D. F. Kelley, "Effect of surface chemistry on the continuum intensity in cdte quantum dots", J. Phys. Chem. C **(in review)** (2026).

[51] P. Brosseau, D. Jasrasaria, A. Ghosh, H. Seiler, S. Palato, and P. Kambhampati, "Two-dimensional electronic spectroscopy reveals dynamics within the bright fine structure of CdSe quantum dots", J. Phys. Chem. Lett. **15**, 1702 (2024).

[52] J. S. Kamal, A. Omari, K. V. Hoecke, Q. Zhao, A. Vantomme, F. Vanhaecke, R. K. Capek, and Z. Hens, "Size-dependent optical properties of zinc blende cadmium telluride quantum dots", J. Phys. Chem. C **116**, 5049 (2012).

[53] S. Lin, J. Li, C. Pu, H. Lei, M. Zhu, H. Qin, and X. Peng, "Surface and intrinsic contributions to extinction properties of ZnSe quantum dots", Nano Res. **13**, 824 (2020).

[54] A. J. Houtepen, Z. Hens, J. S. Owen, and I. Infante, "On the origin of surface traps in colloidal II–VI semiconductor nanocrystals", Chem. Mater. **29**, 752 (2017).

[55] M. Jones, S. S. Lo, and G. D. Scholes, "Quantitative modeling of the role of surface traps in CdSe/CdS/ZnS nanocrystal photoluminescence decay dynamics", Proc. Nat. Acad. Sci. **106**, 3011 (2009).

[56] C. Giansante and I. Infante, "Surface traps in colloidal quantum dots: A combined experimental and theoretical perspective", J. Phys. Chem. Lett. **8**, 5209 (2017).

[57] E. Busby, N. C. Anderson, J. S. Owen, and M. Y. Sfeir, "Effect of surface stoichiometry on blinking and hole trapping dynamics in CdSe nanocrystals", J. Phys. Chem. C **119**, 27797 (2015).

[58] F. T. Rabouw, M. Kamp, R. J. A. van Dijk-Moes, D. R. Gamelin, A. F. Koenderink, A. Meijerink, and D. Vanmaekelbergh, "Delayed exciton emission and its relation to blinking in CdSe quantum dots", Nano Lett. **15**, 7718 (2015).

[59] J. Jasieniak and P. Mulvaney, "From Cd-rich to Se-rich – the manipulation of CdSe nanocrystal surface stoichiometry", J. Am. Chem. Soc. **129**, 2841 (2007).

[60] N. C. Anderson, M. P. Hendricks, J. J. Choi, and J. S. Owen, "Ligand exchange and the stoichiometry of metal chalcogenide nanocrystals: spectroscopic observation of facile metal-carboxylate displacement and binding", J. Am. Chem. Soc. **135**, 18536 (2013).

[61] N. C. Anderson and J. S. Owen, "Soluble, chloride-terminated CdSe nanocrystals: ligand exchange monitored by ^{1}H and ^{31}P NMR spectroscopy", Chem. Mater. **25**, 69 (2013).

[62] Y. Xia, W. Chen, P. Zhang, S. Liu, K. Wang, X. Yang, H. Tang, L. Lian, J. He, X. Liu, G. Liang, M. Tan, L. Gao, H. Liu, H. Song, D. Zhang, J. Gao, K. Wang, X. Lan, X. Zhang, P. Müller-Buschbaum, J. Tang, and J. Zhang, "Facet control for trap-state suppression in colloidal quantum dot solids", Adv. Funct. Mater. **30**, 2000594 (2020).

[63] C. Giansante, I. Infante, E. Fabiano, R. Grisorio, G. P. Suranna, and G. Gigli, ""Darker-than-Black" PbS quantum dots: enhancing optical absorption of colloidal semiconductor nanocrystals via short conjugated ligands", J. Am. Chem. Soc. **137**, 1875 (2015).

[64] A. Bajpai and D. F. Kelley, "Ligand effects on the angular momentum fine structure of CdTe quantum dots", J. Chem. Phys. **163** (2025).

[65] Y. Zeng and D. F. Kelley, "Surface charging in CdSe quantum dots: infrared and transient absorption spectroscopy", J. Phys. Chem. C **121**, 16657 (2017).

[66] D. Morgan and D. F. Kelley, "Spectroscopy of surface-state *p*-doped CdSe/CdS quantum dots", J. Phys. Chem. Lett. **9**, 4160 (2018).

[67] X. Cai, J. E. Martin, L. E. Shea-Rohwer, K. Gong, and D. F. Kelley, "Thermal quenching mechanisms in II-VI semiconductor nanocrystals", J. Phys. Chem. C **117**, 7902 (2013).

[68] H. Lee, B. G. Jeong, W. K. Bae, D. C. Lee, and J. Lim, "Surface state-induced barrierless carrier injection in quantum dot electroluminescent devices", Nature Commun. **12**, 5669 (2021).

[69] A. Ali, F. Rehman, T. Das, I. Hussain, K. Lee, W. Jiang, S. Oh, J. Park, I. Goddard W. A., S. J. Oh, and H. Chae, "Optimizing QLED performance and stability via the surface modification of PEDOT:PSS experimental insights and DFT calculations", ACS Appl. Mater. Interfaces **16**, 57437 (2024).

[70] T. Shen, B. Li, K. Zheng, T. Pullerits, G. Cao, and J. Tian, "Surface engineering of quantum dots for remarkably high detectivity photodetectors", J. Phys. Chem. Lett. **9**, 3285 (2018).

[71] X. Cai, H. Mirafzal, K. Nguyen, V. Leppert, and D. F. Kelley, "Spectroscopy of CdTe/CdSe Type-II Nanostructures: Morphology, Lattice Mismatch, and Band-Bowing Effects", J. Phys. Chem. C **116**, 8118 (2012).

[72] D. Aldakov and P. Reiss, "Safer-by-Design Fluorescent Nanocrystals: Metal Halide Perovskites vs Semiconductor Quantum Dots", J. Phys. Chem. C **123**, 12527 (2019).

[73] O. Zakharov, A. Rubio, X. Blase, M. L. Cohen, and S. G. Louie, "Quasiparticle band structures of six II-VI compounds: ZnS, ZnSe, ZnTe, CdS, CdSe, and CdTe", Phys. Rev. B **50**, 10780 (1994).

[74] H. Liu, J. S. Owen, and A. P. Alivisatos, "Mechanistic study of precursor evolution in colloidal Group II-VI semiconductor nanocrystal synthesis", J. Am. Chem. Soc. **129**, 305 (2007).

[75] O. Chen, X. Chen, Y. Yang, J. Lynch, H. Wu, J. Zhuang, and Y. C. Cao, "Synthesis of metal-selenide nanocrystals using selenium dioxide as the selenium precursor", Angew. Chem. Int. Ed. **47**, 8638 (2008).

[76] X. Li, D. Liu, and D. Wang, "Anharmonic phonon decay in polycrystalline CdTe thin film", Appl. Phys. Lett. **112** (2018).

[77] L. von Szentpály, "Atom-Based Thermochemistry: Predictions of the Sublimation Enthalpies of Group 12 Chalcogenides and the Formation Enthalpies of their Polonides", J. Phys. Chem. A **112**, 12695 (2008).

[78] J. Berkowitz and W. A. Chupka, "Photoionization of High-Temperature Vapors. VI. S2, Se2, and Te2", J. Chem. Phys. **50**, 4245 (1969).

[79] J. J. Grenland, C. J. A. Maddux, D. F. Kelley, and A. M. Kelley, "Charge trapping versus exciton delocalization in CdSe quantum dots", J. Phys. Chem. Lett. **8**, 5113 (2017).

[80] J. van Embden, J. Jasieniak, D. E. Gomez, P. Mulvaney, and M. Giersig, "Review of the synthetic chemistry in the production of Core/Shell semiconductor nanocrystals", Aust. J. Chem. **60**, 457 (2007).

[81] A. Bajpai, C. Sunderland, X. Wang, D. Olmeijer, I. Jen-La Plante, C. Wang, A. M. Kelley, and D. F. Kelley, "Radiative dynamics of AgIn(1−x)GaxS2 quantum dots", J. Chem. Phys. **164**, 154701 (2026).

[82] T. Uematsu, M. Tepakidareekul, T. Hirano, T. Torimoto, and S. Kuwabata, "Facile high-yield synthesis of Ag–In–Ga–S quaternary quantum dots and coating with gallium sulfide shells for narrow band-edge emission", Chem. Mater. **35**, 1094 (2023).

[83] T. Uematsu, K. Wajima, D. K. Sharma, S. Hirata, T. Yamamoto, T. Kameyama, M. Vacha, T. Torimoto, and S. Kuwabata, "Narrow band-edge photoluminescence from $AgInS_2$ semiconductor nanoparticles by the formation of amorphous III–VI semiconductor shells", NPG Asia Mater. **10**, 713 (2018).

[84] T. Uematsu, R. Izumi, S. Sugano, R. Sugano, T. Hirano, G. Motomura, T. Torimoto, and S. Kuwabata, "Spectrally narrow band-edge photoluminescence from $AgInS_2$-based core/shell quantum dots for electroluminescence applications", Faraday Disc. **250**, 281 (2024).

[85] W. Hoisang, T. Uematsu, T. Yamamoto, T. Torimoto, and S. Kuwabata, "Core nanoparticle engineering for narrower and more intense band-edge emission from $AgInS_2/GaS_x$ core/shell quantum dots", Nanomaterials **9**, 1763 (2019).

[86] W. Hoisang, T. Uematsu, T. Torimoto, and S. Kuwabata, "Luminescent quaternary $Ag(In_xGa_{1-x})S_2/GaS_y$ core/shell quantum dots prepared using dithiocarbamate compounds and photoluminescence recovery via post treatment", Inorg. Chem. **60**, 13101 (2021).

[87] T. Kameyama, M. Kishi, C. Miyamae, D. K. Sharma, S. Hirata, T. Yamamoto, T. Uematsu, M. Vacha, S. Kuwabata, and T. Torimoto, "Wavelength-tunable band-edge photoluminescence of nonstoichiometric Ag–In–S nanoparticles via Ga^{3+} doping", ACS Appl. Mater. Interfaces **10**, 42844 (2018).

[88] D. F. Kelley, "Angular momentum fine structure in InP/ZnSe quantum dots", J. Phys. Chem. Lett. **15**, 6279 (2024).

[89] P. Cavanaugh, H. Sun, I. J.-L. Plante, M. J. Bautista, C. Ippen, R. Ma, A. M. Kelley, and D. F. Kelley, "Radiative dynamics and delayed emission in pure and doped InP/ZnSe/ZnS quantum dots", J. Chem. Phys. **155**, 224705 (2021).

[90] A. L. Efros, M. Rosen, M. Kuno, M. Nirmal, D. J. Norris, and M. Bawendi, "Band-edge exciton in quantum dots of semiconductors with a degenerate valence band: dark and bright exciton states", Phys. Rev. B **54**, 4843 (1996).

[91] P. C. Sercel and A. L. Efros, "Band-edge exciton in CdSe and other II–VI and III–V compound semiconductor nanocrystals — revisited", Nano Lett. **18**, 4061 (2018).

[92] J. R. Lakowicz, *Principles of fluorescence spectroscopy*, 3rd (Springer, New York, 2006).

[93] S. J. Strickler and R. A. Berg, "Relationship between absorption intensity and fluorescence lifetime of molecules", J. Chem. Phys. **37**, 814 (1962).

[94] T. Slater, Y. Chen, G. Auton, N. Zaluzec, and S. Haigh, "X-ray absorption correction for quantitative scanning transmission electron microscopic energy-dispersive x-ray spectroscopy of spherical nanoparticles", Microsc. Microanal. **22**, 440 (2016).

[95] B. Boruah, J. M. Modak, and G. Madras, "Construction of a Z-scheme Ag_2S-In_2S_3 structure: towards enhanced photocatalytic inactivation of bacteria and degradation of 4-nitrophenol", Top. Catalysis **68**, 194 (2025).

[96] D. Danilović, D. K. Božanić, G. A. Garcia, L. Nahon, U. Stamenović, V. V. Vodnik, and V. Djoković, "Velocity map imaging VUV angle-resolved photoelectron spectroscopy of isolated silver sulfide nanoparticles", Opt. Quantum Electron. **54**, 604 (2022).

[97] D. Huang and C. Persson, "Photocatalyst $AgInS_2$ for active overall water-splitting: A first-principles study", Chem. Phys. Lett. **591**, 189 (2014).

[98] Y. Lei, H. Jia, W. He, Y. Zhang, L. Mi, H. Hou, G. Zhu, and Z. Zheng, "Hybrid solar cells with outstanding short-circuit currents based on a room temperature soft-chemical strategy: the case of P3HT:Ag_2S", J. Am. Chem. Soc. **134**, 17392 (2012).

[99] J. Liu, S. Chen, Q. Liu, Y. Zhu, and Y. Lu, "Density functional theory study on electronic and photocatalytic properties of orthorhombic $AgInS_2$", Comput. Mater. Sci. **91**, 159 (2014).

[100] J. Liu and E. Hua, "Electronic structure and absolute band edge position of tetragonal $AgInS_2$ photocatalyst: A hybrid density functional study", Mater. Sci. Semicond. Process. **40**, 446 (2015).

[101] Y.-L. Liu, C.-L. Yang, M.-S. Wang, X.-G. Ma, and Y.-G. Yi, "Ternary chalcogenides $XGaS_2$ (X = ag or cu) for photocatalytic hydrogen generation from water splitting under irradiation of visible light", Int. J. Quantum Chem. **120**, 26166 (2019).

[102] Q. Wu, L. Tan, X. Liu, Z. Li, Y. Zhang, Y. Zheng, Y. Liang, Z. Cui, S. Zhu, and S. Wu, "The enhanced near-infrared photocatalytic and photothermal effects of MXene-based heterojunction for rapid bacteria-killing", Appl. Catal. B **297**, 120500 (2021).

[103] T. Omata, K. Nose, and S. Otsuka-Yao-Matsuo, "Size dependent optical band gap of ternary I-III-VI_2 semiconductor nanocrystals", J. Appl. Phys. **105**, 073106 (2009).

[104] S.-H. Wei, S. B. Zhang, and A. Zunger, "First-principles calculation of band offsets, optical bowings, and defects in CdS, CdSe, CdTe, and their alloys", J. Appl. Phys. **87**, 1304 (2000).

[105] K. Gong, D. F. Kelley, and A. M. Kelley, "Non-uniform excitonic charge distribution enhances exciton-phonon coupling in ZnSe/CdSe alloyed quantum dots", J. Phys. Chem. Lett. **8**, 626 (2017).

[106] A. Shabaev, M. J. Mehl, and A. L. Efros, "Energy band structure of $CuInS_2$ and optical spectra of $CuInS_2$ nanocrystals", Phys. Rev. B **92**, 35431 (2015).

[107] K. E. Hughes, S. R. Ostheller, H. D. Nelson, and D. R. Gamelin, "Copper's role in the photoluminescence of $Ag_{1-x}Cu_xInS_2$ nanocrystals, from copper-doped $AgInS_2$ ($x \sim 0$) to $CuInS_2$ ($x = 1$)", Nano Lett. **19**, 1318 (2019).

[108] H. S. Shim, M. Ko, S. Jeong, S. Y. Shin, S. M. Park, Y. R. Do, and J. K. Song, "Enhancement mechanism of quantum yield in alloyed-core/shell structure of ZnS–$CuInS_2$/ZnS quantum dots", J. Phys. Chem. C **125**, 9965 (2021).

[109] M. L. Zaffalon, V. Pinchetti, A. Camellini, S. Vikulov, C. Capitani, B. Bai, M. Xu, F. Meinardi, J. Zhang, L. Manna, M. Zavelani-Rossi, S. A. Crooker, and S. Brovelli, "Intrinsic and extrinsic exciton recombination pathways in $AgInS_2$ colloidal nanocrystals", Energy Mater. Adv. **2021**, 1959321 (2021).

[110] S. M. Kobosko and P. V. Kamat, "Indium-rich $AgInS_2$–ZnS quantum dots—Ag-/Zn-dependent photophysics and photovoltaics", J. Phys. Chem. C **122**, 14336 (2018).

[111] T. Uematsu, K. Wajima, D. K. Sharma, S. Hirata, T. Yamamoto, T. Kameyama, M. Vacha, T. Torimoto, and S. Kuwabata, "Narrow band-edge photoluminescence from AgInS2 semiconductor nanoparticles by the formation of amorphous III–VI semiconductor shells", NPG Asia Mater **10**, 713 (2018).

[112] T. Uematsu, M. Tepakidareekul, T. Hirano, T. Torimoto, and S. Kuwabata, "Facile High-Yield Synthesis of Ag–In–Ga–S Quaternary Quantum Dots and Coating with Gallium Sulfide Shells for Narrow Band-Edge Emission", Chem. Mater. **35**, 1094 (2023).

[113] S. Lin, J. Li, C. Pu, H. Lei, M. Zhu, H. Qin, and X. Peng, "Surface and intrinsic contributions to extinction properties of ZnSe quantum dots", Nano Res. **13**, 824 (2020).

[114] Y. Yang, J. Li, L. Lin, and X. Peng, "An efficient and surface-benign purification scheme for colloidal nanocrystals based on quantitative assessment", Nano Res. **8**, 3353 (2015).